

**MULTICHANNEL BLIND DECONVOLUTION  
IN UNDERWATER ACOUSTIC CHANNELS**

A Dissertation  
Presented to  
The Academic Faculty

By

Ning Tian

In Partial Fulfillment  
of the Requirements for the Degree  
Doctor of Philosophy in the  
School of Electrical and Computer Engineering

Georgia Institute of Technology

May 2018

Copyright © Ning Tian 2018

MULTICHANNEL BLIND DECONVOLUTION  
IN UNDERWATER ACOUSTIC CHANNELS

Approved by:

Professor Justin Romberg  
School of Electrical and Computer  
Engineering  
*Georgia Institute of Technology*

Professor James McClellan  
School of Electrical and Computer  
Engineering  
*Georgia Institute of Technology*

Professor Mark Davenport  
School of Electrical and Computer  
Engineering  
*Georgia Institute of Technology*

Professor Karim Sabra  
School of Mechanical  
Engineering  
*Georgia Institute of Technology*

Professor Christopher Rozell  
School of Electrical and Computer  
Engineering  
*Georgia Institute of Technology*

Date Approved: March 20, 2018



To my parents.

## ACKNOWLEDGEMENTS

I would like to begin by extending my deepest gratitude to my advisor, Dr. Justin Romberg, for his relentless support, valuable advice, and continuous encouragement during my journey as a Ph.D. student. The completion of my dissertation would not have been possible without his inspiration, guidance, and help. I thank him for his profound belief in my work. I am also extremely grateful to Dr. Karim Sabra for his efforts in introducing me to exciting research problems in acoustic imaging and providing me invaluable opportunities for collaborating with his group. I am deeply indebted to him for his valuable insight and unwavering support.

I would also like to express my sincere thanks to Drs. Mark Davenport, James McClellan, and Christopher Rozell for providing me with many thoughtful suggestions on my thesis. I must thank them for reviewing my thesis and always making their time available.

Thanks should also go to our collaborators in the Scripps Institution of Oceanography: Dr. William Kuperman, Dr. Bill Hodgkiss and Chris Verlinden. I also wish to thank Dr. Sung Hoon Byun and Nick Durofchalk for their collaboration. The experimental data used in this thesis are credited to their great amount of assistance. I would like to convey my special thanks to Dr. Kiryung Lee for collaborating with me on many fronts of the research presented in this thesis. His extensive knowledge, constructive advice, helpful contributions, and great friendship have earned my highest regard. I had great pleasure working with them all.

I also would like to joyously acknowledge my fellow students, scholars, and alumni: Ali, Sohail, Alireza, William, Chris, Aurele, Salman, Liangbei, Tomer, Rakshith, Kyle, Kevin, Darryl, and Steve. I have enjoyed all of our interactions that have accompanied our exploration of new ideas in all areas. I cannot leave Georgia Tech without mentioning many of my good friends from the Tsinghua Alumni Association

of Georgia, who are always inspiring and interesting and help me maintain my positive morale.

My heartfelt regards go to Bill and Valerie for their unconditioned love and moral support. I must thank Bill Needle for showing me the commitments and responsibilities he has carried forward since he graduated from Tech more than a half century ago. Thanks should also go to Jane Chisholm for teaching me scientific writing and tirelessly editing my writings. Special thanks to Josyane Roschitz, without whom my early phase of graduate study at Georgia Tech-Lorraine would not have been completed.

Finally, I am forever indebted to my family. I thank my mother and father for their love, support, and encouragement, which have sustained me along this entire journey. Their patience and sacrifice will remain my inspiration throughout my life. I cannot begin to express my gratitude to Joe and Lisa, who embraced me in the Bankoff family, enriched a great part of my vision, and provided me with meaningful guidance on what really matters in a useful life. Their boundless love and unparalleled support have been and will always be my strength.

## TABLE OF CONTENTS

<b>ACKNOWLEDGEMENTS</b> . . . . .	iv
<b>LIST OF FIGURES</b> . . . . .	x
<b>SUMMARY</b> . . . . .	xv
<b>Chapter 1: INTRODUCTION</b> . . . . .	1
1.1 Notations . . . . .	4
1.2 The Multichannel Blind Deconvolution Problem . . . . .	4
1.3 Deconvolution via Low-rank Recovery . . . . .	6
1.4 Deconvolution Using a Bilinear Channel Model . . . . .	9
1.5 Subspace Learning for Multichannel Deconvolution . . . . .	13
1.6 Contributions and Organization of the Thesis . . . . .	16
<b>Chapter 2: MULTICHANNEL DECONVOLUTION VIA LOW-RANK             RECOVERY</b> . . . . .	19
2.1 Introduction . . . . .	19
2.2 Multichannel Deconvolution . . . . .	22
2.2.1 The sensing scenario . . . . .	22
2.2.2 Finite impulse response (FIR) channels . . . . .	23
2.2.3 The heuristic solver . . . . .	27

2.2.4	A general linear model for the CIR . . . . .	29
2.3	Linear Models for Multipath CIR in Ocean Waveguides . . . . .	31
2.3.1	The multipath CIR with known arrival-times and unknown amplitudes . . . . .	31
2.3.2	The multipath CIR with uncertain arrival-times and unknown amplitudes . . . . .	32
2.4	Numerical Results . . . . .	35
2.4.1	Stylized simulations . . . . .	35
2.4.2	Robustness analysis . . . . .	38
2.4.3	Numerical simulations in an ocean waveguide . . . . .	40
2.4.4	Deconvolution of experimentally measured shipping noise recordings . . . . .	43
2.5	An Extension to Blind Source Separation . . . . .	47
2.6	Conclusion . . . . .	52
 <b>Chapter 3: MULTICHANNEL DECONVOLUTION USING BILINEAR CHANNEL MODELS . . . . .</b>		 54
3.1	Introduction . . . . .	54
3.2	Bilinear Channel Models . . . . .	57
3.3	Spectral Methods for Multichannel Deconvolution . . . . .	65
3.4	Non-convex Optimization Algorithms . . . . .	69
3.4.1	An alternating eigenvectors method . . . . .	70
3.4.2	A truncated power method . . . . .	71
3.4.3	Spectral initialization. . . . .	73
3.5	Main Results . . . . .	75

3.6	Numerical Simulation Results . . . . .	80
3.6.1	NC09 noise data simulations . . . . .	80
3.6.2	Santa Barbara Channel experimental data simulations . . . . .	83
3.6.3	Robustness performance in underwater acoustic channels . . . . .	87
3.6.4	Robustness performance using generic subspaces . . . . .	90
3.7	Conclusion . . . . .	95
 <b>Chapter 4: SUBSPACE LEARNING FOR MULTICHANNEL DE-CONVOLUTION . . . . .</b>		<b>96</b>
4.1	Introduction . . . . .	96
4.2	Subspace Learning Problem Formulation . . . . .	98
4.2.1	Optimization over a Grassmannian manifold . . . . .	100
4.2.2	Subspace learning via low-rank recovery . . . . .	102
4.3	Optimization Algorithms . . . . .	103
4.3.1	Optimization over a Grassmannian manifold . . . . .	103
4.3.2	Subspace learning via low-rank recovery . . . . .	105
4.4	Numeric Results . . . . .	107
4.4.1	Generic channels . . . . .	107
4.4.2	Acoustic channels . . . . .	110
4.5	Conclusion and Future Work . . . . .	112
 <b>Chapter 5: CONCLUSIONS . . . . .</b>		<b>114</b>
 <b>Appendix A: Proof of the Main Results . . . . .</b>		<b>117</b>
A.1	Proof of Proposition A.0.1 . . . . .	118

<b>Appendix B: Analysis of Spectral Initialization . . . . .</b>	<b>123</b>
<b>Appendix C: Convergence of Non-convex Optimization Algorithms .</b>	<b>130</b>
C.1 Convergence of the Alternating Eigenvectors Method . . . . .	130
C.1.1 Tail estimates of deviations . . . . .	130
C.1.2 Proof of Proposition A.1.2 . . . . .	134
C.1.3 Proof of Proposition A.1.3 . . . . .	137
C.2 Convergence of the Rank-1 Truncated Power Iteration Method . . . .	139
C.2.1 Proof of Theorem C.2.1 . . . . .	142
C.3 Proof of Lemma 3.4.1 . . . . .	151
<b>References . . . . .</b>	<b>160</b>

## LIST OF FIGURES

1.1	Multichannel deconvolution problem. From measurements of $M$ channel outputs, we want to estimate both the source $s(t)$ and channel responses $h_m(t)$ ( $m = 1, \dots, M$ ). . . . .	5
1.2	A typical example of multipath CIRs in underwater acoustic channels. Each CIR consists of several pulses at different arrival-times. . . . .	5
1.3	Illustration of construction of a joint linear subspace model from a parametric model. (a) A uniform array of $M$ sensors. (b) Examples of $\{\mathbf{g}_r\}$ rearranged as $M$ -by- $K$ matrices. (c) Sorted eigenvalues of $\mathbf{H}_{\mathcal{R}}$ in a logarithmic scale. (d) First few dominant eigenvectors of $\mathbf{H}_{\mathcal{R}}$ rearranged as $M$ -by- $K$ matrices. . . . .	11
2.1	To illustrate the proposed approach, the matrix $\mathbf{X}_0$ defined in Eq. (2.4) is explicitly written with a number of measurements per channel of $L = 9$ , channel length $K = 3$ , and a number of channels $M = 3$ . Each observation $y_m[\ell]$ is a sum along one of the skew diagonals of the a submatrix of $\mathbf{X}_0$ , as illustrated by the red lines above. Recovering an $L + K - 1 \times KM$ matrix from measurements of this type is virtually impossible, but explicitly incorporating the fact that $\mathbf{X}_0$ has rank-1 structure into the recovery makes the recovery possible for appropriate values of $L, K, M$ . . . . .	26
2.2	(a) An illustration of the small time shifts of a band-limited basis pulse (400 – 600 Hz). All shifted pulses form an over-complete subspace matrix $\mathbf{B}_{10}$ for any ray-like pulse that arrives within an uncertainty window of duration $\Delta t = 3$ ms. (b) The singular value spectrum of the corresponding over-complete matrix $\mathbf{B}_{10}$ . The plot contains the first 20 of 600 singular values. The first $R = 6$ singular values capture more than 99% of the total energy. (c) The pulse subspace matrix $\mathbf{B}_1$ , consisting of the $R = 6$ principal components of $\mathbf{B}_{10}$ . . . . .	34



2.3	Examples of recovery for finite-duration CIRs ( $K = 200$ taps) using $M = 100$ channels. (a) Comparison of the original source signal (solid line) and the recovered source signal (dashed line). The relative error is $3 \times 10^{-5}$ (only the first 300 samples out of 1000 samples are plotted). (b) Comparison of the true underlying CIRs (plotting only first 50 taps out of $K = 200$ for the first 3 channels) and the recovered CIRs. The average relative error across all 100 channels is $10^{-4}$ . . . . .	36
2.4	(a) Comparison of the actual CIR and recovered CIR for 5 channels assuming known arrival-times and unknown amplitudes for the 3 pulse-like arrivals of each CIR. The average relative error across all $M = 50$ channels is $2 \times 10^{-10}$ . (b) Same as (a) but assuming uncertain arrival-times ( $\Delta t = 1.5$ ms) and unknown amplitudes. The average relative error across all $M = 50$ channels is $3 \times 10^{-5}$ . . . . .	37
2.5	Variations of the recovery error (in logarithmic scale) for the deconvolution method (averaged over 100 independent realizations) vs. SNR of the recorded measurements. . . . .	39
2.6	(a) Example of channel model error caused by lack of accurate a priori information on the arrival-time structure of the actual CIR (upper plot) containing 5 arrivals. Lower plot shows the approximated CIR assuming only 3 arrivals are present. (b) Variations of the recovery error (in logarithmic scale) for the deconvolution method (averaged over 100 independent realizations) vs. channel model error. . . . .	40
2.7	(a) Computational shallow water waveguide. (b) Experimentally-measured sound speed profile. (c) A priori information of the ray arrival-time structure of the CIRs for $M = 16$ channels. For each ray arrival, the width of the black shaded area indicates the duration of the corresponding uncertainty time-window $2\Delta t$ for the shallow source shown in (a). (d) Comparison of the actual CIRs (blue solid line) obtained from normal-mode simulations and the recovered CIRs (red dashed line) across all $M = 16$ channels using the deconvolution method for the shallow source shown in (a). The average relative error across all $M = 16$ channels is $\approx 10^{-1}$ . . . . .	41
2.8	Using only the simulated-received waveforms on (a) $M = 8$ channels or (b) $M = 4$ channels for the blind deconvolution method. The relative error across all channels for both cases is $\approx 10^{-1}$ . . . . .	43

2.9	Experimental results using shipping noise. (a) Estimated CIRs using the library data set from the RBD method when the R/V was $\approx 600$ m from the VLA. (b) Same as (a) but using a different data set (the “event” set) when the R/V was within the same location on a different day. (c) Comparison of the estimated CIRs from either the RBD (red line) or the blind deconvolution method (green line) using the same event data set. (d) Comparison of the estimated CIRs with RBD using either the event data set (red line, same as shown in (b)) or the library data set. (blue line, same as shown in (a)) . . . . .	46
2.10	(a) and (b): Same as Fig. 2.9 (c) and (d) but using only $M = 8$ channels for the blind deconvolution method. (c) and (d): Same as Fig. 2.9 (c) and (d) but using only $M = 4$ channels for the blind deconvolution method. . .	47
2.11	Multiple inputs multiple outputs (MIMO) system of equations. . . . .	49
2.12	Multiple Inputs Multiple Outputs blind source separation problem scenario in underwater acoustic channels. Four ships signal are measured by the receivers on a VLA. . . . .	50
2.13	CIRs for four ships. From the measurements of $M = 30$ channel outputs, we want to estimate the four source signal up to ordering ambiguities. . .	51
2.14	Four input source signals and the separation results from convolutive measurements. The separation results are accurate other than the ordering ambiguity. . . . .	52
3.1	(a) A known pulse profile $p(t)$ . (b) Amplitudes for each CIRs. (c) Arrival-times for pulses across channels. (d) Pulses across channels for a single path case. . . . .	58
3.2	Arrival-times range across channels. Black shaded region indicates all possible arrival-times. . . . .	61
3.3	Illustration of the collection of CIRs and the eigenvalues of the space spanned by all CIRs. (a) Examples of $\mathbf{p}^i$ rearranged as M-by-N matrices. (b) Sorted eigenvalues of $\mathbf{H}_{\mathcal{R}}$ in a logarithmic scale. . . . .	62
3.4	First 6 basis of a linear subspace that are generated from a parametric embedding of all pulses across channels. . . . .	63
3.5	A priori information of the ray arrival-time structure of $M = 16$ channels for NC09 data CIRs. The black shaded region indicated the possible arrival-times of 2 separate rays. Arrival-times for each ray fall along a line. . . .	82

3.6	Recovery for 16 CIRs and the convergence performance for NC09 channels. (a) $M = 16$ multipath channels are recovery exactly using a bilinear channel model. The original CIRs and estimated CIRs are plotted on top of each other. (b) The residual in each power method iteration, and our method shows a stable convergence. . . . .	83
3.7	Illustration of the Santa Barbara Channel Experiment. Four 32-elements are deployed in the Santa Barbara shipping channel. In our simulation, we used data collected from VLA3 from the source of opportunity, which is the passing container ship Anna Maersk passed by the blue line track. . . . .	84
3.8	Recovery of $M = 31$ CIRs using bilinear channel model. (Discarded one channel from the VLA because of hardware problem) (a) 500 snapshots of arrival-times for CIRs when the ship is cruising away from VLA3 at range 1.71 km to 1.94 km. (b) The estimated CIRs (red) plot on top of the original CIRs, and the recovery SNR is 25dB. . . . .	85
3.9	Recovery of $M = 31$ CIRs using bilinear channel model. (Discarded one channel from the VLA because of hardware problem) (a) Line approximations of arrival-times for CIRs when the ship is $\approx 1.8$ km away from VLA3, the line approximations are a rough estimation of the 500 snapshots shown in Fig. 3.8a. (b) The estimated CIRs (red) plot on top of the original CIRs, and the recovery SNR is $\approx 12$ dB. . . . .	86
3.10	The algorithm robustness performance when arrival-times are not exactly on a line while the bilinear model is formed with the assumption that all arrival-times fall along a line. The red dots indicate the approximation error when using such channel model, and the blue dots are the estimation error using such channel model to perform blind deconvolution. The model error are measured by a off-line coefficient which indicates the ratio between the off-line time and the arrival-time differences among channels. . . . .	88
3.11	(a) Compared to Fig. 3.9a, a subspace with a larger dimension is used in this simulation, which is generated from a wider range of lines. (b)The red dots indicate the approximation error when using such channel model, and the blue dots are the estimation error using such channel model to perform blind deconvolution. The model error are measured by a off-line coefficient which indicates the ratio between the off-line time and the arrival-time differences among channels. . . . .	89
3.12	Monte Carlo simulation for recovery performance with noisy measurements.	90

3.13	Comparison of cross-convolution (CC), subspace-constrained cross-convolution (SCCC), alternating eigenvectors method (AltEig), and rank-1 truncated power method (RTPM). Default parameter setting: $M = 8$ , $K = 256$ , $D = 32$ , $L = 20K$ , $\text{SNR} = 20$ dB. The 95th percentile estimation error is plotted in a logarithmic scale as we vary each parameter as follows: (a) $L$ , (b) $D$ , (c) $M$ , (d) $\text{SNR}$ . . . . .	92
3.14	Convergence of alternating eigenvectors method (AltEig) and rank-1 truncated power method (RTPM) for a random instance. $x$ -axis: iteration index, $y$ -axis: log of the estimation error. $M = 8$ , $K = 256$ , $D = 32$ , $L = 20K$ , $\text{SNR} = 20$ dB. . . . .	93
3.15	Empirical phase transition in the 95th percentile of the log of the estimation error. $x$ -axis: $D/K$ . $y$ -axis: $L/K$ . $K = 256$ , $M = 8$ , $\text{SNR} = 20$ dB. (a) cross-convolution method [1]. (2) subspace-constrained cross-convolution method [83]. (c) alternating eigenvectors method ( $\hat{\sigma}_w^2 = \sigma_w^2$ ). (d) rank-1 truncated power method ( $\hat{\sigma}_w^2 = \sigma_w^2$ ). . . . .	94
4.1	(a) Estimated CIRs from the cross-convolution method by solving each snapshot separately. Blue stems are elements of the original CIRs, and the red stems are the estimation samples. The estimation $\text{SNR} \approx 1$ dB (b) Estimated CIRs from subspace learning method. Blue stems are elements of the original CIRs, and the red stems are the estimation samples. The estimation is accurate with a $\text{SNR} = \approx 30$ dB. . . . .	108
4.2	Comparison of average CIRs estimation error between the classical cross-convolution method (red line) and the subspace learning method (blue line). (a) The number of snapshots for each method is $P = 50$ and the length of measurements $L$ from $K$ to $3K$ . $x$ -axis: the length of measurement length $L$ , $y$ -axis: log of the estimation error when the measurements $\text{SNR} = 20$ dB. (b) The length of measurements $L = 128$ and the number of snapshots for each method $P$ varies from 10 to 50. $x$ -axis: the number of snapshots $L$ , $y$ -axis: log of the estimation error when the measurements $\text{SNR} = 20$ dB. . . . .	109
4.3	Phase transition in estimation error for the subspace learning method from Monte Carlo simulation. $x$ -axis: $P$ : the length of measurement, $y$ -axis: $P$ : number of snapshots. . . . .	110
4.4	(a) The estimations of CIRs (red) using the multichannel blind method from single snapshot with an inaccurate subspace model. The estimation $\text{SNR} \approx 3$ dB. (b) Estimated CIRs (red) from subspace learning method. The starting point are the same inaccurate subspace estimations we used in from Fig. 4.4a. The estimation is accurate with a $\text{SNR} \approx 28$ dB. . . . .	112

## SUMMARY

In the past several decades, research across many disciplines has devoted considerable attention to the multichannel blind deconvolution problem. The multichannel sensing framework is ubiquitous and arises in many applications such as digital communication, medical imaging, ocean tomography and acoustic imaging. Blind deconvolution methods usually rely on the exploitation of either channel structures, input source properties, or both. Meanwhile, using sources of opportunity (e.g., radiating ships at known locations) in acoustic imaging applications has become an active research area recently. In these specific applications of multichannel blind deconvolution, using sources of opportunity means that the input source signal is unknown, so exploiting the channel structure as a priori information is critical.

This thesis develops new techniques for solving the multichannel blind deconvolution problem and implements these techniques in acoustic waveguide multiple environment. Based on the channel structures in the underwater acoustic applications, we solve the problem using two approaches. In the first approach, we formulate the problem as solving a system of bilinear equations, which in turn can be recast as recovering a low-rank matrix from a set of linear observations. In the second approach, we form a cross-correlation matrix from the channel outputs and solve the problem by minimizing a quadratic function over a non-convex set.

For the underwater acoustic channel applications, we developed a systematic way to build an efficient and accurate linear channel model incorporating a priori information about the expected Channel Impulse Responses' (CIRs) arrival-time structure. The linear model of the CIRs in underwater acoustic channels can be readily used in both approaches. Furthermore, we develop a more constrained bilinear channel model, which is motivated by the arrival-times structure across channels of a vertical line array. We solve the problem with the bilinear model assumption using the sec-

ond approach. This second approach also furthers our theoretical knowledge in the classical subspace method for blind deconvolution. We develop efficient and stable algorithms that can be applied in real world applications.

We implement both multichannel deconvolution methods on realistic acoustic channels in an ocean waveguide and experimentally validate the methods using at-sea data recorded in shallow water from short vertical line arrays. The two sets of experimental data we tested are collected from Coronado Bank (water depth  $\approx 150$  m) and Santa Barbara shipping channel (water depth  $\approx 580$  m). We also present numerical results demonstrating that the empirical performance is consistent with our theories.

We also logically extend our method to a Multiple Input Multiple Output (MIMO) system and present a blind source separation technique for convolutive measurements. In the end, we investigate methods to learn the subspace of CIRs directly from multiple snapshots in the context of solving multichannel blind deconvolution. Numerical results demonstrate the effectiveness of these methods.

## CHAPTER 1

### INTRODUCTION

The main purpose of this thesis is to develop new techniques for solving the multichannel blind deconvolution problem and to implement these techniques in an acoustic waveguide environment. In the past several decades, research across many disciplines has devoted considerable attention to the multichannel blind deconvolution problem because the multichannel sensing framework is ubiquitous.

In digital communication applications, blind methods are very attractive because they do not require the transmission of a training sequence, and they are adaptive to varying channels [1, 2, 3]. The multiple-channel framework can be implemented by either multiple sensors or oversampling the received signal. In image deconvolution [4], multichannel images are typically acquired using an imaging system with multiple sensors, multiple time instants, or multiple frequency bands. Important examples in image restoration are image denoising, image deblurring, compressed images decoding, and medical image reconstruction [5], all of which focus on recovering the image (source). In image restoration, ambiguities in channel responses usually arise from uncertainties produced by noisy convolutions with multiple unknown finite impulse response (FIR) filters, and many reports have reviewed classical image restoration methods [6, 7]. Multichannel deconvolution has also attracted interest in applications such as seismology [8] and geoacoustic imaging [9]. Last but not least, in underwater acoustic channels, many blind methods [10, 11, 12, 13] have also been studied extensively. In this thesis, our main applications of multichannel blind deconvolution methods are for underwater acoustic channels.

Acoustic remote sensing has become an essential tool for the development of mod-

ern health-care devices, the investigation of the interior of the ocean and the seafloor, the non-destructive inspection of structures, and the exploration of natural resources embedded in the Earth’s crust. We focus our discussion on underwater acoustic sensing where acoustic waves travel through an ocean waveguide. Acoustic waves carry information about their source and collect information about the environment as they propagate. In ocean tomography and environmental inversion, acoustic remote sensing typically relies on a controlled active acoustic source to probe the environment [14, 15]. In the active case, the Channel Impulse Response (CIR), which is Green’s function for a given ocean environment, can readily be obtained from recorded signals.

Although active sensing is highly reliable, the ocean already contains enough propagating acoustic energy, so using the noninvasive, low-resolution streaming sensing data to directly develop a high-resolution image of the ocean environment in a passive way is a promising alternative to active sensing. A fully passive approach can also be advantageous when regulations forbid the use of sound sources to prevent environmental disruption or when no active sources are available for the band of interests. Using sources of opportunity (e.g., radiating ships) instead of deploying and operating controlled sources emerges as a potent passive acoustic remote sensing approach [16, 17, 18]. In passive approaches, using sources of opportunity means that the broadcast source signal is unknown, and then this problem becomes a blind deconvolution problem. Estimating both the CIRs and the actual source signal using only recorded signals is generally an ill-posed problem without any additional a priori information or assumptions, especially for propagating sound through an ocean waveguide as it is distorted by multipath effects.

Blind deconvolution methods usually rely on the exploitation of either channel structures, input source properties, or both. A number of studies have introduced multichannel blind deconvolution techniques motivated by various applications. These classical techniques can be categorized into two main approaches: deterministic meth-



ods and statistical methods. Deterministic methods [3, 19, 20] typically reduce the blind deconvolution problem to a regularized least squares problem without assuming statistical properties on either the source or channels. These methods are usually critically dependent on an accurate estimate of the duration of the CIR (i.e., the channel length) to deconvolve the CIR and then to recover the source. These deterministic methods are also highly sensitivity to noise. Statistical methods, on the other hand, using second-order-statistics [21, 22] or higher-order-statistics [23] rely on statistical information about an unknown source signal, which, in practice, requires long recording duration to build up statistical information or a priori knowledge of statistic distributions. The multichannel deconvolution methods presented in this thesis are aiming to overcome the challenges in these classical methods and solve the problem from short snapshot measurements with a stable robustness performance.

The blind deconvolution problem in acoustic remote-sensing applications can be solved in various ways. One is to implement approaches that are based on both incoherent [24] and coherent noise processing. These approaches provide a foundation for passive sensing and imaging using only ambient noise sources without any active transmitter. For the coherent processing of noise recordings, some spatial coherence between sensors that receive sound from the same individual noise source, and the CIRs between two receivers can be estimated by cross-correlating long-duration ambient noise recordings from each channel [25]. Another approach, the Ray-Based Blind (RBD) deconvolution method, has been developed based on the beamforming technique using a receiver array [11]. However, a primary limitation of these acoustic imaging methods is their dependence on acoustic propagation effects and the long coherence emerging time for noise correlation techniques. Therefore, these methods sometimes cannot provide high resolution and fast recovery results. In our study of the thesis, we aim to use the estimated results obtained from the ray-based blind deconvolution technique as a priori information for building the CIR model in a varying

acoustic environment and develop a method that can quickly deconvolve and track the system within a short recording time. Furthermore, we develop a subspace learning method that can obtain the channel model directly from multiple snapshots of the convolutive measurements.

## 1.1 Notations

Unless specified otherwise, we use uppercase bold, lowercase bold, and not bold letters for matrices, vectors, and scalars, respectively. For example,  $\mathbf{X}$  denotes a matrix,  $\mathbf{x}$  represents a vector, and  $x$  refers to a scalar. We use  $X[i, j]$  to specify the  $(i, j)$ th entry of a matrix  $\mathbf{X}$ , and  $x[i]$  to signify the  $i$ th entry of a vector  $\mathbf{x}$ . Calligraphic letters such as  $\mathcal{A}$  specify linear operators. The symbol  $C$  or  $c$  refers to a constant number. The matrix  $\mathbf{X}^*$ , and the row vector  $\mathbf{x}^*$  are obtained by taking conjugate transpose of  $\mathbf{X}$ , and column vector  $\mathbf{x}$ , respectively; The matrix  $\mathbf{X}^\top$ , and the row vector  $\mathbf{x}^\top$  are obtained by taking transpose of  $\mathbf{X}$ , and column vector  $\mathbf{x}$ , respectively.  $\mathcal{A}^*$  denotes the adjoint of a linear operator  $\mathcal{A}$ . The notations  $\|\cdot\|$ ,  $\|\cdot\|_*$ , and  $\|\cdot\|_F$  denote the operator, nuclear, and Frobenius norms of the matrices, respectively. Furthermore, we will use  $\|\cdot\|_2$ , and  $\|\cdot\|_1$  to represent the vector  $\ell_2$ , and  $\ell_1$  norms.

## 1.2 The Multichannel Blind Deconvolution Problem

This thesis examines a general sensing scenario under the single-input-multiple-channel framework as depicted in Fig. 1.1a, in which the output of each channel is the convolutive measurements of a common source  $s(t)$  and CIR  $h_m(t)$ . In underwater acoustic channels, this framework can be interpreted as a network of distributed sensors (e.g., a vertical line array) listens to the same ship signal as indicated in Fig. 1.1b.

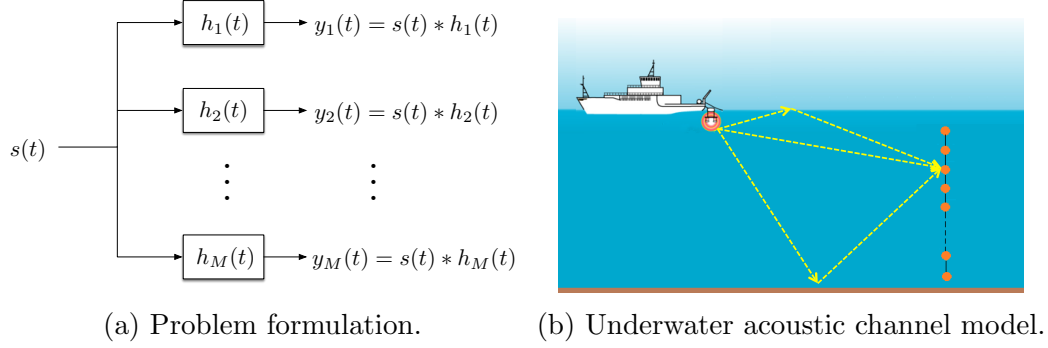


Figure 1.1: Multichannel deconvolution problem. From measurements of  $M$  channel outputs, we want to estimate both the source  $s(t)$  and channel responses  $h_m(t)$  ( $m = 1, \dots, M$ ).

As depicted in Fig. 1.1a, the common source signal  $s(t)$  drives  $M$  individual channels with the CIRs  $h_1(t), h_2(t), \dots, h_m(t)$ . Over a period of time, we observe samples of convolution outputs  $y_1(t), \dots, y_M(t)$ , where  $y_m(t) = s(t) * h_m(t)$ . From these observations alone, we wish to estimate both  $h_m(t)$  ( $m = 1, \dots, M$ ) and  $s(t)$ . A typical example of multipath CIRs in underwater acoustic waveguide is illustrated in Fig. 1.2.

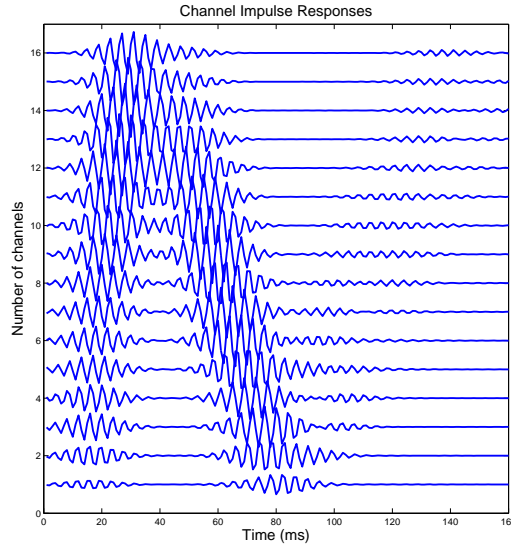


Figure 1.2: A typical example of multipath CIRs in underwater acoustic channels. Each CIR consists of several pulses at different arrival-times.

This problem does not have a unique solution if we known nothing about the source

signal  $s(t)$  or the CIR  $h_m(t)$ . However, if we make some structural assumptions about the channels, namely that they live in a subspace of some known lower dimension, then the problem, which becomes well posed, can be solved by fast and scalable algorithms. Even though many methods for solving this classical signal processing problem have been reported in various applications in the past, we are revisiting this problem by investigating both channel models and recovery methods. We show how to use a priori information about channels to build appropriate channel models that, in turn, can be incorporated into efficient algorithms.

We solve the multichannel blind deconvolution in two approaches and investigate systematic ways to form both linear and bilinear channel models. In the first approach, we formulate the problem as solving a system of bilinear equations, and in turn can be recast as recovering a low-rank matrix from a set of linear observations. In the second approach, we form a cross-correlation matrix from the channel outputs and solve the problem by minimizing a quadratic function over a non-convex set. A linear model of the CIRs in underwater acoustic channel is developed and can be readily use in both approaches. Furthermore, we develop a more confined bilinear channel model, which is motivated by the arrival-times structure across channels of a vertical line array. We solve the problem with the bilinear model assumption using the second approach. This second approach also furthers our theoretical knowledge in the classical subspace method for blind deconvolution. We develop efficient and stable algorithms that can be applied in real world applications. Moreover, we develop a novel framework for blind source separation, which is based on our low-rank recovery method in a multiple-input-multiple-output convolutive measurements scenario.

### 1.3 Deconvolution via Low-rank Recovery

Under the general framework in Fig. 1.1a), we formulate the multichannel deconvolution problem as a bilinear system of equations that can be recast as a system

of linear equations whose solution has a rank-1 structural constraint. Similar formulations via the low-rank recovery of the blind deconvolution problem for a single channel have recently been presented [26, 27]. The multichannel blind deconvolution method, which lifts the source signal and the concatenation of CIRs to their outer product, reconstructs a rank-1 matrix from a set of linear measurements.

Let's denote the common source as a vector  $\mathbf{s} \in \mathbb{R}^L$  and the  $m$ th CIR as a vector  $\mathbf{h}_m \in \mathbb{R}^K$ . Then we can arrange a large  $L \times MK$  matrix  $\mathbf{X}$  as:

$$\mathbf{X}_0 = \begin{bmatrix} \mathbf{s} \end{bmatrix} \begin{bmatrix} \mathbf{h}_1^\top & \mathbf{h}_2^\top & \cdots & \mathbf{h}_M^\top \end{bmatrix} = \begin{bmatrix} \mathbf{s}\mathbf{h}_1^\top & \mathbf{s}\mathbf{h}_2^\top & \cdots & \mathbf{s}\mathbf{h}_M^\top \end{bmatrix}.$$

Each sample of the observation  $y_m[\ell]$  as shown in Fig. 1.1a, is now a linear combination of entries in  $\mathbf{X}_0$ . Concatenating the observations from each channel into a single vector  $\mathbf{y} \in \mathbb{R}^{ML}$ , we form a linear system of equations

$$\mathbf{y} = \mathcal{A}(\mathbf{X}_0),$$

where the linear operator  $\mathcal{A}$  takes sums over skew diagonals of submatrices  $\mathbf{s}\mathbf{h}_m^\top$ .

We can now treat the recovery of the CIR  $\mathbf{h}_m$  and the source  $\mathbf{s}$  as a matrix recovery problem. By construction, the underlying matrix  $\mathbf{X}_0$  can be written as the outer product of two vectors, it has a rank-1 structure. To recover  $\mathbf{X}_0$  from  $\mathbf{y}$ , we might search for a feasible solution  $\tilde{\mathbf{X}}$  that is a  $L \times MK$  matrix that satisfies

$$\min_{\mathbf{X}} \text{rank}(\mathbf{X}) \quad \text{subject to} \quad \mathcal{A}(\mathbf{X}) = \mathbf{y}.$$

This optimization problem can then be solved using low-rank matrix recovery tools developed in recent years, such as nuclear norm minimization, low-rank approximation, iterative hard thresholding and alternating methods [28]. Results of prior

studies in the area of low-rank matrix recovery have identified effective convex relaxations [29, 30] for problems of this type and efficient, scalable heuristic solvers that enable these techniques to work with thousands of unknown variables. We implement our solver, based on the low-rank factorization method that is efficient in memory, while its formulation becomes non-convex [31, 32]. This Burer-Monteiro heuristic has assurances that the local minima of the non-convex problem are also global minima if the rank of the true solution is small [33].

The benefits of the low-rank recovery method is that a priori information about the CIRs can be directly incorporated by adding constraints and requires only short recording duration (e.g., a single snapshot). The single-channel blind deconvolution technique [26] requires certain low-dimensional subspace structures on the source signal and channels in order to reach a well-posed condition. However, the multichannel deconvolution method exploits the spatial diversity of CIRs across channels to solve the blind deconvolution problem without assuming any structure of the source signal.

A logical extension of the multichannel blind deconvolution method via low-rank recovery is to apply the same problem formulation in multiple-input-multiple-output (MIMO) deconvolution problem. In the single source system, we solved the problem by recovering a rank-1 matrix and estimated both the source CIRs simultaneously. In the MIMO system, the measurements can be written as:

$$\mathbf{y} = \mathcal{A}(\mathbf{X}_1) + \mathcal{A}(\mathbf{X}_2) + \cdots + \mathcal{A}(\mathbf{X}_R) = \mathcal{A}(\mathbf{X}).$$

where  $\mathcal{A}$  is the same linear operation as the single source case, which takes sums over skew diagonals of submatrices of  $\mathbf{X}_r$ . Here the rank of each matrix  $\mathbf{X}_r$  is 1 and the rank of their sum  $\mathbf{X} = \mathbf{X}_1 + \cdots + \mathbf{X}_R$  is at most  $R$ . Therefore, our deconvolution method via the low-rank matrix recovery formulation still holds and we are searching

for a feasible solution  $\mathbf{X}$  has the rank no greater than  $R$ .

$$\min_{\mathbf{X}} \text{rank}(\mathbf{X}) \quad \text{subject to} \quad \mathcal{A}(\mathbf{X}) = \mathbf{y}.$$

The deconvolution of the MIMO system turns convolutive mixing of multiple sources into a linear mixing of multiple sources. When we want to perform a blind source separation of these convolutive mixing of multiple sources, we can then directly implement a linear source separation technique such as Independent Component Analysis to separate the multiple sources. The novelty of this method is that we separate convolutive mixtures of multiple sources through two independent steps.

#### 1.4 Deconvolution Using a Bilinear Channel Model

In an ocean acoustic array sensing scenario, receivers of the vertical line array with equal distance (see Fig. 1.1b) spacing listen to the same source near the ocean surface in a distance. The array receives sound that propagates in separate paths (see Fig. 1.2), which have been well modeled using the image method [34]. Distances through which sound travels along the same path to each receiver, such as the direct path, are dependent on the source-receiver configuration. Meanwhile, sound traveling along the same path will experience almost the same media (speed of sound and loss) and environmental parameters. Any environmental change or disturbance of the media will result in the same fluctuation of arrival-times of sound pulses across channels. Therefore, arrival-times of the same path for each receiver are linked. We develop a bilinear channel model that is motivated by exploring this relation of arrival-times across acoustic channels.

The bilinear channel model approximates all CIR vectors jointly with two independent vectors as variables, which correspond to the structure of amplitudes and arrival-times. If all CIR vectors are concatenated as following, the bilinear channel

model can be written as

$$\begin{bmatrix} \mathbf{h}_1 \\ \mathbf{h}_2 \\ \vdots \\ \mathbf{h}_M \end{bmatrix} = \begin{bmatrix} a_1 \Phi_1 \\ a_2 \Phi_2 \\ \vdots \\ a_M \Phi_M \end{bmatrix} \mathbf{u},$$

where  $(\Phi_m)_{m=1}^M \in \mathbb{R}^{K \times D}$  are the subspace bases for the  $M$  channels,  $\mathbf{u} \in \mathbb{R}^D$  is the coefficient vector that determines the pulse arrival-times for one path across all channels, and each element of the vector  $\mathbf{a} = [a_1, \dots, a_M]^\top \in \mathbb{R}^M$  with  $a_m > 0$  is the amplitude of channel  $m$ .

Let  $\underline{\mathbf{h}} \in \mathbb{R}^{MK}$  denote the concatenation of the CIR coefficients for all channels, i.e.,

$$\underline{\mathbf{h}} = [\mathbf{h}_1^\top, \dots, \mathbf{h}_M^\top]^\top.$$

The bilinear channel model equation above can then be equivalently rewritten as a more concise form using Kronecker product as below

$$\underline{\mathbf{h}} = \Phi(\mathbf{a} \otimes \mathbf{u}),$$

where

$$\Phi := \begin{bmatrix} \Phi_1 & \mathbf{0} & \dots & \mathbf{0} \\ \mathbf{0} & \Phi_2 & \dots & \mathbf{0} \\ \vdots & \vdots & \ddots & \vdots \\ \mathbf{0} & \mathbf{0} & \dots & \Phi_M \end{bmatrix} \quad \text{and} \quad \mathbf{a} \otimes \mathbf{u} = \begin{bmatrix} a_1 \mathbf{u} \\ a_2 \mathbf{u} \\ \vdots \\ a_M \mathbf{u} \end{bmatrix}.$$

As a conceptual example of how such bilinear model might arise, we illustrate the following stylized problem for acoustic array processing. Fig. 1.3.



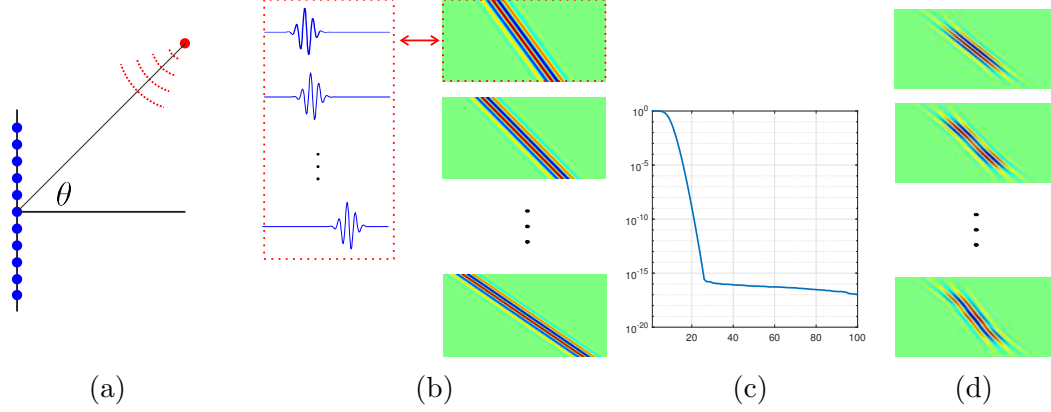


Figure 1.3: *Illustration of construction of a joint linear subspace model from a parametric model. (a) A uniform array of  $M$  sensors. (b) Examples of  $\{\mathbf{g}_{\mathbf{r}}\}$  rearranged as  $M$ -by- $K$  matrices. (c) Sorted eigenvalues of  $\mathbf{H}_{\mathcal{R}}$  in a logarithmic scale. (d) First few dominant eigenvectors of  $\mathbf{H}_{\mathcal{R}}$  rearranged as  $M$ -by- $K$  matrices.*

Figure 1.3a shows a vertical line array. Suppose we know that a source is at location  $\mathbf{r}$ , and the concatenation of the received pulses that travel from the source location to the array elements is  $\mathbf{p}_{\mathbf{r}} \in \mathbb{C}^{MK}$ . These pulse profiles are the same to one another with the same amplitude, but shifted version of each other (See Fig. 1.3b). The delays are induced by the differences in sensor locations relative to the source, while pulse profile can be determined by the filter design. Pulse profiles can also be different from element to element.

Suppose the source location varies in a small region and we denote as  $\mathbf{r} \in \mathcal{R}$ , where  $\mathcal{R}$  is some region in space. As we vary  $\mathbf{r}$  over the set  $\mathcal{R}$ , the responses  $\mathbf{p}_{\mathbf{r}}$  trace out a portion on a manifold in  $\mathbb{C}^{MK}$ . We can approximately embed this manifold onto a linear subspace of dimension  $D$  by using the  $D$  principal eigenvectors of the matrix

$$\mathbf{H}_{\mathcal{R}} = \int_{\mathbf{r} \in \mathcal{R}} \mathbf{p}_{\mathbf{r}} \mathbf{p}_{\mathbf{r}}^* d\mathbf{r}.$$

The dimension  $D$  that allows an accurate embedding depends on the size of  $\mathcal{R}$  and smoothness properties of the mapping from  $\mathbf{r}$  to  $\mathbf{p}_{\mathbf{r}}$ . In this case, we are building  $\Phi$  above by taking the  $MK \times D$  matrix that has the principal eigenvectors as columns and apportioning the first  $K$  rows to  $\Phi_1$ , the next  $K$  rows to  $\Phi_2$ , etc.

Under this more confined bilinear channel model, CIRs estimates can be found by minimizing a quadratic function over a non-convex set. We develop algorithms for multichannel blind deconvolution in this case by modifying the classical cross-convolution method. The classical method for treating the multichannel blind deconvolution problem is to recast it as an eigenvalue problem: we create a correlation matrix using the measured data  $\{\mathbf{y}_m\}$ , and estimate the CIRs from the smallest eigenvector of this matrix. These methods were pioneered in the mid-1990s [1, 3, 35]. We develop our methods based on the same basic principles, but explicitly enforce structural constraints on the solution and provide performance guarantees.

The cross-convolution method for multichannel blind deconvolution [1] follows directly from the commutivity of the convolution operator. If there is no noise in the observations, then

$$\mathbf{y}_{m_1} \circledast \mathbf{h}_{m_2} - \mathbf{y}_{m_2} \circledast \mathbf{h}_{m_1} = \mathbf{0}, \quad \text{for all } m_1, m_2 = 1, \dots, M.$$

Using  $\mathbf{T}_{\mathbf{y}_m}$  as the matrix whose action is a convolution of  $\mathbf{y}_m$  with a signal of length  $K$ , then the channel responses  $\mathbf{h}_{m_1}$  and  $\mathbf{h}_{m_2}$  must obey the linear constraints  $\mathbf{T}_{\mathbf{y}_{m_1}} \mathbf{h}_{m_2} - \mathbf{T}_{\mathbf{y}_{m_2}} \mathbf{h}_{m_1} = \mathbf{0}$ . We then collect all pairs of these linear constraints into a large system, and the vector  $\underline{\mathbf{h}} \in \mathbb{R}^{MK}$ , which corresponds to the concatenation of all CIRs vectors, is determined by

$$\mathbf{Y} \underline{\mathbf{h}} = \mathbf{0}_{M(M-1)L/2 \times 1},$$

where  $\mathbf{Y} \in \mathbb{R}^{M(M-1)L/2 \times MK}$  is defined by

$$\mathbf{Y} = \begin{bmatrix} \mathbf{Y}^{(1)} \\ \mathbf{Y}^{(2)} \\ \vdots \\ \mathbf{Y}^{(M-1)} \end{bmatrix}, \quad \mathbf{Y}^{(i)} = \begin{bmatrix} \mathbf{0}_{L,K} & \cdots & \mathbf{0}_{L,K} & \mathbf{T}_{\mathbf{y}_{i+1}} & -\mathbf{T}_{\mathbf{y}_i} \\ \vdots & & \vdots & \vdots & \ddots \\ \underbrace{\mathbf{0}_{L,K} \cdots \mathbf{0}_{L,K}}_{(i-1) \text{ blocks}} & \underbrace{\mathbf{T}_{\mathbf{y}_M} \cdots -\mathbf{T}_{\mathbf{y}_i}}_{(M-i+1) \text{ blocks}} \end{bmatrix}.$$

Then we estimate  $\underline{\mathbf{h}}$  as the minimum eigenvector of  $\mathbf{Y}^* \mathbf{Y}$

$$\hat{\underline{\mathbf{h}}} = \arg \min_{\|\mathbf{g}\|_2=1} \mathbf{g}^* \mathbf{Y}^* \mathbf{Y} \mathbf{g}.$$

Our proposed framework is to solve an optimization program above but with the additional constraint that  $\underline{\mathbf{h}}$  can be represented by a bilinear model. We then need to solve an optimization program with a Kronecker product constraint on the expansion coefficients as follow:

$$\underset{\mathbf{v}}{\text{minimize}} \quad \mathbf{v}^* \Phi^* \mathbf{Y}^* \mathbf{Y} \Phi \mathbf{v} \quad \text{subject to} \quad \|\mathbf{v}\|_2 = 1, \quad \mathbf{v} = \mathbf{a} \otimes \mathbf{u}.$$

### 1.5 Subspace Learning for Multichannel Deconvolution

Our multichannel blind deconvolution methods are based on the fact we have a priori knowledge about the CIRs, and a low-dimensional subspace where CIRs can be represented by a linear model or a bilinear model. However, we are encountered with situations that such a priori information of an accurate channel model is not readily available. Meanwhile, we are sometimes presented with multiple snapshots of convolutive measurements where both source signals and CIRs are changing for each snapshots. These measurements can be written as

$$\mathbf{y}_m(p) = \mathbf{h}_m(p) \circledast \mathbf{s}(p) + \mathbf{w}_m(p), \quad m = 1, \dots, M,$$

where  $p$  is the index for multiple snapshots  $p = 1, \dots, P$ .

The structural assumption we make here for channels is that CIRs of each snapshot  $\mathbf{h}_m(p)$  ( $m = 1, \dots, M$  and  $p = 1, \dots, P$ ) can be modeled by a fixed subspace. We assume all CIRs lie in a linear subspace with a known low-dimensional size  $D$ . Then the CIR for each channel in each snapshot can be written as

$$\mathbf{h}_m(p) = \mathbf{\Phi}_m \mathbf{u}_m(p), \quad \forall m = 1, \dots, M,$$

where  $\mathbf{\Phi}_m \in \mathbb{R}^{K \times D}$ .

In underwater acoustic channels, receivers on a Vertical Line Array (VLA) can keep measuring all sources of opportunity (e.g. ship noise) in a region. We can have multiple snapshots of measurements when a ship passes by the region, and the CIRs in each snapshot vary slightly because the ship travels a short distance against the VLA in each snapshot. As we studied in previous chapters, when the region is small, the arrival times of the pulses among all snapshots are close to each other and the CIRs are highly correlated. Therefore, a low-dimensional subspace exists for the CIRs of all snapshots.

Under this assumption of a shared subspace for CIRs in all snapshots, let's take another look at the classical cross-convolution method. In each snapshot, we can estimate the expansion coefficients  $\mathbf{u}(p) = [\mathbf{u}_1(p)^\top, \dots, \mathbf{u}_M(p)^\top]^\top$  by solving

$$\underset{\mathbf{u}(p)}{\text{minimize}} \quad \mathbf{u}(p)^* \mathbf{\Phi}^* \mathbf{Y}(p)^* \mathbf{Y}(p) \mathbf{\Phi} \mathbf{u}(p) \quad \text{subject to} \quad \|\mathbf{u}(p)\|_2 = 1.$$

where  $\mathbf{Y}(p)$  is the same large  $Y$  matrix introduced in the previous section and it is

constructed from the  $p$ th measurements  $\mathbf{y}(p)$ , and

$$\mathbf{\Phi} = \begin{bmatrix} \mathbf{\Phi}_1 & \mathbf{0} & \dots & \mathbf{0} \\ \mathbf{0} & \mathbf{\Phi}_2 & \dots & \mathbf{0} \\ \vdots & \vdots & \ddots & \vdots \\ \mathbf{0} & \mathbf{0} & \dots & \mathbf{\Phi}_M \end{bmatrix}, \quad \mathbf{\Phi}_m \in \mathbb{R}^{K \times D}.$$

The core idea of our subspace learning method is to use diverse information collected through multiple snapshots and to learn the subspace jointly. In each snapshot, the solution is to find the smallest eigenvector. Therefore, if we treat multiple snapshots jointly, the subspace which span all CIRs in  $P$  snapshots can be found as the following optimization problem.

$$\begin{aligned} & \underset{\{\mathbf{Q}_m\}_{m=1}^M}{\text{minimize}} \quad \sum_{p=1}^P \lambda_{\min}(\mathbf{Q}^\top \mathbf{Y}(p)^\top \mathbf{Y}(p) \mathbf{Q}) \\ & \text{subject to} \quad \mathbf{Q}_m^\top \mathbf{Q}_m = \mathbf{I}_D, \quad \forall m = 1, \dots, M, \end{aligned}$$

where

$$\mathbf{Q} = \begin{bmatrix} \mathbf{Q}_1 & \mathbf{0} & \dots & \mathbf{0} \\ \mathbf{0} & \mathbf{Q}_2 & \dots & \mathbf{0} \\ \vdots & \vdots & \ddots & \vdots \\ \mathbf{0} & \mathbf{0} & \dots & \mathbf{Q}_M \end{bmatrix}, \quad \mathbf{Q}_m \in \mathbb{R}^{K \times D}$$

Another interesting approach to investigate this subspace learning problem is via low-rank matrix recovery. From our linear channel model assumption  $\mathbf{h}_m(p) = \mathbf{\Phi}_m \mathbf{u}_m(p)$ , this also means that a matrix constructed by stacking all  $\mathbf{h}_m(p)$  for a fixed  $m$  as column vectors has rank- $D$  structure. Let's define a matrix  $\mathbf{H} \in \mathbb{R}^{MK \times P}$  and a

matrix  $\mathbf{H}_m \in \mathbb{R}^{K \times P}$  as below,

$$\mathbf{H} = \begin{bmatrix} \mathbf{h}_1(1) & \mathbf{h}_1(2) & \dots & \mathbf{h}_1(P) \\ \mathbf{h}_2(1) & \mathbf{h}_2(2) & \dots & \mathbf{h}_2(P) \\ \vdots & \vdots & \ddots & \vdots \\ \mathbf{h}_M(1) & \mathbf{h}_M(2) & \dots & \mathbf{h}_M(P) \end{bmatrix}, \quad \mathbf{h}(p) = \begin{bmatrix} \mathbf{h}_1(p) \\ \mathbf{h}_2(p) \\ \dots \\ \mathbf{h}_M(p) \end{bmatrix},$$

$$\text{and } \mathbf{H}_m = \begin{bmatrix} \mathbf{h}_m(1), \mathbf{h}_m(2), \dots, \mathbf{h}_m(P) \end{bmatrix}.$$

We estimate  $\mathbf{h}(p)$  for all snapshots jointly using the basic idea of cross-convolution while enforcing the low-rank structure of  $\mathbf{H}_m$ .

$$\begin{aligned} & \underset{\{\mathbf{h}(p)\}_{p=1}^P}{\text{minimize}} \quad \sum_{p=1}^P \mathbf{h}(p)^* \mathbf{Y}(p)^* \mathbf{Y}(p) \mathbf{h}(p) \\ & \text{subject to} \quad \text{rank}(\mathbf{H}_m) \leq D, \|\mathbf{H}_m\|_F = 1, \quad \forall m = 1, \dots, M, \end{aligned}$$

## 1.6 Contributions and Organization of the Thesis

This thesis develops new techniques for solving the multichannel blind deconvolution problem and implements these techniques in acoustic waveguide multiple environment. The main contributions are stated as blow:

- For underwater acoustic channel applications, a systematic way to build an efficient and accurate linear channel model incorporating a priori information about the expected CIRs' arrival-times structure is developed.
- A more constrained bilinear model that embeds a parametric model for all channels jointly into a linear space while modulates each channel's amplitude independently is developed.
- Formulates the multichannel blind deconvolution problem as solving a system

of bilinear equations, which in turn is recast as recovering a low-rank matrix from a set of linear observations.

- Using bilinear channel models, the problem is solved by minimizing a quadratic function over a non-convex set, which is formed by a cross-correlation matrix from channel outputs.
- The methods presented in the thesis are robust in the presence of additive measurement noises and model errors in the CIR parameterization.
- Performance guarantees of our methods is analyzed and demonstrated when low-dimensional subspace is generic.
- A series of numerical results demonstrate that the empirical performance is consistent with the presented theories.
- We implement both multichannel deconvolution methods on realistic acoustic channels in an ocean waveguide and experimentally validate the methods using at-sea data recorded in shallow water from short vertical line arrays at Coronado Bank and Santa Barbara shipping channel.
- A technique for blind source separation in a multiple-input-multiple-output convolutive system is presented and demonstrated.
- Subspace learning methods that can estimate the channel subspace directly from multiple snapshots of the convolutive measurements are presented.

The remainder of the thesis is organized as follows. Chapter 2 presents the multichannel blind deconvolution method via a low-rank matrix recovery formulation. We show how a priori information about the channels can be used to build a linear model systematically, which in turn makes solving these systems of equations well-posed. Chapter 2 also presents results that demonstrate our method is reliable in estimating

real underwater acoustic channels from experimental data measured at-sea. In the end of Chapter 2, an extension of our method for the MIMO deconvolution and source separation problem is presented and demonstrated numerically.

Chapter 3 presents a bilinear model for CIRs, which is motivated by the arrival-times' structure of sensor array channels. Methods of solving multichannel blind deconvolution under such bilinear channel model are introduced in this chapter. We provide main results in this chapter to show guarantee of our methods under a certain subspace assumption. Numerical results in this chapter shows the robustness of our method. A new set of at-sea experimental data from the Santa Barbara Channel is incorporated in estimating the CIRs in the simulations.

Chapter 4 investigates subspace learning methods for multichannel deconvolution problem. We presents two methods in this chapter, and both of which are demonstrated through numerical simulations. The robustness performance is demonstrated with a comparison to classical method in this chapter. Finally, Chapter 5 concludes the thesis and discuss future works.



## CHAPTER 2

### MULTICHANNEL DECONVOLUTION VIA LOW-RANK RECOVERY

#### 2.1 Introduction

Acoustic remote sensing, such as ocean tomography and geoacoustic inversion, typically relies on a controlled active source to probe the environment [14, 15]. In this case, the channel impulse response (CIR), which is the Green’s function for a given ocean environment, can readily be obtained from recorded signals since the broadcast source signal is known. A potential alternative for performing acoustic remote sensing is to use sources of opportunity (e.g., radiating ships) instead of deploying and operating controlled sources. However, using sources of opportunity means that the broadcast source signal is then unknown; thus, estimating both the CIR and the actual source signal using only recorded signals, a process commonly referred to as blind deconvolution, is generally an ill-posed problem without any additional a priori information or assumptions, especially for propagating sound through an ocean waveguide as it is distorted by multipath effects. This chapter develops a scalable methodology that solves the multichannel deconvolution problem for a source of opportunity radiating in an ocean waveguide using a priori information about CIRs between the source and the array of receiver elements.

The essence of blind deconvolution rests on the exploitation of either channel structures [36] or input source properties, or both. In the underwater acoustic community, the blind deconvolution problem has been studied by many researchers and several algorithms have been proposed [37, 38, 39, 40]. Traditional multichannel blind deconvolution methods can usually be categorized into two main approaches:

deterministic methods and statistical methods [19]. Deterministic methods, such as Kailath methods [1] and subspace methods [3], usually reduce the blind deconvolution problem to a regularized least squares problem, hence critically depend on an accurate estimate of the duration of the CIR (i.e., channel length). These methods also encounter challenges of highly sensitivity to noise when measurement length is not infinity and have no non-asymptotic guarantee. Statistical methods [23, 41] typically rely on statistical information about an unknown source signal, which, in practice, require long recording duration to build up the statistical information.

In underwater acoustic channels, multichannel blind deconvolution methods also encounter challenges. For the coherent processing of noise recordings, the CIRs between two receivers can be estimated by cross-correlating long-duration ambient noise recordings from each channel [25]. Another approach, the Ray-Based Blind (RBD) deconvolution method, has been developed based on the beamforming technique using a receiver array [11]. However, a primary limitation of these acoustic imaging methods is their dependence on acoustic propagation effects and the long coherence emerging time for noise correlation techniques. Therefore, these methods sometimes cannot provide high resolution and fast recovery results. In our study, we aim to develop a method that can quickly deconvolve and track the system within a short recording time.

This chapter examines a sensing scenario under the multiple-channel framework (Fig. 1.1a), in which a network of distributed sensors (e.g., a vertical line array) listens to the same source (Fig. 1.1b). Compared to traditional multichannel blind deconvolution approaches, the proposed blind deconvolution approach does not rely on an accurate channel length estimation or any statistical information about the input source, so it can be used with short recording duration (e.g., a single snapshot). Instead, the proposed approach investigates the multichannel deconvolution problem as a low-rank matrix recovery problem, which significantly differs from the problem

formulation of the aforementioned blind deconvolution approaches. Compared to the recently developed single-channel blind deconvolution method using a similar formulation [26], the multichannel deconvolution method exploits the spatial diversity of CIRs across channels to solve the blind deconvolution problem without assume a generic model for the source.

Under the general deconvolution framework (Fig. 1.1a), the multichannel deconvolution problem is typically posed as a bilinear system of equations that can be recast as a system of linear equations whose solution has a rank-1 structural constraint. This system of linear equations is solved using the low-rank matrix recovery tools developed in recent years [31, 32]. The proposed approach estimates CIRs and source by solving an optimization program. This formulation has the advantage that a priori information about CIRs can be incorporated by adding constraints. Furthermore, this also allows us to use standard numerical techniques to solve the problem on a relatively large scale. The numerical experiments in Section 2.4 demonstrate recovery of 100 channels with 200 taps each from a source of length 1000. Additionally, when the dimension length of the subspace containing the admissible CIRs is consistent with the available a priori information, and it is small compared to the length of measurements, the blind deconvolution can be achieved using a small number of receivers.

The remainder of this chapter is organized as follows. Section 2.2 presents the theoretical formulation of the proposed blind deconvolution method based on recasting the multichannel deconvolution problem as a low-rank matrix recovery problem. A general formulation of the method based on the assumption that CIRs are time-limited is first introduced, and the formulation is then extended to CIRs that can be represented by a general linear model. Section 2.3 introduces a linear model for parameterizing multipath CIRs in ocean waveguides in order to incorporate a priori knowledge of the arrival-time structure of the CIR in the low-rank matrix re-

covery problem. Section 2.4 first investigates the performance and the robustness of the proposed deconvolution method using numerical simulations of general stylized channels such as time-limited channels and pulse-like channels. This section then presents numerical simulation results on realistic acoustic channels in an ocean waveguide and deconvolution result using at-sea data recorded in shallow water using bottom-mounted short vertical line arrays. Section 2.5 extends our multichannel blind deconvolution method to multiple-input-multiple-output system, and presents simulation results of blind source separation from convolutive measurements. Finally, Section 2.6 summarizes the findings of this chapter.

## 2.2 Multichannel Deconvolution

### 2.2.1 The sensing scenario

The multichannel deconvolution problem is illustrated in Fig. 1.1a. A common *source signal*  $s(t)$  drives  $M$  different channels with the CIR  $h_1(t), h_2(t), \dots, h_M(t)$ . Over a period of time, we observe samples of convolution outputs  $y_1(t), \dots, y_M(t)$ , where  $y_m(t) = s(t) * h_m(t)$ . From these observations alone, we wish to estimate both  $h_m(t)$  ( $m = 1, \dots, M$ ) and  $s(t)$ . This problem has direct application in ocean underwater acoustic passive sensing as shown in Fig. 1.1b: for instance, assuming sound from a shipping source that propagates towards each hydrophone based on each CIR  $h_m(t)$ . So under this model, each hydrophone from a vertical line array (forming multiple channels) listens to the same ship noise. The goal is to deconvolve the CIRs and the source by measuring only the outputs of a hydrophone array. This problem does not have a unique solution if we known nothing about the source signal  $s(t)$  or the CIR  $h_m(t)$ . However, if we make some structural assumptions about the channels, namely that they live in a subspace of some known lower dimension, then the problem, which becomes well posed, can be solved by a fast and scalable algorithm.

If we treat both the source  $s(t)$  and the CIR  $h_m(t)$  as unknowns, and our observations consist of linear combinations of entries of  $s(t)$  and the  $h_m(t)$  multiplied by one another, multichannel blind deconvolution is challenging since it is equivalent to solving a system of *bilinear equations*. To precisely state the problem, an inverse problem is written down using the language of linear algebra. We assume that both the  $s(t)$  and the  $h_m(t)$  are bandlimited, so recovering discretized samples  $h_m[k]$  of  $h_m(t)$  and  $s[k]$  of  $s(t)$ , spaced at the corresponding Nyquist rate or closer, is the same as recovering the CIRs themselves and the source (limited to this frequency band). We define the general convolution model as

$$y_m[\ell] = \sum_{n=-\infty}^{\infty} h_m[k]s[\ell - k], \quad \text{for } \ell = 0, 1, \dots, L - 1. \quad (2.1)$$

This problem does not have a unique solution if we assume  $s[k]$  and  $h_m[k]$  have no structure, because many signals and CIRs can produce the same observations  $y_m[\ell]$ . Even if we were to observe an infinite number of samples  $\{y_m[\ell], \ell \in \mathbb{Z}\}$  over an infinite amount of time and treat the channels jointly, the  $h_m[k]$  and  $s[k]$  would still not be identifiable.

### 2.2.2 Finite impulse response (FIR) channels

The story does improve, however, if we make structural assumptions about the CIR  $h_m[k]$ . For example, we might assume that the  $h_m[k]$  are time-limited (i.e., FIR channels) such that  $h_m[k]$  can be nonzero only for  $0 \leq k \leq K - 1$ . Then we can limit the index summation in the convolution model (2.1):

$$y_m[\ell] = \sum_{n=0}^{K-1} h_m[k]s[\ell - k], \quad \text{for } \ell = 0, 1, \dots, L - 1. \quad (2.2)$$

Eq. (2.2) has  $K + (L + K - 1) = L + 2K - 1$  unknowns, and  $L$  bilinear equations that combine these unknowns in different ways: each sample of  $y_m$  involves a

sum over products of various combinations of  $\{h_m[0], \dots, h_m[K-1]\}$  and  $\{s[-K+1], \dots, s[0], \dots, s[L-1]\}$ . Treating the channels jointly adds more equations and more unknowns. However, since the channels are all being driven by a common source, the number of unknowns is smaller than the number of equations. The system of equations corresponding to the observations  $\{y_m[\ell], \ell = 0, \dots, L-1; m = 1, \dots, M\}$  has  $ML$  equations and  $MK + (L + K - 1) = (M + 1)K + L - 1$  unknowns. Thus, when the number of channels  $M$  is large and  $L > K$ , the number of equations in fact are much larger than the number of unknowns.

Only comparing the number of equations to the number of unknowns does not tell the whole story, especially since the equations are non-linear (bilinear in the unknowns of  $\mathbf{s}, \mathbf{h}_1, \mathbf{h}_2, \dots, \mathbf{h}_M$ ). The observations above reveal in some loose sense that as the number of observations grows, so does the ratio of the information we have (equations) versus the information we do not (variables). We take another step towards formalizing this trade-off by recasting the bilinear equations in (2.2) as a system of linear equations with a rank constraint. The common source  $\mathbf{s} \in \mathbb{R}^{L+K-1}$  used in (2.2) and the CIR  $\mathbf{h}_m$  can be defined as a vector as below:

$$\mathbf{s} = \begin{bmatrix} s[-K+1] \\ \vdots \\ s[-1] \\ s[0] \\ s[1] \\ \vdots \\ s[L-1] \end{bmatrix}, \quad \mathbf{h}_m = \begin{bmatrix} h_m[0] \\ h_m[1] \\ \vdots \\ h_m[K-1] \end{bmatrix}. \quad (2.3)$$

Then we can arrange all pairs of variables appearing in the sum in (2.2) in a large

$(L + K - 1) \times KM$  matrix  $\mathbf{X}_0$ :

$$\mathbf{X}_0 = \begin{bmatrix} \mathbf{s} \end{bmatrix} \begin{bmatrix} \mathbf{h}_1^\top & \mathbf{h}_2^\top & \cdots & \mathbf{h}_M^\top \end{bmatrix} = \begin{bmatrix} \mathbf{s}\mathbf{h}_1^\top & \mathbf{s}\mathbf{h}_2^\top & \cdots & \mathbf{s}\mathbf{h}_M^\top \end{bmatrix}. \quad (2.4)$$

Each observation  $y_m[\ell]$ , an example of which is shown graphically in Fig. 2.1, is now a linear combination of entries in  $\mathbf{X}_0$ . Concatenating the observations from each channel into a single vector  $\mathbf{y} \in \mathbb{R}^{ML}$ , we form a linear system of equations

$$\mathbf{y} = \mathcal{A}(\mathbf{X}_0), \quad (2.5)$$

where  $\mathcal{A}$  takes sums over skew diagonals of submatrices  $\mathbf{s}\mathbf{h}_m^\top$ . We can write out this linear operator  $\mathcal{A}$  in the form of inner products against the rank-1 matrix  $\mathbf{X}_0 = \mathbf{s}\mathbf{h}^\top$ , where  $\mathbf{h} = [\mathbf{h}_1^\top, \mathbf{h}_1^\top, \dots, \mathbf{h}_M^\top]^\top$ .  $\mathbf{A}_{m\ell}$  is the skew-diagonal sum measurement matrix yielding observation  $y_m[\ell]$ , and we can write  $y_m[\ell]$  as below (an example of  $\mathbf{A}_{m\ell}$  is given in Eq. (2.14)).

$$y_m[\ell] = \sum_{i,j} A_{m\ell}[i,j] X_0[i,j] = \text{trace}(\mathbf{X}_0^\top \mathbf{A}_{m\ell}) = \langle \mathbf{A}_{m\ell}, \mathbf{X}_0 \rangle. \quad (2.6)$$

Then for all measurements across channels, we form the following expression

$$\mathbf{y} = \begin{bmatrix} y_1[0] \\ y_1[1] \\ \vdots \\ y_M[L-1] \end{bmatrix} = \mathcal{A}(\mathbf{X}_0) = \begin{bmatrix} \langle \mathbf{A}_{10}, \mathbf{X}_0 \rangle \\ \langle \mathbf{A}_{11}, \mathbf{X}_0 \rangle \\ \vdots \\ \langle \mathbf{A}_{M(L-1)}, \mathbf{X}_0 \rangle \end{bmatrix}. \quad (2.7)$$

We can now treat the recovery of the CIR  $\mathbf{h}_m$  and the source  $\mathbf{s}$  as a *matrix recovery* problem. The vector  $\mathbf{y}$  contains  $ML$  different linear combinations of entries

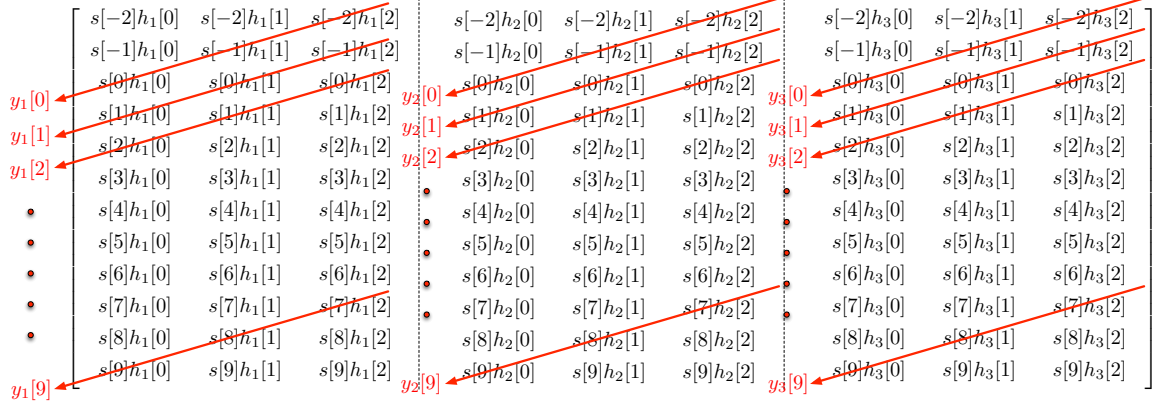


Figure 2.1: To illustrate the proposed approach, the matrix  $\mathbf{X}_0$  defined in Eq. (2.4) is explicitly written with a number of measurements per channel of  $L = 9$ , channel length  $K = 3$ , and a number of channels  $M = 3$ . Each observation  $y_m[\ell]$  is a sum along one of the skew diagonals of the a submatrix of  $\mathbf{X}_0$ , as illustrated by the red lines above. Recovering an  $(L + K - 1) \times KM$  matrix from measurements of this type is virtually impossible, but explicitly incorporating the fact that  $\mathbf{X}_0$  has rank-1 structure into the recovery makes the recovery possible for appropriate values of  $L, K, M$ .

of an  $(L + K - 1) \times KM$  matrix. Regardless of the values of  $L, K$ , and  $M$ , the number of equations will always be less than the entries in the unknown matrix, indicating that the system of linear equations in Eq. (2.5) is underdetermined. However, because the underlying matrix  $\mathbf{X}_0$  can be written as the outer product of two vectors (as in Eq. (2.4)), it has a special structure, whose rank is 1. To recover  $\mathbf{X}_0$  from  $\mathbf{y}$ , we might search for a  $(L + K - 1) \times KM$  matrix that satisfies

$$\mathcal{A}(\mathbf{X}) = \mathbf{y}, \quad \text{rank}(\mathbf{X}) = 1. \quad (2.8)$$

For an arbitrary  $\mathbf{y}$ , a solution  $\tilde{\mathbf{X}}$  that satisfies the constraints above exactly may or may not exist. Given  $\mathbf{y}$ , we might search instead for such a feasible solution  $\tilde{\mathbf{X}}$  by solving

$$\min_{\mathbf{X}} \text{rank}(\mathbf{X}) \quad \text{subject to} \quad \mathcal{A}(\mathbf{X}) = \mathbf{y}. \quad (2.9)$$



### 2.2.3 The heuristic solver

The deconvolution problem is now recast as a low-rank matrix recovery problem, which can then be solved using low-rank matrix recovery tools developed in recent years, such as nuclear norm minimization, low-rank approximation, iterative hard thresholding and alternating methods [28]. Results of prior studies in the area of low-rank matrix recovery have identified effective convex relaxations [29, 30] for problems of this type and efficient, scalable heuristic solvers that enable these techniques to work with thousands of unknown variables. A description of the heuristic solver used in this chapter is discussed below. The Burer-Monteiro heuristic solver is based on the low-rank factorization method and notably efficient in memory. Numerical simulations using this solver are presented in Section 2.4 .

The multichannel deconvolution problem via recovery a low-rank matrix becomes computationally intractable as the number of channels increases. To recover  $\mathbf{X}_0$ , we are searching over a matrix of size  $(L + K - 1) \times KM$  that minimizes the nuclear norm which satisfies the linear constraints. If we want to recover  $M = 100$  channels with each channel of length  $K = 500$ , and a source of length  $L + K - 1 = 1000$ , then the rank-1 matrix  $\mathbf{X}_0$  is of size  $1000 \times 50000$ , which the storage becomes an issue in computation. However, the nonlinear programming algorithm developed by Burer and Monteiro [32], using low-rank factorization can greatly reduce the number of variables, and in the meanwhile, provides reliable performance adapted in our application.

By construction, we know that the target matrix  $\mathbf{X}_0$  is rank-1, so instead of iterating matrix  $\mathbf{X}$  of size  $(L + K - 1) \times KM$  to minimize its nuclear norm, we can reformulate the problem to optimize over vectors  $\mathbf{Z} \in \mathbb{R}^{(L+K-1) \times 1}$  and  $\mathbf{H} \in \mathbb{R}^{KM \times 1}$ , where  $\mathbf{X} = \mathbf{Z}\mathbf{H}^\top$  (Note that  $\mathbf{Z}$  and  $\mathbf{H}$  correspond to the source signal vector  $\mathbf{s}$  and CIR vectors  $\mathbf{h}$  in Eq. (4) respectively). Hence we only need to store two vectors  $\mathbf{Z}$  and  $\mathbf{H}$  in the memory for each iteration. This reformulation is driven by the fact

that the nuclear norm is equal to the minimum Frobenius norm factorization:

$$\|\mathbf{X}\|_* = \min_{\mathbf{Z}, \mathbf{H}} \frac{1}{2}(\|\mathbf{Z}\|_F^2 + \|\mathbf{H}\|_F^2) \quad \text{subject to} \quad \mathbf{X} = \mathbf{Z}\mathbf{H}^\top. \quad (2.10)$$

We can then minimize the following augmented Lagrange term:

$$\|\mathbf{Z}\|_F^2 + \|\mathbf{H}\|_F^2 - 2\langle \boldsymbol{\lambda}, \mathcal{A}(\mathbf{Z}\mathbf{H}^\top) - \mathbf{y} \rangle + \sigma \|\mathcal{A}(\mathbf{Z}\mathbf{H}^\top) - \mathbf{y}\|_2^2. \quad (2.11)$$

This new formulation of the problem is non-convex because  $\mathcal{A}(\mathbf{Z}\mathbf{H}^\top)$  is a linear combination of the product of two unknowns. But the Burer-Monteiro heuristic shows that under certain conditions, the local minima in Eq. (2.11) are also the global minima [33]. This Burer-Monteiro heuristic solver is used in state-of-the-art large scale implementations of matrix recovery problems. To minimize the augmented Lagrangian term in Eq. (2.11), the inner operation is executed using Limited-memory Broyden-Fletcher-Goldfarb-Shanno algorithm (LBFGS) with Matlab solver ‘minfunc’ developed by Recht, Fazel and Parrilo [31]. The parameters of the augmented Lagrangian are updated according to the schedule proposed by Burer and Monteiro [32]. The parameter  $\boldsymbol{\lambda}$  determines the trade-off between the fidelity of the solution to the measurements  $\mathbf{y}$  and its conformance to the model. The term involving  $\sigma$  measures the Euclidean norm of the infeasibility, and  $\sigma$  is a penalty parameter. We update both parameters for each LBFGS minimization.

We also use a gradient-based algorithm because the function and the gradient evaluations of the augmented Lagrange term Eq. (2.11) with respect to vectors  $\mathbf{Z}, \mathbf{H}$  can be performed very quickly. We can write out how we compute the gradient of the augmented Lagrange term as below. We denote the objective function as  $f(\mathbf{Z}, \mathbf{H})$ , where

$$f(\mathbf{Z}, \mathbf{H}) = \|\mathbf{Z}\|_F^2 + \|\mathbf{H}\|_F^2 - 2\langle \boldsymbol{\lambda}, \boldsymbol{\Delta} \rangle + \sigma \|\boldsymbol{\Delta}\|_2^2$$

where  $\Delta = \mathcal{A}(\mathbf{Z}\mathbf{H}^\top) - \mathbf{y}$ . It then can be calculated that

$$\nabla_{\mathbf{Z}} f(\mathbf{Z}, \mathbf{H}) = 2(\mathbf{Z} - [\mathcal{A}^*(\boldsymbol{\lambda} - \sigma\Delta)]\mathbf{H})$$

and

$$\nabla_{\mathbf{H}} f(\mathbf{Z}, \mathbf{H}) = 2(\mathbf{H} - [\mathcal{A}^*(\boldsymbol{\lambda} - \sigma\Delta)]^*\mathbf{Z})$$

where  $\mathcal{A}^*$  is the adjoint of  $\mathcal{A}$  and also can be implemented through Fast Fourier Transform.

#### 2.2.4 A general linear model for the CIR

The linear operator  $\mathcal{A}$  in the previous section was derived from the assumption that the CIR is time-limited, so the length of each CIR is  $K$ . More generally, we can incorporate a priori information about the CIR (e.g., expected arrival-time structure in a multipath environment) into a general linear model, that is, we can assume each CIR  $\mathbf{h}_m$  can be written as

$$\mathbf{h}_m = \mathbf{C}_m \mathbf{u}_m, \quad m = 1, \dots, M, \quad (2.12)$$

where  $\mathbf{C}_m \in \mathbb{R}^{K \times D}$ ,  $\mathbf{u}_m \in \mathbb{R}^D$  is the coefficient vector,  $K$  is the length of the vector  $\mathbf{h}_m$ , and  $D$  is the number of columns of the matrix  $\mathbf{C}_m$ . Therefore, the CIR  $\mathbf{h}_m$  lives in a subspace that is the linear span of the columns of the matrix  $\mathbf{C}_m$ . The time-limited CIR example in the previous section is a special case, which corresponds to  $\mathbf{C}_m = \mathbf{I}^{K \times K}$ . We shall note here the length of the channel  $K$  no longer needs to satisfy the constraint  $L > K$ , but we require that the length of the channel coefficient vector  $D$  satisfies  $L > D$ , since the number of unknowns of the CIR per channel is now  $D$  instead of  $K$ .

Let us concatenate all the CIR vectors  $\{\mathbf{h}_m\}$  together, as well as the coefficient

vectors  $\{\mathbf{u}_m\}$ , we write the linear model for multiple channels in a concise way:

$$\underline{\mathbf{h}} = \mathbf{C}\underline{\mathbf{u}}, \quad (2.13)$$

where

$$\mathbf{C} := \begin{bmatrix} \mathbf{C}_1 & \mathbf{0} & \dots & \mathbf{0} \\ \mathbf{0} & \mathbf{C}_2 & \dots & \mathbf{0} \\ \vdots & \vdots & \ddots & \vdots \\ \mathbf{0} & \mathbf{0} & \dots & \mathbf{C}_M \end{bmatrix}, \quad \underline{\mathbf{h}} = \begin{bmatrix} \mathbf{h}_1 \\ \mathbf{h}_2 \\ \vdots \\ \mathbf{h}_M \end{bmatrix}, \quad \text{and} \quad \underline{\mathbf{u}} = \begin{bmatrix} \mathbf{u}_1 \\ \mathbf{u}_2 \\ \vdots \\ \mathbf{u}_M \end{bmatrix}.$$

With the subspace model in place, the goal is now to recover the source  $\mathbf{s}$  and the channel subspace coefficients  $\mathbf{u}_1, \mathbf{u}_2, \dots, \mathbf{u}_M$ . As before, we recast this problem as recovering the rank-1 matrix  $\mathbf{X}_0 = [\mathbf{s}\mathbf{u}_1^\top \quad \mathbf{s}\mathbf{u}_2^\top \quad \dots \quad \mathbf{s}\mathbf{u}_M^\top]$ . Each observation  $y_m[\ell]$  is again a linear combination of the entries in  $\mathbf{X}_0$ . Here the new linear operator  $\mathcal{A}$  is implemented with the channel model embedded. For example, we can write out explicitly how to calculate  $y_m[0]$  using linear algebra with  $K = 4$ :

$$y_m[0] = \begin{bmatrix} \mathbf{s}^\top \end{bmatrix} \begin{bmatrix} 0 & 0 & 0 & 1 \\ 0 & 0 & 1 & 0 \\ 0 & 1 & 0 & 0 \\ 1 & 0 & 0 & 0 \\ 0 & 0 & 0 & 0 \\ \vdots & \vdots & \vdots & \vdots \\ 0 & 0 & 0 & 0 \end{bmatrix} \begin{bmatrix} \mathbf{h}_m \end{bmatrix} = \langle \mathbf{A}_{m1}, \mathbf{s}\mathbf{u}_m^\top \rangle, \quad \mathbf{A}_{m1} = \begin{bmatrix} 0 & 0 & 0 & 1 \\ 0 & 0 & 1 & 0 \\ 0 & 1 & 0 & 0 \\ 1 & 0 & 0 & 0 \\ 0 & 0 & 0 & 0 \\ \vdots & \vdots & \vdots & \vdots \\ 0 & 0 & 0 & 0 \end{bmatrix} \mathbf{C}_m. \quad (2.14)$$

In this case, each measurement matrix is the corresponding skew diagonal sum matrix times the channel subspace matrix. We still keep the general notation  $\mathbf{y} = \mathcal{A}(\mathbf{X}_0)$  the same.

## 2.3 Linear Models for Multipath CIR in Ocean Waveguides

In the previous section, the multichannel deconvolution problem has been recast as a low-rank matrix recovery problem, and we require the ambient dimension of the measurements to be bigger than the dimension of the CIR to solve the problem. Because a priori knowledge of the CIR is usually available, dimension reduction of the CIR using a linear model is possible. For instance, in an ocean waveguide, an accurate linear model for CIRs can be fit using a priori knowledge of the environmental parameters (expected variations of the sound-speed profile) and the source-receiver configuration [34]. Incorporating a linear model for CIRs reduces the dimension of the subspace spanned by the admissible CIRs such that the deconvolution becomes more tractable numerically. Two types of linear models for the CIR in ocean waveguides are discussed below.

### 2.3.1 The multipath CIR with known arrival-times and unknown amplitudes

Our first CIR model, based on the ray approximation, assumes that the CIR consists of multiple pulses that arrive at different time delays with different amplitudes. This model can be interpreted as the same pulse emitted from a common source but taking multiple paths to reach the receivers, as illustrated in Fig. 1.1b. The CIR  $h_m(t)$  can be written as a sum of pulse function  $p(t)$  with different delays  $t_1, t_2, \dots, t_D$  and different amplitudes  $u_m[1], u_m[2], \dots, u_m[D]$ :

$$h_m(t) = u_m[1]p(t - t_1) + u_m[2]p(t - t_2) + \dots + u_m[D]p(t - t_D). \quad (2.15)$$

In this CIR linear model, we know the pulse profile  $p(t)$  (as an example, we assume the pulse is a band-limited Gaussian-windowed sinusoid  $p(t) = u \cdot \sin(2\pi f_c t) e^{-(\frac{t}{\tau})^2}$ , and the decay parameter  $\tau$  is determined by the effective bandwidth of the pulse)

and pulse time delays  $t_1, t_2, \dots, t_D$  as the a priori information, and the unknowns are the amplitude coefficients  $u_m[1], u_m[2], \dots, u_m[D]$  of each ray-like arrivals.  $h_m(t)$  and  $p(t - t_d)$  can be discretized in vector forms as  $\mathbf{h}_m \in \mathbb{R}^K$  and  $\mathbf{p}_{t_d} \in \mathbb{R}^K$ . In terms of linear algebra, Eq.(2.15) implies that the CIR  $\mathbf{h}_m$  lies in  $D$ -dimension subspace spanned by vectors  $\mathbf{p}_{t_1}, \mathbf{p}_{t_2}, \dots, \mathbf{p}_{t_D}$  instead of the  $K$ -dimension vector length ( $D < K$ ). The subspace matrix  $\mathbf{C}_m \in \mathbb{R}^{K \times D}$  for the CIR  $\mathbf{h}_m$ , which is explained in Eq.(2.12), is simply constructed by stacking  $D$  time-domain pulse basis vectors column-wise. Therefore,  $\mathbf{C}_m$  can be written as

$$\mathbf{C}_m = \begin{bmatrix} \mathbf{p}_{t_1} & \mathbf{p}_{t_2} & \dots & \mathbf{p}_{t_D} \end{bmatrix}. \quad (2.16)$$

### 2.3.2 The multipath CIR with uncertain arrival-times and unknown amplitudes

In practice, the arrival-time structure of the CIR in ocean waveguides is never known exactly as a result of environmental fluctuations (e.g., sound speed variations). However, assuming that the range of expected sound-speed variations can be estimated, using for instance an oceanographic model, we can assume that the arrival-times  $t_i$  ( $i = 1 \dots D$ ) for each ray arrival lies within a known time-interval  $\Delta t_i$ , that is, each ray arrival might occur within the time window  $t_i \pm \Delta t_i$ . Examining all possible pulses that arrive within one time interval  $t_i \pm \Delta t_i$  shows that they form a collection of shifted pulses that lie on a certain region of a manifold. Depending on the range of the time interval, the region of the manifold differs. Now the model for pulses on the manifold in terms of the arrival-time is nonlinear. The manifold needs to be embedded into a linear model that can approximate the CIR by a linear subspace with preferably a low dimension so that the deconvolution method can be implemented. Since all the pulses that lie on the manifold are highly correlated, principal component analysis (PCA) is performed here to build a low dimension linear subspace for

all shifted pulses.

A systematic way to construct the lower dimension subspace based on PCA is introduced in this section. An over-complete subspace matrix, denoted by  $\mathbf{B}_{1o}$ , is first formed by column-wise stacking vectors that represent all pulses arriving within the time interval  $t_i \pm \Delta t_i$ . Using the same notation as the previous section for shifted pulse basis vectors, we form the matrix  $\mathbf{B}_{1o}$  as

$$\mathbf{B}_{1o} = \begin{bmatrix} \mathbf{p}_{t_1+\Delta t_i} & \mathbf{p}_{t_1+\Delta t_i-\delta t} & \cdots & \mathbf{p}_{t_1-\Delta t_i+\delta t} & \mathbf{p}_{t_1-\Delta t_i} \end{bmatrix},$$

where  $\delta t$  is a tiny shifting grid for each pulse. However, all those time-shifted pulses (i.e., Fig. 2.2a is an example of those shifted pulses) are highly correlated. We then perform a principal component analysis using a singular value decomposition of this collection of shifted pulse basis vectors to reduce its dimension, resulting in a low-dimension linear model for approximating any pulse arriving in this time region. The matrix  $\mathbf{B}_{1o}$  can be written as  $\mathbf{B}_{1o} = \mathbf{U}\mathbf{S}\mathbf{V}^\top$ . Because the singular value spectrum of this matrix decays to near zero quickly as shown in Fig. 2.2b, we only need the first  $R$  ( $R$  is a small number in this typical example) singular values of  $\mathbf{B}_{1o}$  to capture nearly all energy (more than 99.999% in simulation) of the singular values. Then the  $R$  corresponding singular vectors (i.e., Fig. 2.2c is an example of the first  $R = 6$  singular vectors) form the basis of the low dimension subspace. Column-wise stacking of these  $R$  singular vectors generates a matrix  $\mathbf{B}_1$  that can accurately represent any pulse that arrives within the time region  $t_1 \pm \Delta t$ . The matrix  $\mathbf{B}_1$  is written as

$$\mathbf{B}_1 = [\mathbf{U}(:, 1), \dots, \mathbf{U}(:, R)]. \quad (2.17)$$

The same procedure is performed for each path of the CIR and generates corresponding  $\mathbf{B}_2, \dots, \mathbf{B}_D$  for each time region. Finally, the subspace matrix  $\mathbf{C}_m$ , introduced

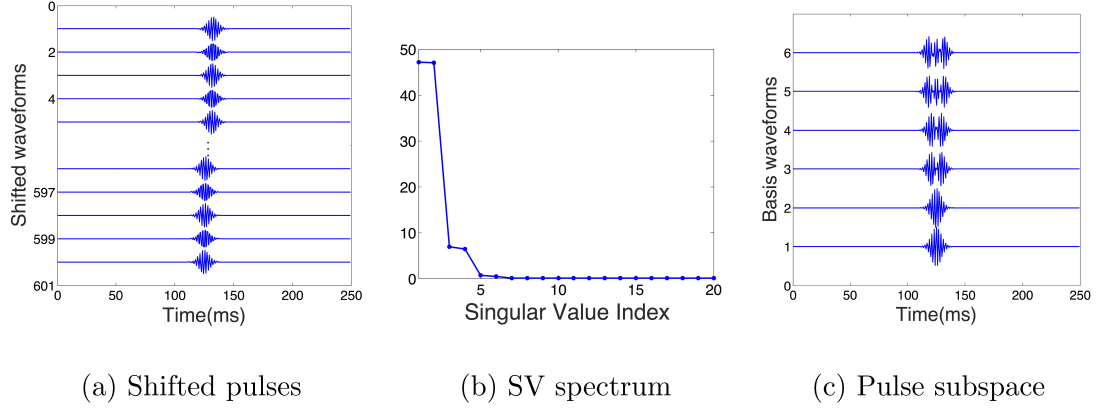


Figure 2.2: (a) An illustration of the small time shifts of a band-limited basis pulse (400 – 600 Hz). All shifted pulses form an over-complete subspace matrix  $\mathbf{B}_{1o}$  for any ray-like pulse that arrives within an uncertainty window of duration  $\Delta t = 3$  ms. (b) The singular value spectrum of the corresponding over-complete matrix  $\mathbf{B}_{1o}$ . The plot contains the first 20 of 600 singular values. The first  $R = 6$  singular values capture more than 99% of the total energy. (c) The pulse subspace matrix  $\mathbf{B}_1$ , consisting of the  $R = 6$  principal components of  $\mathbf{B}_{1o}$ .

in Eq.(2.12) for the CIR  $\mathbf{h}_m$  is then formed by

$$\mathbf{C}_m = [\mathbf{B}_1, \mathbf{B}_2, \dots, \mathbf{B}_D]. \quad (2.18)$$

Because of the uncertainty of the paths' arrival-time, the CIR  $\mathbf{h}_m$  is approximated by a subspace with the dimension  $R \times D$  compared to a subspace of the dimension  $D$  in Eq.(2.16).

We need to point out that PCA is not the only method of finding the low dimension subspace for pulses that arrive within a known time region. Based on the a priori information of the CIR structure, other efficient subspaces that can approximate  $\mathbf{h}_m$  with a linear model also exist. For example, the discrete prolate spheroidal sequences [42] can form a highly efficient basis that represents band-limited and time concentrated pulses, which can also be an adequate linear model for the current application.



## 2.4 Numerical Results

In this section, the multichannel blind deconvolution method is implemented on various types of channel structures and the effectiveness and robustness of the deconvolution algorithm are demonstrated for both stylized and realistic CIRs. In simulations, the common driving source signal,  $\mathbf{s} \in \mathbb{R}^{L+K-1}$ , where  $L + K - 1 = 1000$ , is Gaussian white noise filtered in an arbitrary bandwidth representative of shipping noise spectra (400 – 600 Hz) with a sampling frequency  $f_s = 2000$  Hz.

### 2.4.1 Stylized simulations

Stylized channel structures introduced in Section 2.2 and 2.3 are simulated in this section as direct implementations of the proposed deconvolution method. These general CIR assumptions do not directly represent any specific underwater acoustic channels but more general type of channel models. Realistic underwater acoustic channel simulations will be discussed later in Section 2.4.3.

#### 1. Time-limited channels

The first simulation investigates the time-limited channel model that corresponds to the scenario illustrated in Fig. 2.1. For time-limited channels, CIR vectors  $\mathbf{h}_1, \dots, \mathbf{h}_M \in \mathbb{R}^K$  have finite length, which means that elements of the CIR vector  $h_m[k]$  are nonzero only for  $0 \leq k \leq K - 1$  and they are normally distributed random variables (i.e., FIR channels). Fig. 2.3 illustrates a typical recovery result for parameters  $K = 200$  (the CIR vector length) and  $M = 100$  (number of recording channels). In this case, both the source signal and all of the CIRs (21000 variables) are recovered with relatively small errors from 100 observed outputs (100,000 total samples). The blind deconvolution method here benefits from having totally unstructured CIRs, which efficiently increases the mixing of the source signal and CIRs and thus the diversity of observations in the  $M = 100$  recording signals.

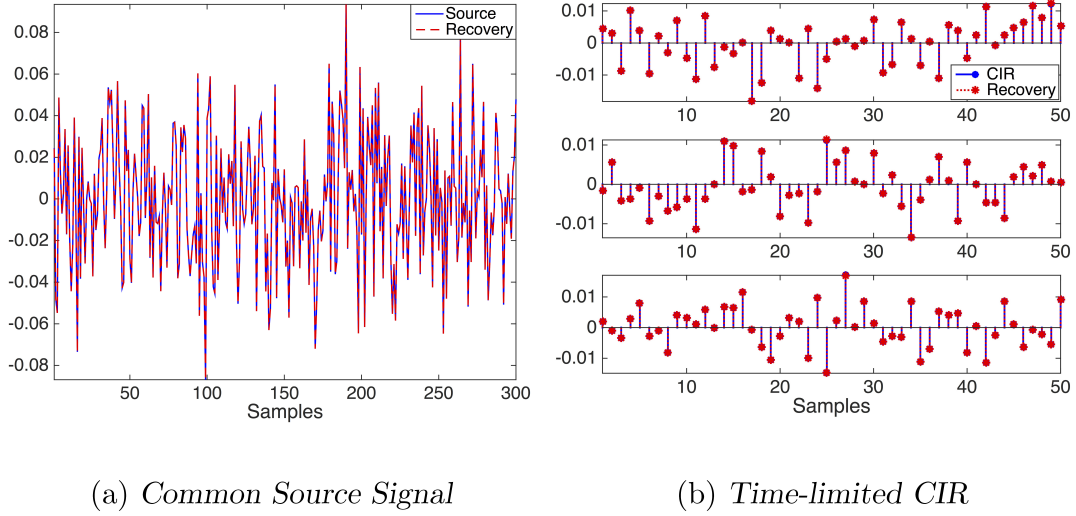


Figure 2.3: Examples of recovery for finite-duration CIRs ( $K = 200$  taps) using  $M = 100$  channels. (a) Comparison of the original source signal (solid line) and the recovered source signal (dashed line). The relative error is  $3 \times 10^{-5}$  (only the first 300 samples out of 1000 samples are plotted). (b) Comparison of the true underlying CIRs (plotting only first 50 taps out of  $K = 200$  for the first 3 channels) and the recovered CIRs. The average relative error across all 100 channels is  $10^{-4}$ .

## 2. Channels with known arrival-times and unknown amplitudes

To examine the method proposed in Section 2.3.1, we implement a general linear model for CIRs with finite number of discrete arrivals with a priori known arrival-times but unknown amplitudes. This linear model is realized for multipath channels in an ocean waveguide as introduced in Section 2.3. In this simulation scenario, each CIR consisted of three different individual pulse arrivals that correspond to  $D = 3$ , defined in Section 2.3.1. The basis pulse  $p(t)$  throughout the rest of simulations is defined as a Gaussian window pulse in the frequency band of 400 – 600 Hz. The length of the CIR vector is  $K = 500$ , and the number of channels is  $M = 50$ . Because accurate time delays  $t_{1m}, t_{2m}, t_{3m}$  for each pulse are assumed to be known, we only need to estimate the amplitudes of each pulse, which are  $u_m[1], u_m[2], u_m[3]$ .

Simulation results presented in Fig. 2.4a demonstrate the exact deconvolution of the first 5 CIRs (The common source signal is also exactly recovered as in Fig.

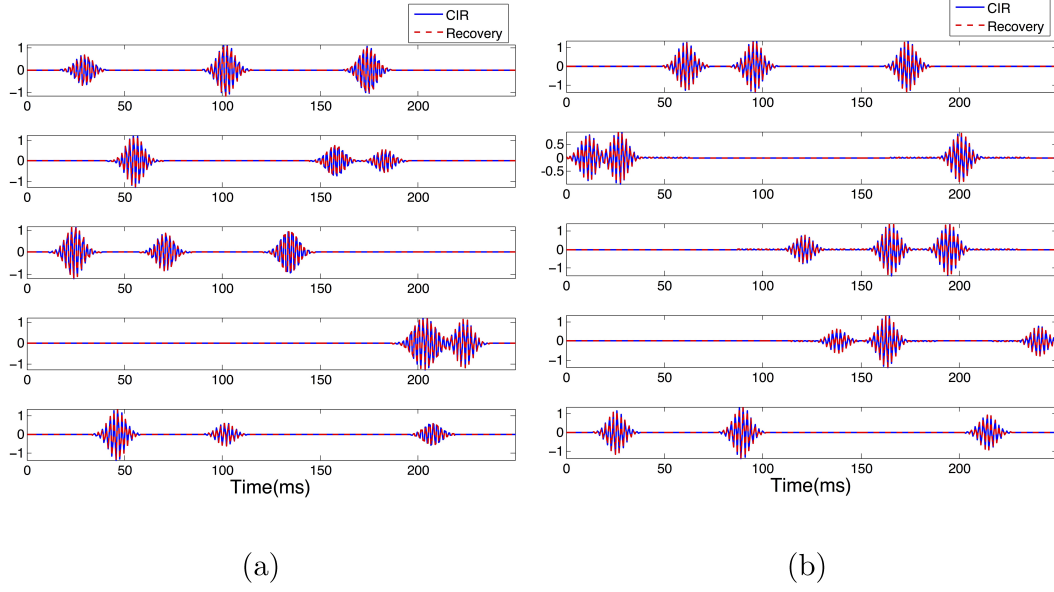


Figure 2.4: (a) Comparison of the actual CIR and recovered CIR for 5 channels assuming known arrival-times and unknown amplitudes for the 3 pulse-like arrivals of each CIR. The average relative error across all  $M = 50$  channels is  $2 \times 10^{-10}$ . (b) Same as (a) but assuming uncertain arrival-times ( $\Delta t = 1.5$  ms) and unknown amplitudes. The average relative error across all  $M = 50$  channels is  $3 \times 10^{-5}$ .

2.3a, but not plotted in Fig. 2.4). The method proposed in this chapter yields accurate performance if the CIR linear channel model is precise and the dimension of the subspace representing the model is small. The multipath CIR model is only one special example commonly applied in the ocean waveguide. Another typical channel model in other applications is *sparse* channel, that is, each CIR has  $D$  non-zero components at known sparse locations, but we do not know the corresponding amplitudes at each location [43].

### 3. Channels with uncertain arrival-times and unknown amplitudes

The channel model introduced in Section 2.3.2 assuming uncertain arrival-times and unknown amplitudes is examined hereafter. Parameters of the simulation are similar to those used in the previous section except that the arrival-times of each pulse-like arrival of each CIR can lay anywhere within the time interval  $t_i \pm \Delta t$  ( $i = 1 \dots D$ ), assuming the same uncertainty window  $\Delta t = 1.5$  ms for all arrivals for

the sake of simplicity. The uncertainty of the arrival-time increases the dimension of the subspace that represents the CIR, and yields a small model error in representing CIRs because of truncating insignificant singular values. The results in Fig. 2.4b demonstrate that the method still accurately estimated the CIR.

## 2.4.2 Robustness analysis

### 1. The effect of additive measurement noise

The recovery performance in the presence of additive measurement noises is examined in this section. Gaussian measurement noise  $e_m(t)$  is added on each channel's convolution measurements  $y_1(t), \dots, y_M(t)$ . In this simulation, the CIR model is the same as in the previous section. The recovery error and measurement noise are plotted in a log-log scale in Fig. 2.5. The measurement signal-to-noise ratio (SNR) is defined as  $\text{SNR} = 20\log_{10}(\|\mathbf{y}_m\|_2/\|\mathbf{e}_m\|_2)$ , and the CIR recovery relative error is defined as  $20\log_{10}(\|\mathbf{h}_m\|_2/\|\mathbf{h}_m - \mathbf{h}_{m_{\text{Approx}}}\|_2)$ . The result shows that our algorithm is robust to additive noise: as the noise level increases, no catastrophic failure occurs, and the recovery error grows linearly. Hence, the proposed deconvolution method recovers the CIR and the source accurately, and the performance is robust to noise when a linear model represented by Eq. (2.12) exists.

### 2. The effect of model errors

In the real environment, we usually encounter not only the measurement noise, but also model errors that are caused by lack of accurate a priori information to build an exact linear model for the CIR. The model error incurred in representing the CIR by the subspace matrix can be defined as  $\mathbf{h}_m = \mathbf{C}_m \mathbf{u}_m + \mathbf{e}_m$ . In the simulation, the channel model error is generated under the assumption that we do not have information about the later and weaker arrival pulses: in typical shallow water environments, those later arrivals have significantly weaker amplitudes and more randomly distributed arrival-times, when compared to the earlier arrivals, as

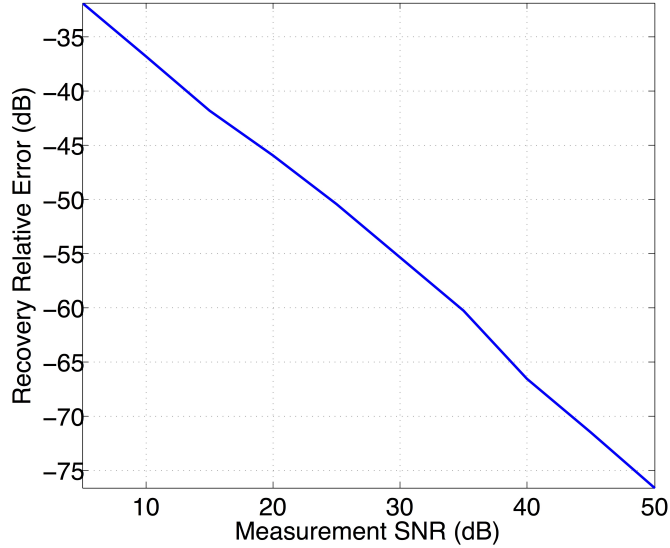


Figure 2.5: Variations of the recovery error (in logarithmic scale) for the deconvolution method (averaged over 100 independent realizations) vs. SNR of the recorded measurements.

they correspond to ray paths cumulating more reflections from the absorbing ocean bottom and the fluctuating ocean surface. For example, the true CIR shown in Fig. 2.6a consists of 5 pulses that arrive at time  $t_1, t_2, t_3, t_4, t_5$ , but the a priori information only provides the knowledge of the first 3 pulses that arrive at time  $t_1, t_2, t_3$ . The linear model that is generated by only incorporating stronger ray arrivals at time  $t_1, t_2, t_3$  would introduce model error in approximating the true CIR. The best approximation for the CIR is also depicted in Fig. 2.6a. Channel model error is defined as the normalized euclidean distance between the true CIR and CIR approximation using the linear model, which is  $20\log_{10}(\|\mathbf{h}_m\|_2/\|\mathbf{e}_m\|_2)$ . Figure. 2.6b illustrates the method is also robust to this type of channel model error if the model error (averaged here over 100 independent realizations) is within an upper bound of  $\approx 10\text{dB}$ . It is worth noting that the model error  $\mathbf{e}_m$  can be generated and measured by other variables as well. For example, the model error can be caused by a tilted array other than a perfect vertical array, therefore, the accuracy of a priori information will depend on a variable that measures the overall array tilt or individual receiver locations more

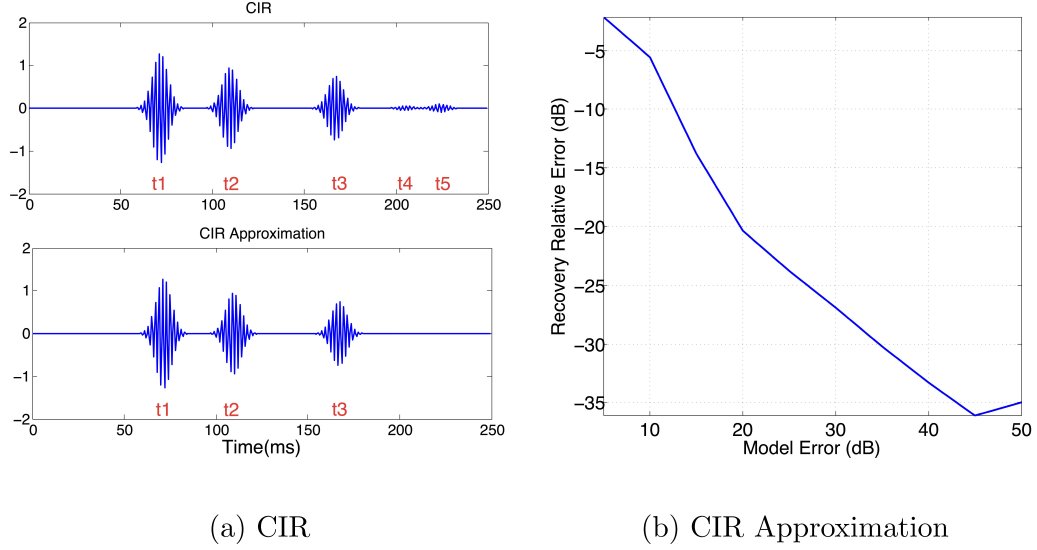


Figure 2.6: (a) Example of channel model error caused by lack of accurate a priori information on the arrival-time structure of the actual CIR (upper plot) containing 5 arrivals. Lower plot shows the approximated CIR assuming only 3 arrivals are present. (b) Variations of the recovery error (in logarithmic scale) for the deconvolution method (averaged over 100 independent realizations) vs. channel model error.

generally.

### 2.4.3 Numerical simulations in an ocean waveguide

In this section numerical simulations are conducted in a generic shallow water environment to assess the performance of the blind deconvolution method for the case of a surface source arbitrarily set at depth of 5 m, which represents a shipping source. This source is assumed to broadcast Gaussian white noise filtered in the frequency band 400 – 600 Hz as a simple model for shipping noise [44]. Figure 2.7a describes the shallow water environment used for the simulations. All environmental parameters including the sound speed profile (Fig. 2.7)b were selected to be representative of the experimental scenario and the actual environment introduced in the next section. Additionally, as implemented in the actual at-sea experiment, only a very short bottom-mounted vertical linear array (VLA) with 16 elements and 1-m spac-

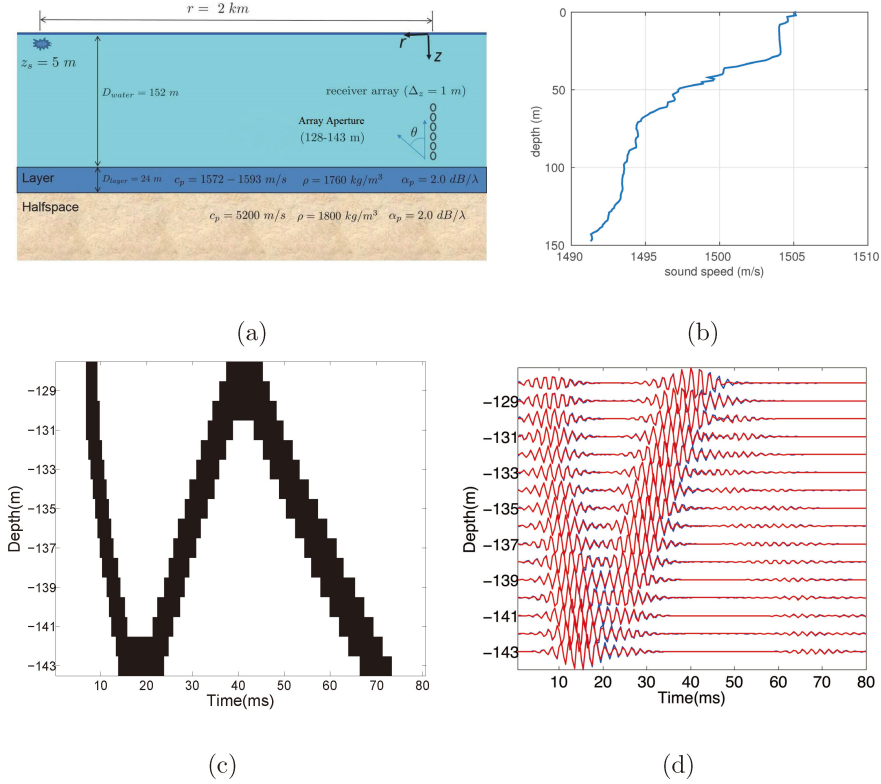


Figure 2.7: (a) Computational shallow water waveguide. (b) Experimentally-measured sound speed profile. (c) A priori information of the ray arrival-time structure of the CIRs for  $M = 16$  channels. For each ray arrival, the width of the black shaded area indicates the duration of the corresponding uncertainty time-window  $2\Delta t$  for the shallow source shown in (a). (d) Comparison of the actual CIRs (blue solid line) obtained from normal-mode simulations and the recovered CIRs (red dashed line) across all  $M = 16$  channels using the deconvolution method for the shallow source shown in (a). The average relative error across all  $M = 16$  channels is  $\approx 10^{-1}$ .

ing located from 128 m to 143 m deep were simulated here. The range between the source and the VLA elements was arbitrarily set to 2 km and the corresponding CIR waveforms were computed using the normal-mode formulation implemented with the software KRAKEN (Fig. 2.7c, blue line) [45].

A priori information of the ray arrival-time structure of the CIRs was obtained independently from a simple ray tracing simulation, using the standard BELLHOP model, and used for the CIR parametrization discussed in Section 2.3 (Fig. 2.7b) (note that no amplitude information for the various paths was used and that the ray simulations do not account for any dispersive effects presented in the actual

CIR waveforms computed from normal-mode simulations). A classic shallow-water multipath structure can be observed where for instance the first wavefront corresponds to the direct and first surface-bounced arriving nearly simultaneously for this very shallow source. The uncertainty time window of each simulated ray arrival (of up to  $\Delta t = 7$  ms) corresponds to variations of the sound-speed profile of  $\pm 3$  m/s which are representative of the expected variations of the environmental parameters at the experimental site described in the next section. The ray arrival-time intervals are then further combined if their corresponding uncertainty windows overlaps. The resulting ray arrival-time uncertainty windows are then used to construct the CIR subspace using the same method described in Section 2.3.2. Figure 2.7d shows that a small relative error of more than  $-20$ dB is achieved with the CIRs estimated from blind deconvolution (red dashed line) when compared to the original CIRs computed from normal-mode simulations (blue solid line) even though the a priori information we have about the CIRs is not very accurate in this shallow-ocean acoustic channel application (i.e., resulting in fairly large uncertainty time window of up to  $\Delta t = 7$  ms).

Furthermore, Fig. 2.8 demonstrates that similar performance can be achieved even when we reduce the number of recording channels to only 8 and 4 channels. These simulation results indicate that the proposed deconvolution method can be used with a very limited number of receivers, provided that fairly accurate a priori information of the arrival-time structure of the CIR is available. This means that our blind deconvolution method doesn't require a dense array to perform well, which is advantageous in comparison to some traditional deconvolution methods such as ray-based deconvolution (RBD) method [11] which not only it needs a long aperture, but the array should also be relatively dense with appropriate element spacing for beamforming to work.



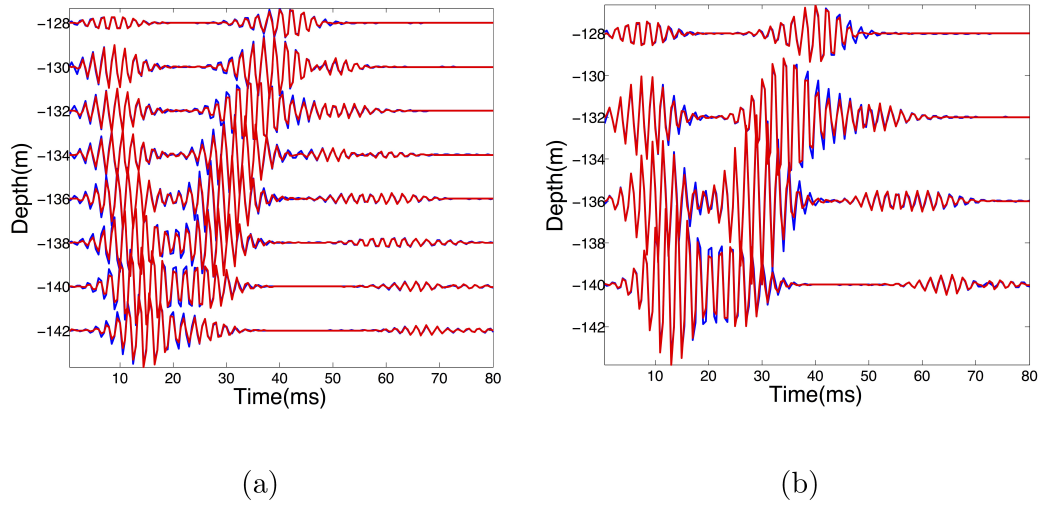


Figure 2.8: *Using only the simulated-received waveforms on (a)  $M = 8$  channels or (b)  $M = 4$  channels for the blind deconvolution method. The relative error across all channels for both cases is  $\approx 10^{-1}$ .*

#### 2.4.4 Deconvolution of experimentally measured shipping noise recordings

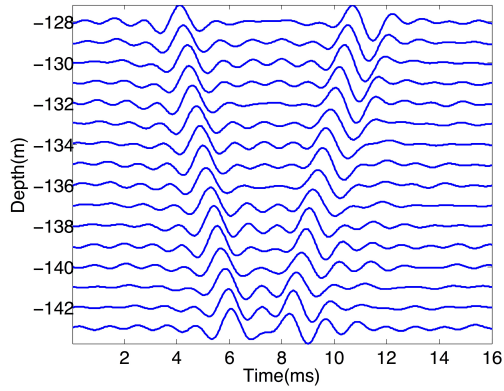
The blind deconvolution method is applied here to shipping noise recorded on a short bottom-mounted vertical line array which was moored in a shallow and nearly range-independent section of the Coronado Bank (water depth  $\approx 150$  m), approximately 20 km offshore of San Diego, CA. Based on prior studies, the environmental parameters for the test site were estimated to be similar to those shown in Fig. 2.7a. The VLA had 16 elements uniformly spaced by 1 m; with the first element approximately 7 m above the seafloor. Other technical features of the hydrophone array deployment and the electronic system have been described previously [46, 47, 16]. The research vessel (R/V) New Horizon was used as a surface source of opportunity to test the blind deconvolution method using the recorded shipping noise data on the VLA. Since no ground truth was available for the actual CIR between the R/V and the VLA, estimated CIRs from the blind deconvolution were compared to the estimated CIRs

independently obtained using a previously described RBD method.

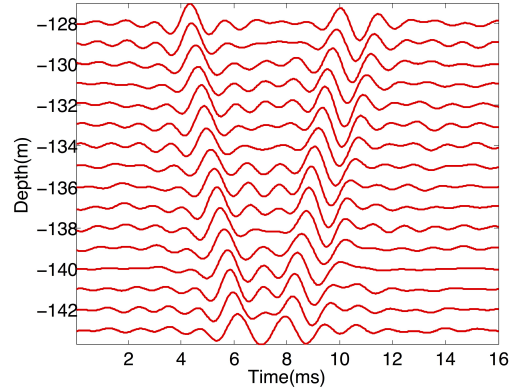
To do so,  $M = 16$  CIRs between the R/V and the VLA were first estimated using RBD for an arbitrarily selected location of the R/V  $\approx 600$  m away from the VLA, referred to hereafter as the “library” location. Based on visual inspection of spectrograms of the recorded shipping noise [47, 16] from the R/V at this distance, its dominant frequency band was found to be  $300 - 800$  Hz and the  $10 - s$  long snapshot of recorded data was filtered in this frequency band. These  $M = 16$  estimated CIRs with RBD (see Fig. 2.9a) were then used to infer a priori arrival-time structure of the CIRs (in the vicinity of this selected library location) as input to the blind deconvolution method. In order to estimate the arrival-time uncertainty for each ray-path of the CIRs, we used historical sound-speed profiles measurements from CTD casts collected in the area and representative of the ocean sound speed fluctuations ( $\approx 3$  m/s) occurring during the time period of the experiments. By running multiple ray simulations using the software BellHop for a source-array separation distance of 2km, through this collection of sound-speed profiles we obtained a maximum uncertainty window of  $\Delta_t = 3$  ms for all considered ray arrivals. An arrival-time window of  $\Delta t = 3$  ms was used here for each ray-like arrival.

The blind deconvolution method was then applied to another set of shipping noise data (referred to as “event” data) recorded from the same R/V when it passed again across the library location a day later to estimate the corresponding CIRs (referred to as recovered CIRs) between the R/V and the VLA (see Fig. 2.9c). As a validation, the CIRs were also estimated independently using the RBD method for the same event data which closely compared to the recovered CIRs from the blind deconvolution method (see Fig. 2.9b and Fig. 2.9c) with an average correlation coefficient across the 16 channels of 0.85. It can also be noted that the CIRs estimated from RBD using the library data (i.e., used only as a priori information for the blind deconvolution method) and the event data (which matched the CIRs obtained from

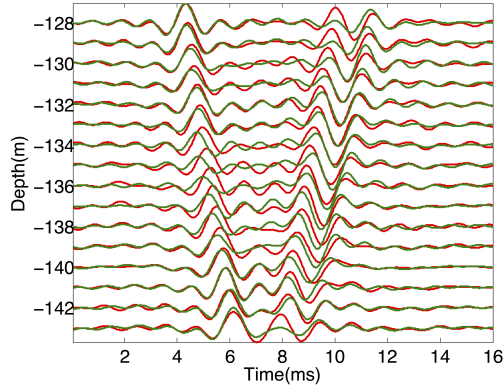
the blind deconvolution method) did significantly differ -as expected- due to variations of the environmental parameters across the selected two days at this shallow water test site: the average correlation coefficient across the 16 channels was only 0.58. Finally, Fig. 2.10 shows that the blind deconvolution method can also be implemented successfully using only a smaller number of receiver elements (respectively 8 and 4 elements), provided that sufficiently accurate a priori information of the arrival-time structure of the CIRs is available (e.g., using simulated data for the selected test site). If such a priori information is available, this may be a significant advantage of the blind deconvolution method over the RBD method which requires an array with sufficiently long aperture to beamform individually the different ray arrivals composing the CIR wavefronts [11].



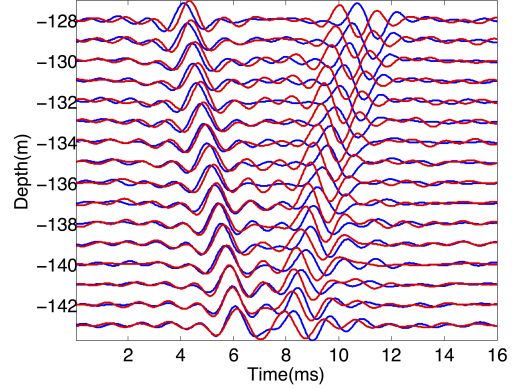
(a) Library CIRs



(b) Event CIRs

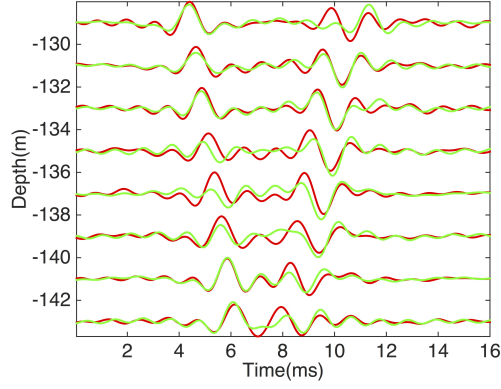


(c) Recovered and Event CIRs

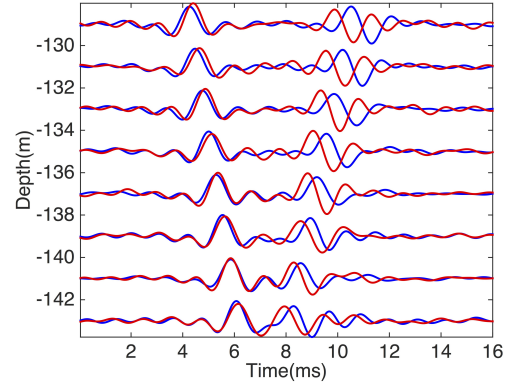


(d) Library and Event CIRs

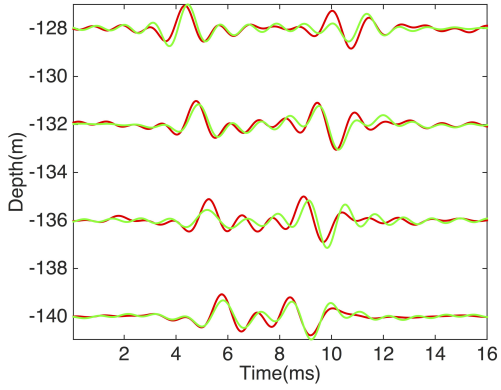
Figure 2.9: *Experimental results using shipping noise. (a) Estimated CIRs using the library data set from the RBD method when the R/V was  $\approx 600$  m from the VLA. (b) Same as (a) but using a different data set (the “event” set) when the R/V was within the same location on a different day. (c) Comparison of the estimated CIRs from either the RBD (red line) or the blind deconvolution method (green line) using the same event data set. (d) Comparison of the estimated CIRs with RBD using either the event data set (red line, same as shown in (b)) or the library data set. (blue line, same as shown in (a))*



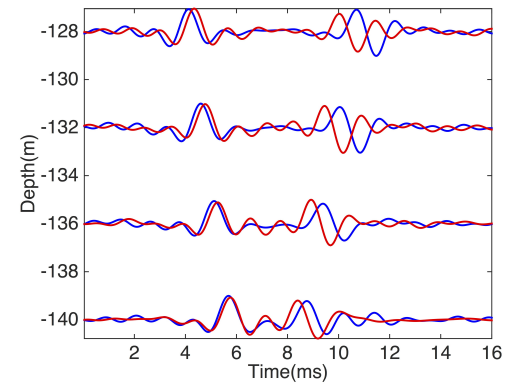
(a) Recovered and Event CIRs



(b) Library and Event CIRs



(c) Recovered and Event CIRs



(d) Library and Event CIRs

Figure 2.10: (a) and (b): Same as Fig. 2.9 (c) and (d) but using only  $M = 8$  channels for the blind deconvolution method. (c) and (d): Same as Fig. 2.9 (c) and (d) but using only  $M = 4$  channels for the blind deconvolution method.

## 2.5 An Extension to Blind Source Separation

Blind source separation (BSS) has wide applications in diverse areas such as audio processing [48], finance [49], geophysics [50], and neural science [51]. In instantaneous mixing scenarios, each measurement consists of a sum of differently weighted source signals, and therefore, these types of systems are memoryless. However, in many real-world applications, such as in acoustics, the measurements are convolutive mixtures because the mixtures are both weighted and delayed. Each source contributes to the

sum with multiple delays and weights corresponding to multiple paths.

Traditionally, in order to solve the BSS problem in specific areas, we need to exploit some statistical assumptions and priors about sources. A tremendous number of BSS algorithms have been reported so far, and one of the most important is Independent Component Analysis [52] (ICA), which exploits the higher-order statistical independence of non-Gaussian signals. More recently, the incorporation of additional source structural priors such as sparsity establishes many connections between BSS and sparse representation, machine learning and compressive sensing [53]. Techniques for separating the sums of structured signals fall into two categories: convex and greedy methods. Convex methods pose BSS as an optimization problem while greedy methods build up signals piece-wise in iterative procedures. Convex optimization also provides a general framework for efficiently solving numerous structural source separation problems that are not discussed in traditional BSS techniques.

We focus on the problem of separating convolutive acoustic mixtures. Many algorithms have been reported for BSS in both time and frequency domains [54]. Using time domain methods for convolutive mixtures, we attempt to estimate an complicated unmixing system, which often generates a large problem with many parameters, so it is very computational costly. However, frequency domain methods transform convolutive mixture into instantaneous mixture problems for each frequency band, so they gain computational efficiency and faster convergence while creating complex-valued computation [55]. But the performance of the frequency methods are fundamentally limited because too few samples may be used in each frequency band, which will cause the independence assumption to fail. Moreover, in each frequency band, a permutation and a scaling ambiguity need to be addressed [56]. Thus, a number of researchers have also developed methods that combine the time-domain criteria with frequency-domain implementations [57, 58] and methods using filter bank [59].

Even though many convolutive algorithms have shown reliable performance when

the mixing process is stationary, few methods work in real-world, time-varying environments. We examine this BSS problem using a different approach via low-rank recovery to treat the convolutive mixtures and develop a general framework for solving blind-source separation and deconvolution. The novelty of our proposed method is that we separate convolutive mixtures through two independent steps. This two-step BSS framework for convoluted mixtures first turns a “memory” mixing system into a “memoryless” system in step one, and then carries out an appropriate demixing techniques in step two.

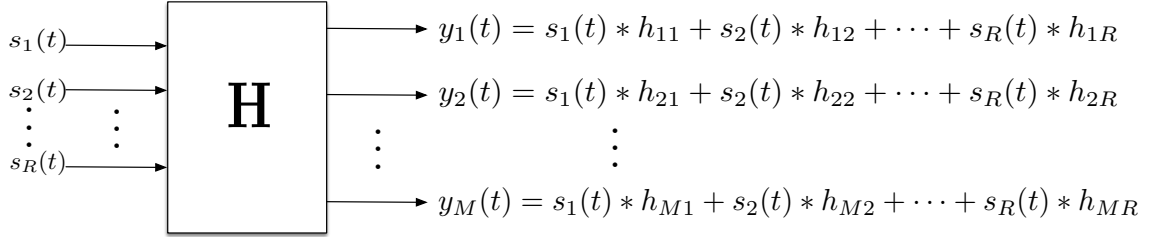


Figure 2.11: *Multiple inputs multiple outputs (MIMO) system of equations.*

In the single source case, we solved the problem by recovering a rank-1 matrix and estimated both the source CIRs simultaneously. The multiple-input and multiple-output (MIMO) system equations are illustrated in Fig. 2.11. We use the same problem formulation for each source across channels, and measurements can be written as:

$$\mathbf{y} = \mathcal{A}(\mathbf{X}_1) + \mathcal{A}(\mathbf{X}_2) + \cdots + \mathcal{A}(\mathbf{X}_R) = \mathcal{A}(\mathbf{X}).$$

where  $\mathcal{A}$  is the same linear operation as the single source case, which takes sums over skew diagonals of submatrices of  $\mathbf{X}_r$ . The matrix  $\mathbf{X}_r$  is the same lifting form of source vector  $\mathbf{s}_r$  and concatenated channel vectors  $\mathbf{h}^{(r)}$ . Here the rank of each matrix  $\mathbf{X}_r$  is 1 and the rank of their sum  $\mathbf{X} = \mathbf{X}_1 + \cdots + \mathbf{X}_R$  is smaller than  $R$ , so our deconvolution method via the low-rank matrix recovery formulation still holds. We

are still searching for a feasible solution  $\mathbf{X}$  has rank no greater than  $R$ .

$$\min_{\mathbf{X}} \text{rank}(\mathbf{X}) \quad \text{subject to} \quad \mathcal{A}(\mathbf{X}) = \mathbf{y}.$$

The same low-rank recovery techniques can be applied and the system can be deconvolved using our heuristic solver. However, in the MIMO case, the multiple sources cannot directly be separated from the deconvolution process and the deconvolution is just the first step of our BSS technique. After the first step, we generate linear combinations of the  $R$  sources. Therefore, for step two, we implement linear mixing source separation techniques that are efficient for the nature of our sources. In our implementation, we use the classical Independent Component Analysis (ICA) to perform the demix in the second step.

We simulated a scenario that four speech signals that have traveled through multipath channels and were observed by 30 channels. This scenario can well approximate the situation that receivers on a VLA measure four ship sources in a known region indicated in Fig. 2.12. We used simulated multipath CIRs for each source, which are plotted in Fig. 2.13.

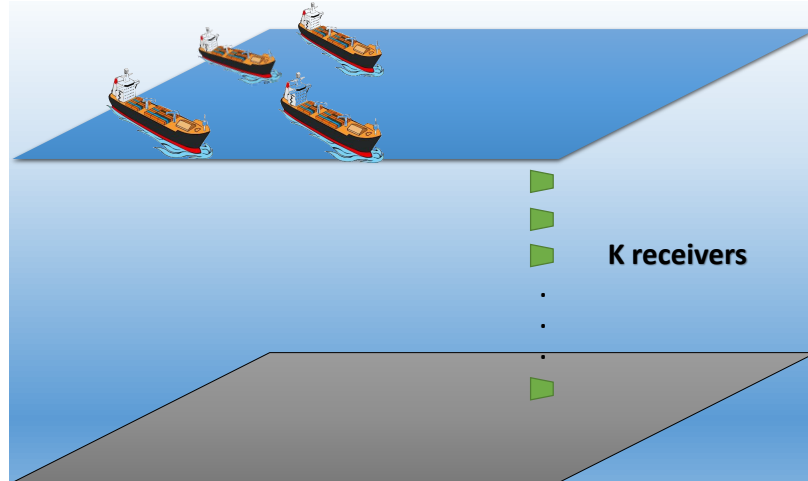


Figure 2.12: *Multiple Inputs Multiple Outputs blind source separation problem scenario in underwater acoustic channels. Four ships signal are measured by the receivers on a VLA.*



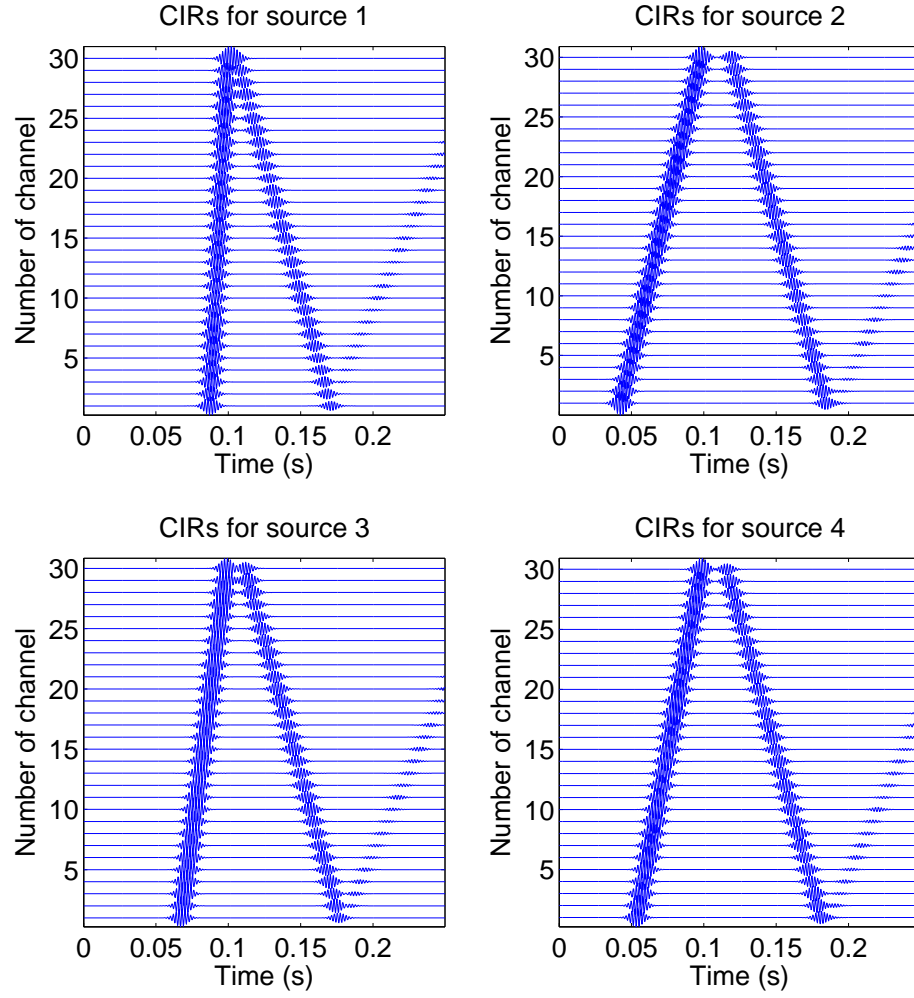


Figure 2.13: *CIRs for four ships. From the measurements of  $M = 30$  channel outputs, we want to estimate the four source signal up to ordering ambiguities.*

Only from convolution measurements and a priori information of CIRs, we are able to estimate the original four speech signals (the order of which is different). The source separation results are shown in Fig. 2.14.

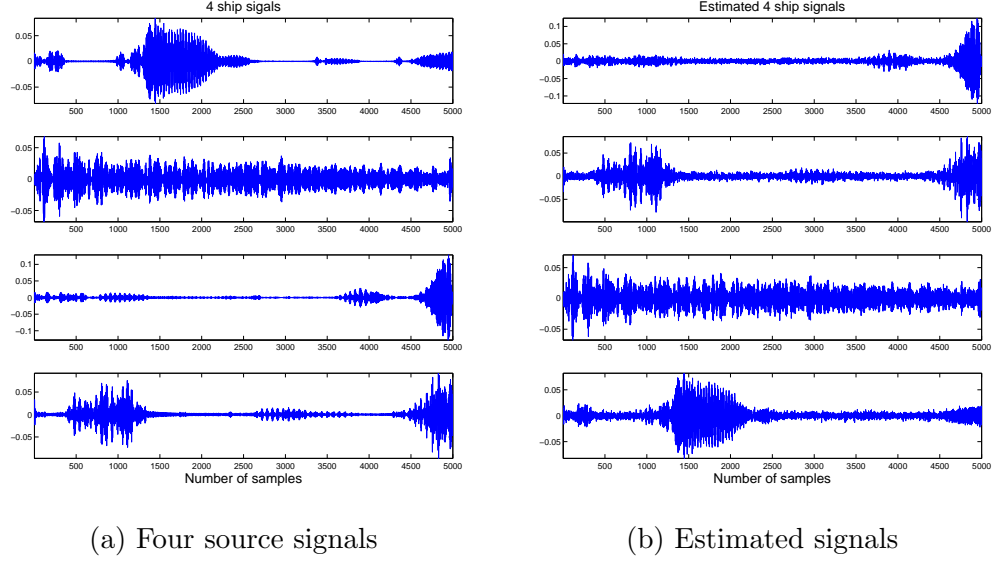


Figure 2.14: *Four input source signals and the separation results from convolutive measurements. The separation results are accurate other than the ordering ambiguity.*

## 2.6 Conclusion

This chapter introduced a method for solving the deconvolution problem using acoustic sources of opportunity and a priori information about the CIR via the low-rank recovery problem formulation. For the shallow-water acoustic channel application, we developed a systematic way to build an efficient and accurate linear model incorporating a priori information about the expected CIRs' arrival-time structure so that the low-rank recovery method can be implemented for the proposed blind deconvolution method. Stylized numerical simulations demonstrated that the proposed method perfectly deconvolved both the noise source signal and CIRs simultaneously. The proposed method was also shown to be robust in the presence of additive measurement noises and model errors in the CIR parameterization. Furthermore the applicability of the proposed blind deconvolution method for estimated CIRs in shallow water using shipping noise and short bottom-mounted VLAs was demonstrated both numerically and experimentally. This method is likely to be applicable to other environments supporting waveguide-like propagation (e.g., seismic or structural waveguides). The

proposed blind deconvolution method then naturally extends to the multiple input multiple output (MIMO) deconvolution problem (i.e., the case of multiple sources of opportunities) and we showed successfully blind source separation results.

## CHAPTER 3

# MULTICHANNEL DECONVOLUTION USING BILINEAR CHANNEL MODELS

### 3.1 Introduction

In ocean waveguide environments, the typical ray-like arrival-time structure of the CIR between a surface source and the element of a vertical line array (VLA) provides us a priori information about the CIRs, which turns the multichannel blind deconvolution problem feasible (see Fig. 1.1). In many situations, a known, active source signal is not available for use because of environmental or physical constraints (e.g., nature reserve habitat), while sources of opportunity present themselves. Therefore, using sources of opportunity in acoustic imaging applications is increasingly active. This chapter presents further investigation that exploit the structure of CIRs jointly and algorithms for solving multichannel blind deconvolution with a more confined model.

In the application of acoustic imaging using elements of a VLA, the blind deconvolution problem under the multiple-channel framework provides diversification of observations, and various studies have addressed this multichannel blind deconvolution problem. In Chapter 2, we have previously developed a fast multichannel myopic deconvolution method via low-rank recovery technique [60]. The deconvolution method via low-rank recovery does not take account of the linking among arrival-times of the CIRs across all channels, which is a further constraint of the channel model as a result of the VLA sensing configuration. This chapter utilizes the linking among arrival-times of the CIRs across all channels by introducing a bi-

linear channel model for CIRs, which further reduces the dimension of the channel parametric model compared to the linear model. We will demonstrate later in this chapter that using the bilinear channel model, the deconvolution method is more robust to measurement noise and can estimate the CIRs more accurately because the additional constraint imposed on the channel model. We also can incorporate larger uncertainty arrival-times into our model than the linear model we introduced in the previous chapter.

We show that this problem is well-posed if the channels follow a bilinear model where the ensemble of CIRs is modeled as lying in a low-dimensional subspace but with each channel modulated by an independent gain. Under this model, we show how the CIRs estimates can be found by minimizing a quadratic function over a non-convex set.

Algorithms for solving non-convex quadratic and bilinear problems have recently been introduced for solving problems closely related to blind deconvolution. A non-convex optimization over matrix manifolds provides a guaranteed solution for matrix completion [61]. Alternating minimization is another non-convex optimization algorithm for matrix completion that provides a provable performance guarantee [62, 63, 64]. Phase retrieval is cast as a non-convex optimization because of the nonlinearity in generating the observation. Wirtinger flow algorithms [65, 66, 67, 68] and alternating minimization [69, 70] are non-convex optimization algorithms for the phase retrieval problem.

While algorithms based on heuristics for particular applications have existed for decades, it is not until recently that a rich mathematical theory has developed around this problem. The fundamental identifiability of solutions to this problem has been studied from an information theoretic perspective [71, 72, 73, 74, 75, 76, 77]. Practical algorithms with provable performance guarantees that make the problem well-posed by imposing structural constraints on the signals have arisen based on ideas from

compressive sensing and low-rank matrix recovery. These include methods based on convex programming [26, 78, 79], alternating minimization [80], and gradient descent [81].

We propose two methods for solving this non-convex program, and provide performance guarantees for each under a generic bilinear channel model. The first is a method of alternating eigenvectors that breaks the program down into a series of eigenvalue problems. The second is a truncated power iteration, which can roughly be interpreted as a method for finding the largest eigenvector of a symmetric matrix with the additional constraint that it adheres to our bilinear model. As with most non-convex optimization algorithms, the performance of both of these algorithms is highly dependent on having a good starting point. We show how such a starting point can be constructed from the channel measurements.

We also implement the truncated power iteration method on underwater acoustic channels and show effectiveness in simulations based on Santa Barbara Channel at-sea experiments data. Our method is also verified by the Noise09 data that we discussed in the previous chapter. Our method is shown robust to both the measurement noise and specific modeling errors.

The remainder of this chapter is organized as follows. Section 3.2 presents the establishment of the bilinear channel model motivated by the VLA sensing scenario. Section 3.3 formulate of the blind deconvolution problem using cross convolution method under the bilinear channel representation. Section 3.4 presents two iterative algorithms for multichannel blind deconvolution under the bilinear channel model, which are obtained by modifying the classical cross-convolution method. Our main results on non-asymptotic stable recovery are presented in Section 3.5. Section 3.6 then presents numerical simulation results on realistic acoustic channels and simulations that support the theories developed in this chapter. Finally, Section 3.7 summarizes the findings of this chapter.

### 3.2 Bilinear Channel Models

In an ocean acoustic array sensing scenario, receivers of the vertical line array with equal distance spacing listen to the same source near the ocean surface in a distance. The array receives sound that propagates in separate paths, which have been well modeled using the image method [34]. Distances through which sound travels along the same path to each receiver, such as the direct path, are dependent on the source-receiver configuration. Meanwhile, sound traveling along the same path will experience almost the same media (speed of sound and loss) and environmental parameters. Any environmental change or disturbance of the media will result in the same fluctuation of arrival-times of sound pulses across channels. Therefore, arrival-times of the same path for each receiver are linked, and their relation is determined by the source-receiver configuration and environmental parameters. In this section, we develop a bilinear channel model that is motivated by exploring the relation of arrival-times across channels.

A typical example of CIRs with only the direct path for all receivers along a VLA is demonstrated as in Fig. 3.1d. The CIRs can be written as a function in terms of pulse arrival-times and pulse amplitudes as parameters:

$$h_m(t) = a_m \cdot p(t - t_m), \quad (3.1)$$

where  $t_m$  (illustrated in Fig. 3.1c) and  $a_m$  (illustrated in Fig. 3.1b) are the arrival-time and amplitude of the direct path pulse for channel  $m$  respectively, and the function  $p(t)$  (illustrated in Fig. 3.1a) is the pulse profile which corresponds to the filter choice of the receivers. Assuming that the arrival-times across channels can be linked by a function  $t_m = f(m)$ , where  $m$  is the channel number and the function  $f$  explains the relation of the arrival-times across channels, we want to build a parametric model for the CIRs using this relation. When the distance between the source and receivers

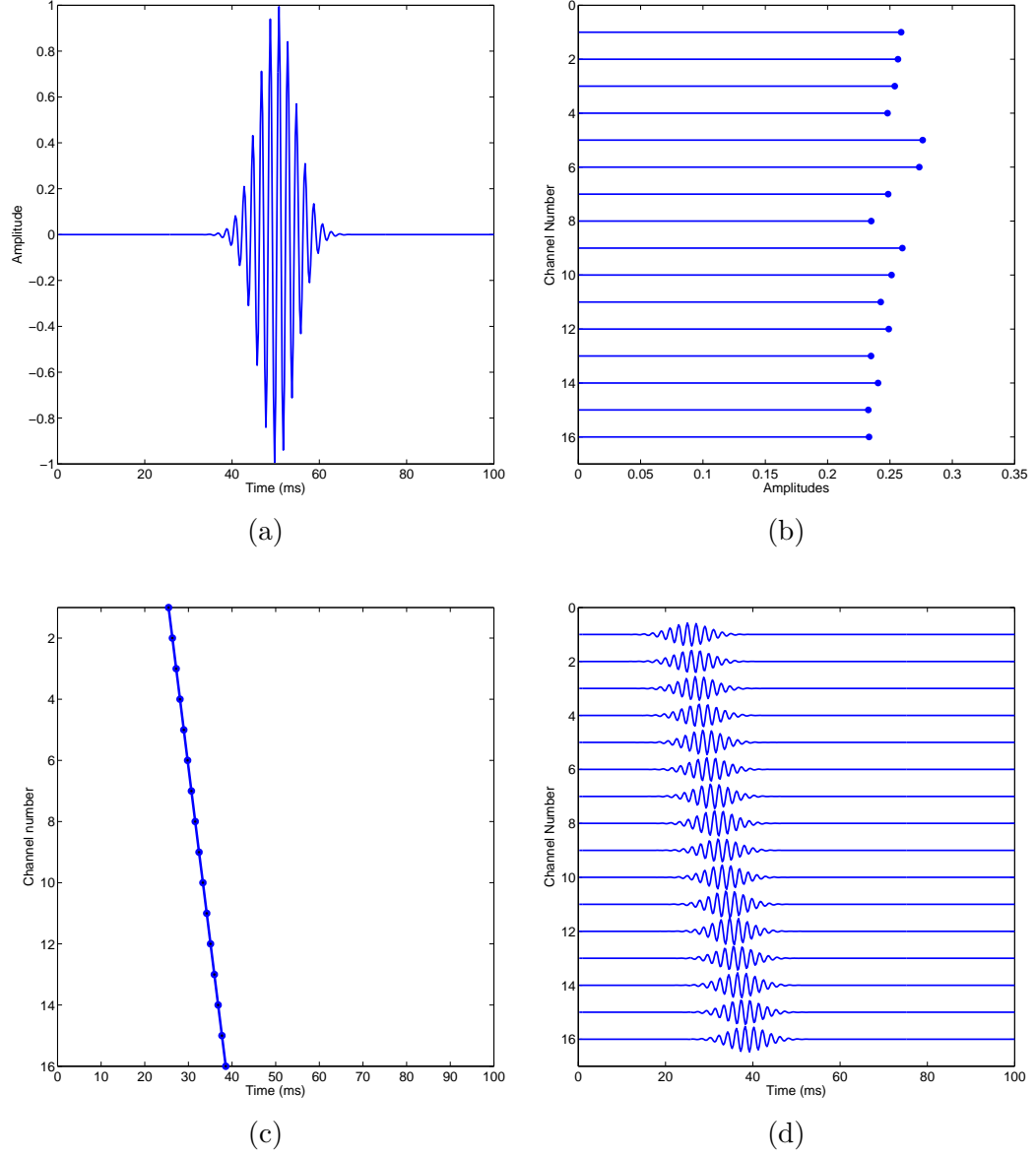


Figure 3.1: (a) A known pulse profile  $p(t)$ . (b) Amplitudes for each CIRs. (c) Arrival-times for pulses across channels. (d) Pulses across channels for a single path case.



are far compared to the length of the array, we can assume that arrival-time of each receiver falls along a line in terms of the depth of each receiver. When receivers are equally vertically spaced, the depths of receivers can be indicated by the channel number  $m$ . The linear relation of arrival-times and receiver depths can be illustrated by

$$t_m = t_1 + (m - 1)k, \quad (3.2)$$

where  $t_1$  is the arrival-time for the first channel, and  $k$  is the slope of the line. The slope  $k$  will depend on fixed parameters such as VLA geometry, environmental parameters such as source and receiver range, local sound speed and so on. In our example of arrival-times shown in Fig. 3.1c, the linear relation for all arrival-times is plotted.

Incorporating the pulse arrival-times structure into a parametric channel model and matching a low-dimensional subspace for CIRs which consists of such pulses for the same path require us to model channels jointly. However, each CIR still has an independent amplitude modulating the pulse, so we need to separate the amplitude variables from the arrival-time variables in the model. The model now is a bilinear model, where one variable vector defines the amplitudes and one variable vector defines the linked arrival-times of all pulse on the same path. This bilinear model differs from the linear channel model studied in previous research [60], and further reduces the dimension of the subspace for all CIRs and constrains the model compared to the linear model. However, new deconvolution algorithms are needed to recover the CIRs under this channel model, which will be addressed later in this chapter.

The Principal Component Analysis technique is applied to solve the subspace matching problem for pulses whose arrival-times are linked by a known relation. We discretize the CIR  $h_m(t)$  to a vector  $\mathbf{h}_m \in \mathbb{R}^N$  and the pulse  $p_m(t)$  to  $\mathbf{p}_m \in \mathbb{R}^N$  (note that each CIR  $\mathbf{h}_m$  has an independent amplitude  $a_m$  of the pulse  $\mathbf{p}_m$ ). Because we are treating the channels jointly, the signal to which we want to match a subspace is

the concatenated pulse basis vector

$$\underline{\mathbf{p}} = [\mathbf{p}_1^\top, \dots, \mathbf{p}_M^\top]^\top, \quad \text{where } \underline{\mathbf{p}} \in \mathbb{R}^{MK}. \quad (3.3)$$

Suppose we obtain a collection of  $\underline{\mathbf{p}}^i$  in a set  $\mathcal{R}$  because the source range is varying and the environment of the source-receiver configuration is changing over time. As we vary  $\underline{\mathbf{p}}^i$  over the set  $\mathcal{R}$ , the responses  $\underline{\mathbf{p}}^i$  trace out a portion of a manifold in  $\mathbb{C}^{MK}$ . We can (approximately) embed this manifold in a linear subspace of dimension  $D$  by looking at the  $D$  principal eigenvectors of the matrix

$$\mathbf{H}_{\mathcal{R}} = \sum_i \underline{\mathbf{p}}^i \underline{\mathbf{p}}^{i*}.$$

The dimension  $D$  that provides an accurate embedding will depend on the size of  $\mathcal{R}$  and smoothness properties of the varying process in  $\underline{\mathbf{p}}^i$ .

This technique of embedding a parametric model into a linear space has been explored for source localization and channel estimation in underwater acoustics in [82, 60], and some analysis in the context of compressed sensing is provided in [82]. However, in order to treat CIRs jointly, the amplitudes of the CIRs vary between receivers in the array, and this variation compromises the subspace embedding described above. The bilinear model discussed in this chapter explicitly accounts for these channel-to-channel variations.

Let's then discuss in details how this bilinear model can be generated in the application of ocean acoustic array sensing. Fixing the source-receiver configuration provides the arrival-time relationship function  $t_m = f(m)$  in a stable environment. Meantime, the function  $f$  varies because of environmental variations or the source is moving. Each possible environment variation or a different location of the source (indexed by  $i$ ) leads to a different function  $t_m^i = f^i(m)$ . From historical data of the environment, the environmental variation range can be estimated, and the range of

source is known, so we are able to generate or observe a collection of  $\mathbf{t}^i = [t_1, \dots, t_M]^i$  within the range limits.

As an example, when the distance between the source and receivers are far compared to the length of the array and the arrival-times for the same path fall along a line, the range of the environmental variation can be indicated by one arrival time  $t_i$  and slope  $k$ . The range of all possible arrival-times which satisfy the linear relation in a certain environment can be plot as in Fig. 3.2, where the black region indicates the collection of all possible arrival-times.

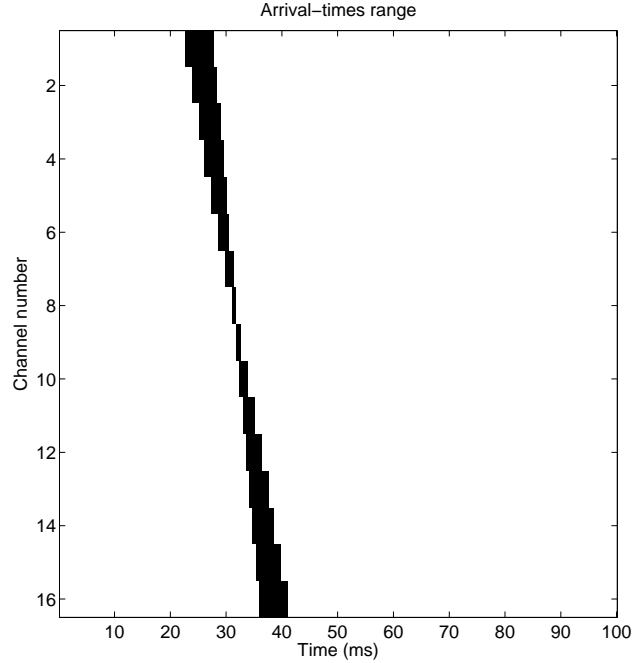


Figure 3.2: *Arrival-times range across channels. Black shaded region indicates all possible arrival-times.*

Then, from each possible  $\mathbf{t}^i$ , a collection of  $\underline{\mathbf{p}}^i$  are generated. Even though the number of  $\underline{\mathbf{p}}^i$  are large, they lie on a manifold which can be approximated by a linear subspace using PCA, which is closely related to the area of manifold embeddings. We denote the basis matrix of the subspace to be  $\Phi \in \mathbb{R}^{MK \times D}$ , which is constructed by

PCA, and for a certain  $\underline{\mathbf{p}}$ , we can write it as

$$\underline{\mathbf{p}} = \Phi \mathbf{u}, \quad (3.4)$$

where  $\mathbf{u} \in \mathbb{R}^D$  is the coefficient vector which fully describes the corresponding realization of arrival-times  $\mathbf{t}$ .

In particular, we can estimate the parameter  $t_1$  and  $k$  up to a range in the linear relation of all arrival-times as in Eq. (3.2). Within the range, we alter the value of  $t_1$  and  $k$  in fine increments to generate a collection of  $\underline{\mathbf{p}}^i$  which overpopulate all possible pulses in this scenario. Stacking all  $\underline{\mathbf{p}}^i$  as column vectors generate an over-complete matrix which spans the subspace. We can visualize such collection of CIRs as in Fig. 3.3a

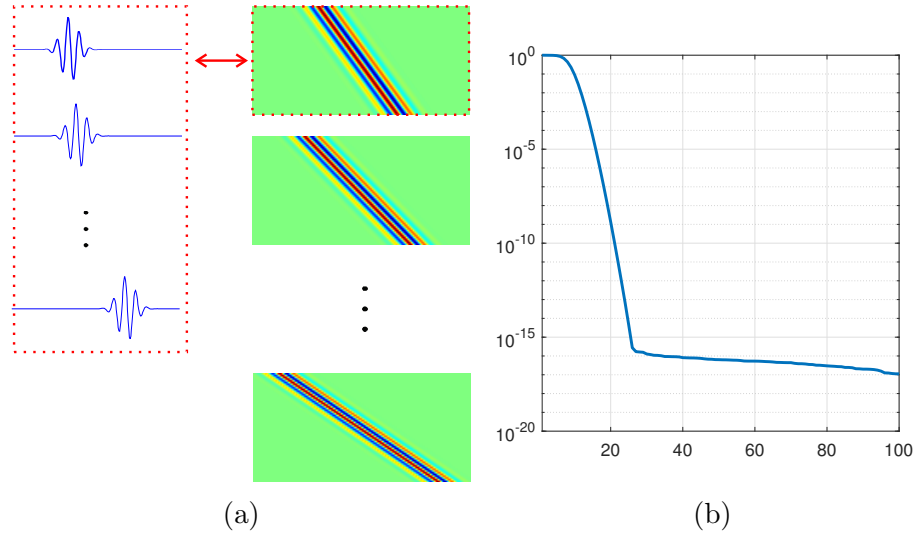


Figure 3.3: *Illustration of the collection of CIRs and the eigenvalues of the space spanned by all CIRs. (a) Examples of  $\underline{\mathbf{p}}^i$  rearranged as M-by-N matrices. (b) Sorted eigenvalues of  $\mathbf{H}_{\mathcal{R}}$  in a logarithmic scale.*

Because each realization of  $\underline{\mathbf{p}}^i$  is highly correlated, performing a PCA on the over-complete matrix generates a low-dimensional linear subspace bases matrix  $\Phi$ . A rapid decaying of the eigenvalues in a typical PCA operation on the collection of  $\{\underline{\mathbf{p}}^i\}$  is shown in Fig. 3.3b. Here  $\Phi$  corresponds to the definition in Eq. (3.4) and

can represent all possible pulses whose arrival-times are on the 'lines' in Fig. 3.2. Vectors of the subspace basis are interpreted as in Fig. 3.4 (the first 6 basis vectors are plotted).

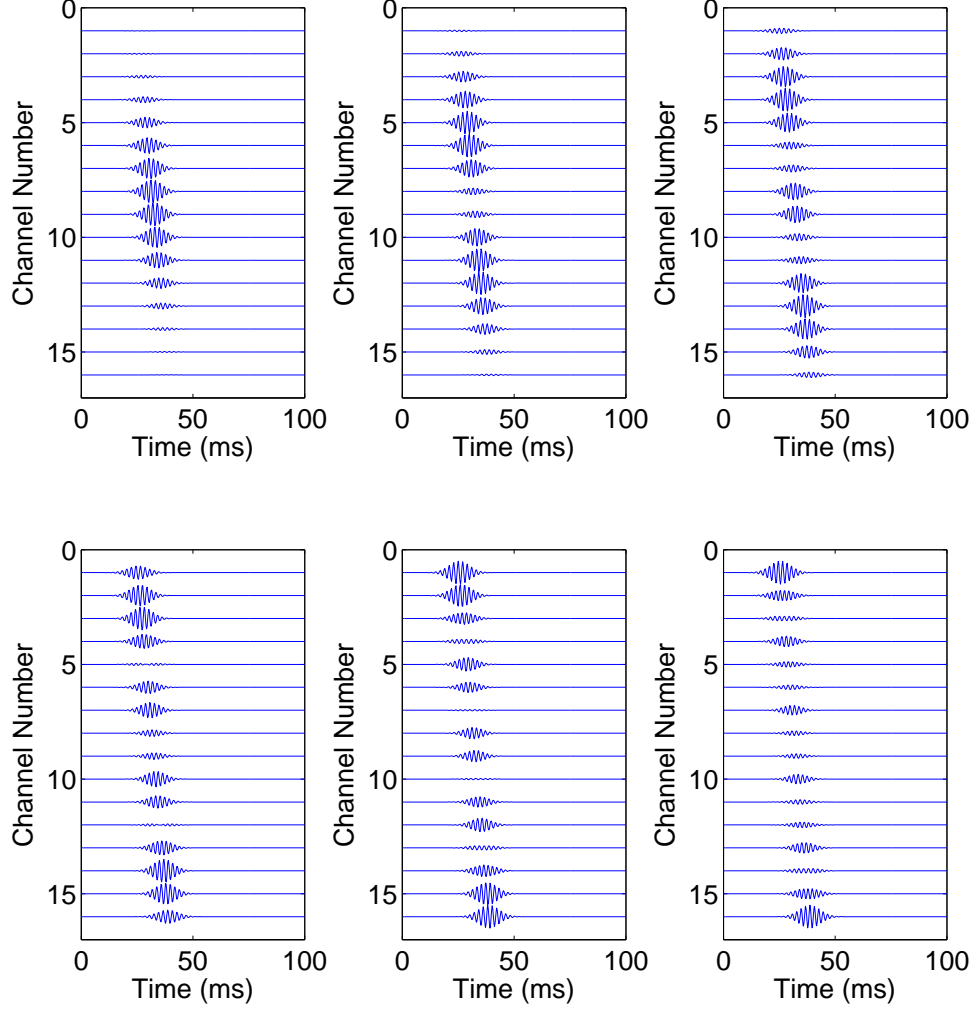


Figure 3.4: *First 6 basis of a linear subspace that are generated from a parametric embedding of all pulses across channels.*

Let  $\underline{\mathbf{h}} \in \mathbb{R}^{MK}$  denote the concatenation of the CIR coefficients for all channels, i.e.,

$$\underline{\mathbf{h}} = [\mathbf{h}_1^\top, \dots, \mathbf{h}_M^\top]^\top.$$

With a linear subspace for the pulse vectors  $\underline{\mathbf{p}}$  in place,  $\underline{\mathbf{h}}$  can be then modeled by a bilinear channel model. The bilinear channel model approximate all CIR vectors

jointly with two independent vectors as variables, which correspond to amplitudes and the structure of arrival-times (i.e. we can interpret it as a vector to define the slope of arrival-times when they are linearly linked). We can explicitly write out the bilinear channel model for each CIR as

$$\begin{bmatrix} \mathbf{h}_1 \\ \mathbf{h}_2 \\ \vdots \\ \mathbf{h}_M \end{bmatrix} = \begin{bmatrix} a_1 \mathbf{\Phi}_1 \\ a_2 \mathbf{\Phi}_2 \\ \vdots \\ a_M \mathbf{\Phi}_M \end{bmatrix} \mathbf{u}, \quad (3.5)$$

where  $(\mathbf{\Phi}_m)_{m=1}^M \in \mathbb{R}^{K \times D}$  are the  $m$ th row-blocks of the subspace matrix  $\mathbf{\Phi}$  defined in Eq. (3.4),  $\mathbf{u} \in \mathbb{R}^D$  is the coefficient vector that determines the structure arrival-times on one particular path across all channels, and each element of the vector  $\mathbf{a} = [a_1, \dots, a_M]^\top \in \mathbb{R}^M$  with  $a_m > 0$  is the amplitude of channel  $m$ .

Equation (3.5) can then be equivalently rewritten as a more concise form using Kronecker product as below

$$\underline{\mathbf{h}} = \mathbf{\Phi}(\mathbf{a} \otimes \mathbf{u}), \quad (3.6)$$

where

$$\mathbf{\Phi} := \begin{bmatrix} \mathbf{\Phi}_1 & \mathbf{0} & \dots & \mathbf{0} \\ \mathbf{0} & \mathbf{\Phi}_2 & \dots & \mathbf{0} \\ \vdots & \vdots & \ddots & \vdots \\ \mathbf{0} & \mathbf{0} & \dots & \mathbf{\Phi}_M \end{bmatrix} \quad \text{and} \quad \mathbf{a} \otimes \mathbf{u} = \begin{bmatrix} a_1 \mathbf{u} \\ a_2 \mathbf{u} \\ \vdots \\ a_M \mathbf{u} \end{bmatrix}.$$

Note here that we change the definition of  $\mathbf{\Phi}$ , which is different from Eq. (3.4). From here to the end of the chapter, we use the definition of  $\mathbf{\Phi}$  as in Eq. (3.6).

The formulation above only represents a single path case. For more general multi-path channels (number of paths is  $N$ ), the bilinear channel model still holds, and the

concatenation of CIR vectors  $\mathbf{h}$  can be written as

$$\underline{\mathbf{h}} = \tilde{\Phi}[(\mathbf{a}_1 \otimes \mathbf{u}_1)^\top, \dots, (\mathbf{a}_N \otimes \mathbf{u}_N)^\top]^\top, \quad (3.7)$$

where

$$\tilde{\Phi} := \begin{bmatrix} \Phi_{11} & \mathbf{0} & \dots & \mathbf{0} & \dots & \Phi_{N1} & \mathbf{0} & \dots & \mathbf{0} \\ \mathbf{0} & \Phi_{12} & \dots & \mathbf{0} & \dots & \mathbf{0} & \Phi_{22} & \dots & \mathbf{0} \\ \vdots & \vdots & \ddots & \vdots & \ddots & \vdots & \vdots & \ddots & \vdots \\ \mathbf{0} & \mathbf{0} & \dots & \Phi_{1M} & \dots & \mathbf{0} & \mathbf{0} & \dots & \Phi_{NM} \end{bmatrix}. \quad (3.8)$$

A general bilinear channel model that exploits the pulse arrival-times relation across channels are introduced based on the application of underwater acoustic channels. This bilinear channel model can also be found in many multiple-channel systems where a linear subspace embedding exists to approximate certain structure of CIRs (i.e. parametric estimation) jointly while another parameter of the CIR has to be modified independently (i.e. gains of each channel) for each channel. We will then investigate the formulation and algorithms for solving multichannel blind deconvolution problem when such bilinear channel models can be applied.

### 3.3 Spectral Methods for Multichannel Deconvolution

In this section, we revisit a classical method of treating the multichannel blind deconvolution problem and adapt this method with bilinear channel models. The classical method recast the problem as an eigenvalue problem: we create a correlation matrix using the measured data  $\{\mathbf{y}_m\}$ , and estimate the channels from the eigenvector corresponding to the smallest eigenvalue (the smallest eigenvector) of this matrix. These methods were pioneered in the mid-1990s in [1, 3, 35], and we briefly review the essential ideas in this section. The methods we present in the next section operate on

the same basic principles, but explicitly enforce structural constraints on the solution based on the bilinear channel model.

The cross-convolution method for multichannel blind deconvolution [1] follows directly from the commutivity of the convolution operator. Given the noisy measurements

$$\mathbf{y}_m = \mathbf{h}_m \circledast \mathbf{x} + \mathbf{w}_m, \quad m = 1, \dots, M, \quad (3.9)$$

If there is no noise in the observations, then we can have the following equation

$$\mathbf{y}_{m_1} \circledast \mathbf{h}_{m_2} - \mathbf{y}_{m_2} \circledast \mathbf{h}_{m_1} = \mathbf{0}, \quad \text{for all } m_1, m_2 = 1, \dots, M.$$

Using  $\mathbf{T}_{\mathbf{y}_m}$  as the matrix whose action is convolution with  $\mathbf{y}_m$  with a signal of length  $K$ , we see that the channel responses  $\mathbf{h}_{m_1}$  and  $\mathbf{h}_{m_2}$  must obey the linear constraints  $\mathbf{T}_{\mathbf{y}_{m_1}} \mathbf{h}_{m_2} - \mathbf{T}_{\mathbf{y}_{m_2}} \mathbf{h}_{m_1} = \mathbf{0}$ . We can collect all pairs of these linear constraints into a large system, and the vector  $\underline{\mathbf{h}} \in \mathbb{R}^{MK}$  defined in (3.2), which corresponds to the concatenation of all CIRs vectors, is determined by

$$\mathbf{Y} \underline{\mathbf{h}} = \mathbf{0}_{M(M-1)L/2 \times 1}, \quad (3.10)$$

where  $\mathbf{Y} \in \mathbb{R}^{M(M-1)L/2 \times MK}$  is defined by

$$\mathbf{Y} = \begin{bmatrix} \mathbf{Y}^{(1)} \\ \mathbf{Y}^{(2)} \\ \vdots \\ \mathbf{Y}^{(M-1)} \end{bmatrix}, \quad \mathbf{Y}^{(i)} = \begin{bmatrix} \mathbf{0}_{L,K} & \dots & \mathbf{0}_{L,K} & \mathbf{T}_{\mathbf{y}_{i+1}} & -\mathbf{T}_{\mathbf{y}_i} \\ \vdots & & \vdots & \vdots & \ddots \\ \mathbf{0}_{L,K} & \dots & \mathbf{0}_{L,K} & \underbrace{\mathbf{T}_{\mathbf{y}_M}}_{(M-i+1) \text{ blocks}} & \underbrace{-\mathbf{T}_{\mathbf{y}_i}}_{(M-i+1) \text{ blocks}} \end{bmatrix}. \quad (3.11)$$

We can further write out explicitly what matrix  $\mathbf{Y}$  looks like:



$$\mathbf{Y} = \begin{bmatrix} \mathbf{T}_{y_2} & -\mathbf{T}_{y_1} & \mathbf{0} & \mathbf{0} & \cdots & \mathbf{0} & \mathbf{0} \\ \mathbf{T}_{y_3} & \mathbf{0} & -\mathbf{T}_{y_1} & \mathbf{0} & \cdots & \mathbf{0} & \mathbf{0} \\ \mathbf{T}_{y_4} & \mathbf{0} & \mathbf{0} & -\mathbf{T}_{y_1} & \cdots & \mathbf{0} & \mathbf{0} \\ \vdots & \vdots & \vdots & \vdots & \ddots & \vdots & \vdots \\ \mathbf{T}_{y_M} & \mathbf{0} & \mathbf{0} & \mathbf{0} & \cdots & \mathbf{0} & -\mathbf{T}_{y_1} \\ \mathbf{0} & \mathbf{T}_{y_3} & -\mathbf{T}_{y_2} & \mathbf{0} & \cdots & \mathbf{0} & \mathbf{0} \\ \mathbf{0} & \mathbf{T}_{y_4} & \mathbf{0} & -\mathbf{T}_{y_2} & \cdots & \mathbf{0} & \mathbf{0} \\ \vdots & \vdots & \vdots & \vdots & \ddots & \vdots & \vdots \\ \mathbf{0} & \mathbf{T}_{y_M} & \mathbf{0} & \mathbf{0} & \cdots & \mathbf{0} & -\mathbf{T}_{y_2} \\ \vdots & \vdots & \vdots & \vdots & \ddots & \vdots & \vdots \\ \mathbf{0} & \mathbf{0} & \mathbf{0} & \mathbf{0} & \cdots & \mathbf{T}_{y_M} & -\mathbf{T}_{y_{M-1}} \end{bmatrix}.$$

In other words,  $\underline{\mathbf{h}}$  is determined as the null vector of  $\mathbf{Y}$ . It was shown that  $\underline{\mathbf{h}}$  is uniquely determined up to scaling ambiguity by (3.10) (i.e.  $\mathbf{Y}$  has a null space that is exactly 1 dimensional) under a mild algebraic condition that the polynomials generated by  $\{\mathbf{h}_m\}_{m=1}^M$  have no common zero. Furthermore, under a certain statistical noise model, this estimate is also consistent because the problem reduces to the noise-free case as the measurement length  $L$  goes to infinity. In the presence of noise,  $\underline{\mathbf{h}}$  is estimated as the minimum eigenvector of  $\mathbf{Y}^*\mathbf{Y}$

$$\hat{\underline{\mathbf{h}}} = \arg \min_{\|\mathbf{g}\|_2=1} \mathbf{g}^*\mathbf{Y}^*\mathbf{Y}\mathbf{g}. \quad (3.12)$$

Note that  $\mathbf{Y}^*\mathbf{Y}$  is computed cross-correlating the outputs. Therefore,  $\mathbf{Y}^*\mathbf{Y}$  is computed at a low computational cost using the fast Fourier transform. Furthermore, the size of  $\mathbf{Y}^*\mathbf{Y}$ , which is  $MK \times MK$ , does not grow with as the length of observation increases. When there is white additive noise, this cross-correlation matrix will in expectation be the noise-free version plus a scaled identity. These means that as the sample size gets large, the noisy and noise-free measurements cross-correlations will

have the same eigenvectors, and the estimate (3.12) is consistent.

A similar technique can be used if we have a linear model for the channel responses as we discussed in Eq. (2.13) of chapter 2. We can estimate the expansion coefficients  $\mathbf{v}$  by solving

$$\underset{\mathbf{v}}{\text{minimize}} \quad \mathbf{v}^* \mathbf{C}^* (\mathbf{Y}^* \mathbf{Y} - \varrho \mathbf{I}) \mathbf{C} \mathbf{v} \quad \text{subject to} \quad \|\mathbf{v}\|_2 = 1, \quad (3.13)$$

where  $\varrho$  is a scalar that depends on the variance of the additive noise (this correction is made so that eigenstructure more closely matches that of  $\mathbf{C}^* \mathbf{Y}^* \mathbf{Y} \mathbf{C}$  for noise-free  $\mathbf{Y}$ ). The classical method in Eq.(3.12) is sensitive to noise when working with finite number of measurements samples. In [83], it was shown that a linear model can significantly improve the stability of the estimate of  $\underline{\mathbf{h}}$  in the presence of noise, and a rigorous non-asymptotic analysis of the estimation error for generic bases  $\mathbf{C}$  is presented.

When the CIRs have a bilinear channel model, we formulate our optimization problem to solve the multichannel deconvolution by adding an additional constraint to optimization program which is similar to (3.12) and (3.13) above. The additional constraint require  $\underline{\mathbf{h}}$  can be represented by a bilinear model as in (3.6).

We create the matrix

$$\mathbf{A} = \mathbf{\Phi}^* (\mathbf{Y}^* \mathbf{Y} - \hat{\sigma}_w^2 (M-1) L \mathbf{I}_{MK}) \mathbf{\Phi},$$

where  $\hat{\sigma}_w^2$  is an estimate of the noise variance  $\sigma_w^2$ , and  $\mathbf{Y}$  is formed as in (3.11) in the previous section. We then solve a program that is similar to the eigenvalue problems above, but with a Kronecker product constraint on the expansion coefficients:

$$\underset{\mathbf{v}, \mathbf{a}, \mathbf{u}}{\text{minimize}} \quad \mathbf{v}^* \mathbf{A} \mathbf{v} \quad \text{subject to} \quad \|\mathbf{v}\|_2 = 1, \quad \mathbf{v} = \mathbf{a} \otimes \mathbf{u}. \quad (3.14)$$

For multipath channels, CIRs are the sum of multiple path pulses with a certain arrival-time structure. We use  $\tilde{\mathbf{A}}$  to denote the multipath case, which can be written as

$$\tilde{\mathbf{A}} = \tilde{\mathbf{\Phi}}^* (\mathbf{Y}^* \mathbf{Y} - \hat{\sigma}_w^2 (M-1) L \mathbf{I}_{MK}) \tilde{\mathbf{\Phi}},$$

where  $\tilde{\mathbf{\Phi}}$  is define in Eq. (3.8). So the optimization problem can be rewritten as

$$\underset{\tilde{\mathbf{v}}}{\text{minimize}} \quad \tilde{\mathbf{v}}^* \tilde{\mathbf{A}} \tilde{\mathbf{v}} \quad \text{subject to} \quad \|\mathbf{v}\|_2 = 1, \quad \mathbf{v} = [(\mathbf{a}_1 \otimes \mathbf{u}_1)^\top, \dots, (\mathbf{a}_N \otimes \mathbf{u}_N)^\top]^\top. \quad (3.15)$$

A more straightforward statement of the optimization problem for multipath channels can be written as

$$\begin{aligned} \min_{\mathbf{u}, \mathbf{a}} \quad & \|\mathbf{Y} \tilde{\mathbf{\Phi}} [(\mathbf{a}_1 \otimes \mathbf{u}_1)^\top, \dots, (\mathbf{a}_N \otimes \mathbf{u}_N)^\top]^\top\|_2^2 \\ \text{s.t.} \quad & \|\tilde{\mathbf{\Phi}} [(\mathbf{a}_1 \otimes \mathbf{u}_1)^\top, \dots, (\mathbf{a}_N \otimes \mathbf{u}_N)^\top]^\top\|_2 = 1 \\ & a_m \geq 0, \quad \forall m = 1, \dots, M, \end{aligned} \quad (3.16)$$

which is equivalent to the problem defined in Eq. (3.15).

### 3.4 Non-convex Optimization Algorithms

The norm and bilinear constraints on our formulations (as in Eq. (3.14) and Eq. (3.16)) of both single path and multipath (linear sum of multiple bilinear model) make this a non-convex optimization program, and unlike the spectral methods for linear channel models, no (known) computationally efficient algorithm to compute its solution is available to our knowledge. The problem can no longer be solved by finding the least dominant eigenvector of a given matrix. Note that  $\mathbf{v}$  has a rank-1 structure by construction and this structure induces a logical alternating minimization approach.

We propose and analyze two non-convex optimization algorithms for solving (3.14).

The first is an alternating eigenvalue method, which iterates between minimizing for  $\mathbf{a}$  in (3.14) with  $\mathbf{u}$  fixed, then  $\mathbf{u}$  with  $\mathbf{a}$  fixed. The second is a variation on the truncated power method [84], whose iterations consist of applications of the matrix  $\mathbf{A}$  (just like the standard power method) followed by a projection to enforce the structural constraints: low-rank structure as in (3.14) or block-wise low-rank structure in the multipath case as in (3.16).

### 3.4.1 An alternating eigenvectors method

While the problem in (3.14) is non-convex, it becomes tractable if either of the terms in the tensor constraint are held constant. If we have an estimate  $\hat{\mathbf{u}}$  for  $\mathbf{u}$ , and fix  $\mathbf{u} = \hat{\mathbf{u}}$ , then we can solve for the optimal  $\mathbf{a}$  with

$$\underset{\mathbf{a}}{\text{minimize}} \quad \mathbf{a}^* \mathbf{A}_{\hat{\mathbf{u}}} \mathbf{a} \quad \text{subject to} \quad \|\mathbf{a}\|_2 = 1,$$

where

$$\mathbf{A}_{\hat{\mathbf{u}}} = (\mathbf{I}_M \otimes \hat{\mathbf{u}})^* \mathbf{A} (\mathbf{I}_M \otimes \hat{\mathbf{u}}), \quad \mathbf{I}_M \otimes \hat{\mathbf{u}} = \begin{bmatrix} \hat{\mathbf{u}} & \mathbf{0} & \dots & \mathbf{0} \\ \mathbf{0} & \hat{\mathbf{u}} & \dots & \mathbf{0} \\ \vdots & \vdots & \ddots & \vdots \\ \mathbf{0} & \mathbf{0} & \dots & \hat{\mathbf{u}} \end{bmatrix}.$$

The solution is the eigenvector corresponding to the smallest eigenvalue of  $\mathbf{A}_{\hat{\mathbf{u}}}$ . Similarly, with an estimate  $\hat{\mathbf{a}} = [\hat{a}_1, \dots, \hat{a}_M]^\top$  fixed in for  $\mathbf{a}$  for the next step, we solve

$$\underset{\mathbf{u}}{\text{minimize}} \quad \mathbf{u}^* \mathbf{A}_{\hat{\mathbf{a}}} \mathbf{u} \quad \text{subject to} \quad \|\mathbf{u}\|_2 = 1,$$

where

$$\mathbf{A}_{\hat{\mathbf{a}}} = (\hat{\mathbf{a}} \otimes \mathbf{I}_D)^* \mathbf{A} (\hat{\mathbf{a}} \otimes \mathbf{I}_D), \quad \hat{\mathbf{a}} \otimes \mathbf{I}_D = \begin{bmatrix} \hat{a}_1 \mathbf{I} \\ \hat{a}_2 \mathbf{I} \\ \vdots \\ \hat{a}_M \mathbf{I} \end{bmatrix},$$

which again can be solved by founding the smallest eigenvector of  $\mathbf{A}_{\hat{\mathbf{a}}}$ .

We summarize this method of “alternating eigenvectors” in Algorithm 1. The function `MinEigVector` returns the eigenvector of the input matrix corresponding to its smallest eigenvalue.

---

**Algorithm 1:** Alternating Eigenvectors

---

**input :**  $\mathbf{A}, \mathbf{u}_0$   
**output:**  $\hat{\mathbf{h}}$   
1  $\hat{\mathbf{u}} \leftarrow \mathbf{u}_0$ ;  
2 **while** *stop condition not satisfied* **do**  
3      $\hat{\mathbf{a}} \leftarrow \text{MinEigVector}((\mathbf{I}_M \otimes \hat{\mathbf{u}}^*) \mathbf{A} (\mathbf{I}_M \otimes \hat{\mathbf{u}}))$ ;  
4      $\hat{\mathbf{u}} \leftarrow \text{MinEigVector}((\hat{\mathbf{a}}^* \otimes \mathbf{I}_D) \mathbf{A} (\hat{\mathbf{a}} \otimes \mathbf{I}_D))$ ;  
5 **end**  
6  $\hat{\mathbf{h}} \leftarrow \Phi(\hat{\mathbf{a}} \otimes \hat{\mathbf{u}})$ ;

---

### 3.4.2 A truncated power method

A standard tool from numerical linear algebra to compute the largest eigenvector of a symmetric matrix is the power method, where the matrix is iteratively applied to a starting vector, with renormalization at each step. The same method can be used to compute the smallest eigenvector simply by subtracting the matrix from an appropriate scalar multiple of the identity. In [84], a variation on this algorithm was introduced to force the iterates to be sparse. This was done by hard thresholding after each application of the matrix.

Our rank-1 truncated power method follows the same template. We create a matrix  $\mathbf{B}$  by subtracting  $\mathbf{A}$  above from a multiple of the identity. For multipath

bilinear channel models, our method is a slightly different block-wise rank-1 truncated power method, which we denote by  $\tilde{\mathbf{A}}$  and  $\tilde{\mathbf{B}}$ .

$$\mathbf{B} = \gamma \mathbf{I}_{MD} - \mathbf{A},$$

We then iteratively apply  $\mathbf{B}$  starting with an initial vector  $\mathbf{u}_0$ . After each application of  $\mathbf{B}$ , we project the result onto the set of rank-1 matrices by computing the singular vector corresponding to the largest singular value, and then renormalize.

The “iterative truncated power method” is summarized in Algorithm 2, to find an approximate solution to (3.16).

---

**Algorithm 2:** Iterative Truncated Power Method

---

**input** :  $\mathbf{Y}^* \mathbf{Y}$ ,  $\tilde{\Phi}$ ,  $\hat{\mathbf{u}}_1, \dots, \hat{\mathbf{u}}_N$ ,  $\hat{\mathbf{a}}_1, \dots, \hat{\mathbf{a}}_N$   
**output:**  $\hat{\mathbf{h}}$   
1  $\mathbf{X}_0 \leftarrow [(\hat{\mathbf{a}}_1 \otimes \hat{\mathbf{u}}_1)^\top, \dots, (\hat{\mathbf{a}}_N \otimes \hat{\mathbf{u}}_N)^\top]^\top$ ;  
2  $\tilde{\mathbf{A}} \leftarrow \tilde{\Phi}^\top (\mathbf{Y}^\top \mathbf{Y}) \tilde{\Phi}$ ;  
3  $\gamma \leftarrow \|\tilde{\mathbf{A}}\|_*$ ;  
4 **while** *stop condition not satisfied* **do**  
5      $\mathbf{X} \leftarrow \gamma \mathbf{X}_0 - \tilde{\mathbf{A}} \mathbf{X}_0$ ;  
6      $\hat{\mathbf{u}}_1, \dots, \hat{\mathbf{u}}_N, \hat{\mathbf{a}}_1, \dots, \hat{\mathbf{a}}_N \leftarrow \text{BlockRank1Approx}(\mathbf{X})$ ;  
7      $\mathbf{X}_0 \leftarrow [(\hat{\mathbf{a}}_1 \otimes \hat{\mathbf{u}}_1)^\top, \dots, (\hat{\mathbf{a}}_N \otimes \hat{\mathbf{u}}_N)^\top]^\top$ ;  
8      $\mathbf{X}_0 \leftarrow \frac{\mathbf{X}_0}{\|\mathbf{X}_0\|_2}$  ;  
9 **end**  
10  $\hat{\mathbf{h}} \leftarrow \tilde{\Phi}[(\mathbf{a}_1 \otimes \mathbf{u}_1)^\top, \dots, (\mathbf{a}_N \otimes \mathbf{u}_N)^\top]^\top$ ;

---

In this algorithm, the nonnegative constraint on the elements of  $\mathbf{a}$  is not explicitly enforced. Some care must be taken in choosing the value of  $\gamma$ . We want to ensure that the smallest eigenvalue of  $\mathbf{A}$  gets mapped to the largest (in magnitude) eigenvalue of  $\mathbf{B}$ , but we also want the relative gap between the largest and second largest eigenvalues of  $\mathbf{B}$  to be as large as possible. In our algorithm, we use  $\gamma = \|\tilde{\mathbf{A}}\|_*$ ; in our analysis below, we use a conservative value of  $\gamma = \mathbb{E}[\|\mathbf{A}\|]$ .

### 3.4.3 Spectral initialization.

Both the alternating eigenvectors method and the rank-1 truncated power method require an initial estimate of the channel gains  $\mathbf{a}$  and the basis coefficients  $\mathbf{u}$ . Because the program they are trying to solve is non-convex, this starting point is important. The performance of the method relies critically on constructing a feasible starting point. Designing a good initialization scheme is critical so that the alternating minimization won't get stuck in local minimum.

Our spectral initialization is inspired from the lifting reformulation (e.g., see [26] for the lifting in blind deconvolution). The measurements equations  $\mathbf{y}_m = \mathbf{h}_m \circledast \mathbf{x} + \mathbf{w}_m$ , can be recast as a linear operator acting on a  $L \times D \times M$  tensor formed from the Kronecker products of the unknowns  $\mathbf{x}, \mathbf{u}, \mathbf{a}$ . Let  $\mathcal{A} : \mathbb{C}^{LDM} \rightarrow \mathbb{C}^{ML}$  be a linear map such that<sup>1</sup>

$$\mathcal{A}(\mathbf{x} \otimes \mathbf{u} \otimes \mathbf{a}) = \begin{bmatrix} \mathbf{x} \circledast a_1 \mathbf{S}^* \Phi_1 \mathbf{u} \\ \vdots \\ \mathbf{x} \circledast a_M \mathbf{S}^* \Phi_M \mathbf{u} \end{bmatrix}, \quad \text{where} \quad \mathbf{S} := \begin{bmatrix} \mathbf{I}_K & \mathbf{0}_{K,L-K} \end{bmatrix}. \quad (3.17)$$

Concatenating the  $\{\mathbf{y}_m\}$  and  $\{\mathbf{w}_m\}$  into single vectors of length  $ML$ , we can rewrite measurements equations as

$$\mathbf{y} = \mathcal{A}(\mathcal{X}) + \mathbf{w},$$

where  $\mathcal{X} = \mathbf{x} \otimes \mathbf{u} \otimes \mathbf{a}$ .

A natural initialization scheme is to apply the adjoint of  $\mathcal{A}$  to  $\mathbf{y}$ , then project the result onto the feasible set of vectors that can be arranged as rank-1 tensors (this technique is often used to initialize non-convex programs for recovering rank-1 matrices from linear measurements [85, 86]). However, there is no known algorithm

---

<sup>1</sup>We have defined how  $\mathcal{A}$  operates on length  $LDM$  vectors that can be arranged as rank-1 tensors. Its action on a general vector in  $\mathbb{C}^{LDM}$  can be derived by applying the expression in (3.17) to a series of  $LDM$  vectors that form a separable basis for tensors in  $\mathbb{C}^L \times \mathbb{C}^D \times \mathbb{C}^M$ .

for computing the projection onto the set of rank-1 tensors that has strong optimality guarantees.

We avoid this by exploiting the structure on the factor  $\mathbf{a} = [a_1, \dots, a_M]^\top$  that enforces  $a_m \geq 0$  for all  $m = 1, \dots, M$ . The action of the operator  $(\mathbf{I}_{LD} \otimes \mathbf{1}_{1,M})$  has the effect of summing down the third mode of the tensor; in particular

$$(\mathbf{I}_{LD} \otimes \mathbf{1}_{1,M})(\mathbf{x} \otimes \mathbf{u} \otimes \mathbf{a}) = \left( \sum_{m=1}^M a_m \right) (\mathbf{x} \otimes \mathbf{u}).$$

When the factor  $\sum_{m=1}^M a_m$  has a sufficiently large magnitude, we can get an estimate of  $\mathbf{x} \otimes \mathbf{u}$  by applying this operator to  $\mathcal{A}^* \mathbf{y}$ . This is the case if the channel gains are positive. However, without the positivity constraint on  $\mathbf{a}$ , the factor can be arbitrary small in magnitude, which may turn the initialization vulnerable to noise. The positivity constraint on  $\mathbf{a}$  can be weakened if estimates of the phases of  $a_1, \dots, a_M$  are available as prior information. In this scenario, the known phase information is absorbed into the basis  $\Phi$  and one can focus on estimating only the gains.

The first step of our initialization, then, is to compute

$$\mathbf{\Gamma} = \text{mat}((\mathbf{I}_{LD} \otimes \mathbf{1}_{1,M})\mathcal{A}^* \mathbf{y}), \quad (3.18)$$

where the operator  $\text{mat}(\cdot)$  takes a vector in  $\mathbb{C}^{LD}$  and produces a  $D \times L$  matrix by column-major ordering.

Once corrected for noise, the leading eigenvector of  $\mathbf{\Gamma} \mathbf{\Gamma}^*$  gives us a rough estimate of the channel coefficients  $\mathbf{u}$ . In Appendix B, we show that the random matrix  $\mathbf{\Gamma} \mathbf{\Gamma}^* - \sigma_w^2 L \sum_{m=1}^M \Phi_m^* \Phi_m$  concentrates around a scalar multiple of  $\mathbf{u} \mathbf{u}^*$ .

Finally, we note that there is a closed-form expression for computing  $\mathbf{\Gamma}$  from the measurements  $\{\mathbf{y}_m\}$ . This is given in the following lemma that is proved in Appendix C.3.



**Lemma 3.4.1.** *The matrix  $\Gamma$  in (3.18) can be written as*

$$\Gamma = \sum_{m=1}^M \Phi_m^* \mathbf{S} \mathbf{C}_{\mathbf{y}_m} \mathfrak{J}, \quad (3.19)$$

where  $\mathbf{C}_{\mathbf{y}_m} \in \mathbb{C}^{L \times L}$  is the matrix whose action is the circular convolution with  $\mathbf{y}_m \in \mathbb{C}^L$ ,  $\mathfrak{J}$  is the “flip operator” modulo  $L$ :

$$\mathfrak{J} := \begin{bmatrix} \mathbf{e}_1 & \mathbf{e}_L & \mathbf{e}_{L-1} & \cdots & \mathbf{e}_2 \end{bmatrix}, \quad (3.20)$$

and  $\mathbf{e}_1, \dots, \mathbf{e}_L$  are the standard basis vectors for  $\mathbb{R}^L$ .

We summarize our spectral initialization technique in Algorithm 3.

---

**Algorithm 3:** Spectral Initialization

---

**input :**  $\{\mathbf{y}_m\}_{m=1}^M$ ,  $\{\Phi_m\}_{m=1}^M$ ,  $L$ , and an estimate of noise variance  $\hat{\sigma}_w^2$   
**output:**  $\mathbf{u}_0$   
**1**  $\Gamma \leftarrow \sum_{m=1}^M \Phi_m^* \mathbf{S} \mathbf{C}_{\mathbf{y}_m} \mathfrak{J};$   
**2**  $\mathbf{u}_0 \leftarrow \text{MaxEigVector}(\Gamma \Gamma^* - \hat{\sigma}_w^2 L \sum_{m=1}^M \Phi_m^* \Phi_m);$

---

### 3.5 Main Results

Our main results give non-asymptotic performance guarantees for both Algorithm 1 and Algorithm 2 when their iterations start from the initial estimate by Algorithm 3 under the following two assumptions:

(A1) **Generic subspaces.** The random matrices  $\Phi_1, \dots, \Phi_M$  are independent copies of a  $K$ -by- $D$  complex Gaussian matrix whose entries are independent and identically distributed (iid) as  $\mathcal{CN}(0, 1)$ . Our theorems below hold with high probability with respect to  $(\Phi_m)_{m=1}^M$ .

(A2) **Random noise.** The perturbations to the measurements  $\mathbf{w}_1, \dots, \mathbf{w}_M \in \mathbb{C}^L$  are independent subgaussian vectors with  $\mathbb{E}[\mathbf{w}_m] = \mathbf{0}$  and  $\mathbb{E}[\mathbf{w}_m \mathbf{w}_m^*] = \sigma_w^2 \mathbf{I}_L$ ,

and are independent of the bases  $(\Phi_m)_{m=1}^M$ .

We present main theorems in two different scenarios. In the first scenario, we assume that the input source is a white subgaussian random process. In the second scenario, we assume that the input source satisfies an incoherence condition that essentially ensures that it is not too concentrated in the frequency domain (a characteristic that a random source has with high probability). The error bound for the deterministic model is more general but is also slightly weaker than the random model.

The theorems provide sufficient conditions on the observation length  $L$  implying that the estimation error will fall below a certain threshold. The number of samples in these sufficient conditions will depend on the length of the CIR  $K$ , their intrinsic dimensions  $D$ , the number of channels  $M$ , and the signal-to-noise-ratio (SNR) defined as

$$\eta := \frac{\mathbb{E}_{\phi}[\sum_{m=1}^M \|\mathbf{h}_m \otimes \mathbf{x}\|_2^2]}{\mathbb{E}_{\mathbf{w}}[\sum_{m=1}^M \|\mathbf{w}_m\|_2^2]}.$$
 (3.21)

Under (A1) and (A2), it follows from the commutativity of convolution and expectation of structured random matrices derived in [83] that  $\eta$  simplifies to

$$\eta = \frac{K \|\mathbf{x}\|_2^2 \|\mathbf{u}\|_2^2}{ML\sigma_w^2}.$$
 (3.22)

In addition, the bounds will depend on the spread of the channel gains. We measure this disparity using the two flatness parameters

$$\mu := \max_{1 \leq m \leq M} \frac{\sqrt{M}a_m}{\|\mathbf{a}\|_2}$$
 (3.23)

and

$$\nu := \min_{1 \leq m \leq M} \frac{\sqrt{M}a_m}{\|\mathbf{a}\|_2}.$$
 (3.24)

Our results are most interesting when there are not too many weak channels, meaning

$\mu = O(1)$  and  $\nu = \Omega(1)$ . To simplify the theorem statements below, we will assume these conditions on  $\mu$  and  $\nu$ .

We now present our first main result. Theorem 3.5.1 below assumes a *random common source* signal  $\mathbf{x}$ . We present guarantees for Algorithms 1 and 2 simultaneously, with  $\underline{\mathbf{h}}_t = \Phi \mathbf{v}_t$  as the channel estimate after iteration  $t$  (for the alternating eigenvectors method, take  $\mathbf{v}_t = \hat{\mathbf{a}}_t \otimes \hat{\mathbf{u}}_t$ ).

**Theorem 3.5.1** (Random Source). *We observe noisy channel outputs  $\{\mathbf{y}_m\}$  as in (3.9), with SNR  $\eta$  as in (3.21), and form a sequence of estimates  $(\underline{\mathbf{h}}_t)_{t \in \mathbb{N}}$  of the channel responses by either Algorithm 1 or Algorithm 2 from the initial estimate by Algorithm 3. Suppose assumptions (A1) and (A2) above hold. Let  $\mathbf{x}$  be a sequence of zero-mean iid subgaussian random variables with variance  $\sigma_x^2$ ,  $\eta \geq 1$ ,  $\mu = O(1)$ , and  $L \geq 3K$ .<sup>2</sup> Then for any  $\beta \in \mathbb{N}$ , there exist absolute constants  $C > 0, \alpha \in \mathbb{N}$  and constants  $C_1(\beta), C_2(\beta)$  such that if there are a sufficient number of channels,*

$$M \geq C_1(\beta) \log^\alpha(MKL), \quad (3.25)$$

*that are sufficiently long (relative to the dimension  $D$  of the subspace prior),*

$$K \geq C_1(\beta) D \log^\alpha(MKL), \quad (3.26)$$

*and we have observed the a sufficient number of samples at the output of each channel,*

$$L \geq \frac{C_1(\beta) \log^\alpha(MKL)}{\eta} \left( \frac{K}{M^2} + \frac{D}{D \wedge M} \right), \quad (3.27)$$

---

<sup>2</sup>Without the subspace prior,  $L > K$  is necessary to claim that  $\mathbf{Y}^* \mathbf{Y}$  has nullity 1 in the noiseless case. We used  $L \geq 3K$  in the proof in order to use the identity that the circular convolutions of three vectors of length  $K$  modulo  $L$  indeed coincide with their linear convolution.

then with probability exceeding  $1 - CK^{-\beta}$ , we can bound the approximation error as

$$\begin{aligned} \sin \angle(\underline{\mathbf{h}}_t, \underline{\mathbf{h}}) &\leq \\ 2^{-t} \angle(\underline{\mathbf{h}}_0, \underline{\mathbf{h}}) + C_2(\beta) \log^\alpha(MKL) &\left( \frac{1}{\sqrt{\eta L}} \left( \frac{\sqrt{K}}{M} + \sqrt{\frac{D}{D \wedge M}} \right) + \frac{\sqrt{D}}{\eta \sqrt{ML}} \right), \end{aligned} \quad (3.28)$$

$$\forall t \in \mathbb{N}.$$

We make the following remarks about the assumption (3.25) – (3.27) in Theorem 3.5.1. The lower bound on the number of channels in (3.25) is very mild,  $M$  has to be only a logarithmic factor of the number of parameters involved in the problem. The condition (3.26) allows a low-dimensional subspace, the dimension of which scales proportional to the length of filter  $K$  up to a logarithmic factor. For a fixed SNR and a large number of channels ( $M = \Omega(\sqrt{K/D})$ ), the condition in (3.27) says that the length of observation can grow proportional to  $\sqrt{KD}$  — this is suboptimal when compared to the degrees of freedom  $(M + D)/(M - 1)$  per channel. (The total number of unknowns is  $L + M + D$  and we have  $ML$  equations.) In fact, if  $L < K$ , then the circular convolution modulo  $L$  of two vectors respectively of length  $K$  and  $L$  introduces aliasing due to the wrapping around of the vector of length  $K$ . This renders the deconvolution problem into a demixing problem that separates a mixture of convolutions. While it might be still possible to uniquely identify a solution in this blind demixing problem, the deconvolution approach in this paper does not apply. In other words, the requirement  $L \geq K$  is the fundamental limitation of the linearization that leverages on the cross-convolution. However, this still marks a significant improvement over an earlier analysis of this problem [87], which depended on the concentration of subgaussian polynomial [88] and union bound arguments. The scaling laws of parameters have been sharpened significantly, and as we will see in the next section, its prediction is consistent with the empirical results by Monte Carlo simulations in Section 3.6. Compared to the analysis for the other spectral method

under the linear subspace model [83], Theorem 3.5.1 shows that the estimation error becomes smaller by factor  $\sqrt{D}$ .

To prove Theorem 3.5.1, we establish an intermediate result for the case where the input signal  $\mathbf{x}$  is deterministic. In this case, our bounds depend on the spectral norm  $\rho_{\mathbf{x}}$  of the (appropriately restricted) autocorrelation matrix of  $\mathbf{x}$ ,

$$\rho_{\mathbf{x}} := \|\tilde{\mathbf{S}}\mathbf{C}_{\mathbf{x}}^*\mathbf{C}_{\mathbf{x}}\tilde{\mathbf{S}}^*\|,$$

where

$$\tilde{\mathbf{S}} = \begin{bmatrix} \begin{bmatrix} \mathbf{0}_{K-1, L-K+1} & \mathbf{I}_{K-1} \end{bmatrix} \\ \begin{bmatrix} \mathbf{I}_{2K-1} & \mathbf{0}_{2K-1, L-2K+1} \end{bmatrix} \end{bmatrix}. \quad (3.29)$$

Then the deterministic version of our recovery result is:

**Theorem 3.5.2** (Deterministic Source). *Suppose that the same assumptions hold as in Theorem 3.5.1, only with  $\mathbf{x}$  as a fixed sequence of numbers obeying*

$$\rho_{\mathbf{x}} \leq C_3 \|\mathbf{x}\|_2^2. \quad (3.30)$$

If (3.26) and (3.25) hold, and

$$L \geq \frac{C_1(\beta) \log^\alpha(MKL)}{\eta} \left( \frac{K^2}{M^2} + \frac{KD}{D \wedge M} \right), \quad (3.31)$$

then with probability exceeding  $1 - CK^{-\beta}$ , we can bound the approximation error as

$$\sin \angle(\underline{\mathbf{h}}_t, \underline{\mathbf{h}}) \leq 2^{-t} \angle(\underline{\mathbf{h}}_0, \underline{\mathbf{h}}) + \frac{C_2(\beta) \log^\alpha(MKL)}{\sqrt{\eta}L} \left( \frac{K}{M} + \sqrt{\frac{KD}{D \wedge M}} \right), \quad \forall t \in \mathbb{N}. \quad (3.32)$$

The condition (3.30) can be interpreted as a kind of incoherence condition on the input signal  $\mathbf{x}$ . Since

$$\rho_{\mathbf{x}} \leq \|\mathbf{C}_{\mathbf{x}}\|^2 = L\|\hat{\mathbf{x}}\|_\infty^2,$$

where  $\hat{\mathbf{x}} \in \mathbb{C}^L$  is the normalized discrete Fourier transform of  $\mathbf{x}$ , it is sufficient that  $\hat{\mathbf{x}}$  is approximately flat for (3.30) to hold. This is a milder assumption than imposing an explicit stochastic model on  $\mathbf{x}$  as in Theorem 3.5.1. For the price of this relaxed condition, the requirement on  $L$  in (3.31) that activates Theorem 3.5.2 is more stringent compared to the analogous condition (3.27) in Theorem 3.5.1.

### 3.6 Numerical Simulation Results

In this section, we present empirical performance of the alternating eigenvectors method (AltEig) in Algorithm 1 and the iterative rank-1 truncated power method (RTPM) in Algorithm 2, both initialized by the spectral initialization in Algorithm 3.

First, we implement the RTPM method to solve the multichannel blind deconvolution problem using the bilinear channel model for the underwater acoustic channels. In underwater acoustic channel numerical simulations in Section 3.6.1, 3.6.2 and 3.6.3, the common driving source signal,  $\mathbf{s} \in \mathbb{R}^L$ , is Gaussian white noise filtered in an arbitrary bandwidth representative of shipping noise spectra (400 – 600 Hz). In this particular underwater channel bilinear model, AltEig does not provide stable recovery, therefore, we report the simulation results using RTPM method. The effectiveness and robustness of the RTPM algorithm are demonstrated by realistic CIRs using two sets of experimental data.

In the end of this section, we further compare the performance of our methods both in Algorithm 1 and Algorithm 2 using a generic subspace for the bilinear channel model. This also demonstrates that the empirical performance of our methods agrees with the main results in this chapter.

#### 3.6.1 NC09 noise data simulations

In this section, CIRs of receivers on an equally-spaced vertical line array are modeled as in Section 3.2 using the fact that the arrival-times of the same path for each

receiver fall along a line when the distance between the source and receivers is large. The subspace basis matrix  $\Phi$  is generated by the method described in Section 3.2, and variation limits are learned through experimental data will be specified in each following sections. We need to point out here that the linear relation for arrival-times across channels is not a necessary assumption in order for the method to work. The relation for arrival-times can be any parametric function that we know as a priori. Even when an explicit function is not available, the method only requires a collection of realizations of arrival-times to build up a library, which represents a certain source-receiver configuration and environment.

In this simulation scenario, arrival-times and amplitudes for each pulse are collected from experimental results, as well as their variation range. In this experiment, a short bottom-mounted vertical line array was moored in a shallow and nearly range-independent section of the Coronado Bank (water depth  $\approx 150$  m), approximately 20 km offshore of San Diego, CA. Based on prior studies, the environmental parameters for the test site were estimated ahead of time. The VLA had 16 elements uniformly spaced by 1 m; with the first element approximately 7 m above the sea-floor. The research vessel (R/V) New Horizon was used as a surface source of opportunity. Since no ground truth was available for the actual CIRs between the R/V and the VLA, estimated CIRs from Ray-Based Deconvolution method were used as a priori for arrival-times and amplitudes information. In order to estimate the arrival-time uncertainty for each ray-path of the CIRs, we used historical sound-speed profiles measurements from CTD casts collected in the area and representative of the ocean sound speed fluctuations ( $\approx 3$  m/s) occurring during the time period of the experiments. By running multiple ray simulations using the software BELLHOP for a source-array separation distance of 2 km, through this collection of sound-speed profiles we obtained a maximum uncertainty window of  $\Delta t = 3$  ms for all considered ray arrivals. An arrival-time window of  $\Delta t = 5$  ms was used here for  $t_1$ , and the corre-

sponding range of  $k$  is calculated with the assumption that arrival-times fall along a line. In this environmental scenario, the CIRs have 2 separate paths and the range of arrival-times for each path can be indicated by the black region in the following figure.

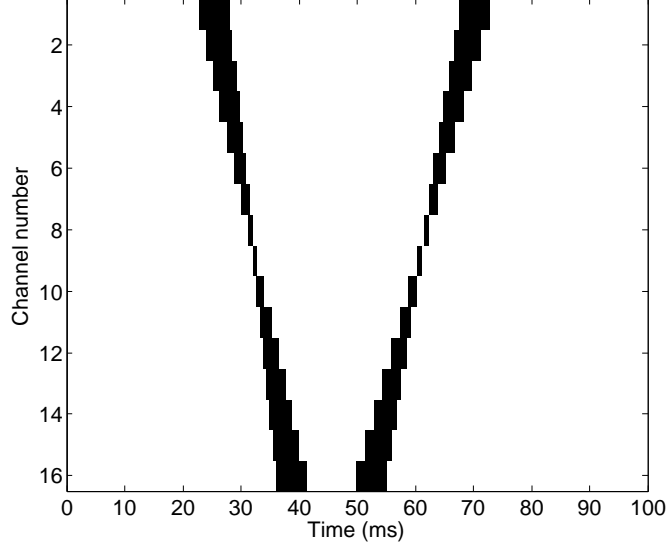


Figure 3.5: *A priori information of the ray arrival-time structure of  $M = 16$  channels for NC09 data CIRs. The black shaded region indicated the possible arrival-times of 2 separate rays. Arrival-times for each ray fall along a line.*

The measurements for each channel were convolution of a unknown common source  $\mathbf{s} \in \mathbb{R}^L$ , where  $L = 5000$ , and the unknown CIR  $\mathbf{h}_m \in \mathbb{R}^K$ , where  $K = 400$  samples and  $m = 1, \dots, 16$ . The sampling frequency is chosen to be  $f_s = 4000$  Hz. The span of the subspace for channel bilinear model was known as  $\Phi$ . The amplitudes of pulses for the same path are unknown, but they are positive valued and have a known flatness property which is described by a parameter  $\mu$ . Implementing the RTPM method, the CIRs are perfectly recovered when no measurement noise is added. The true and recovered CIRs are plotted on top of each other in Fig. 3.6a. The algorithm also maintains stable convergence performance as shown in Fig. 3.6b.



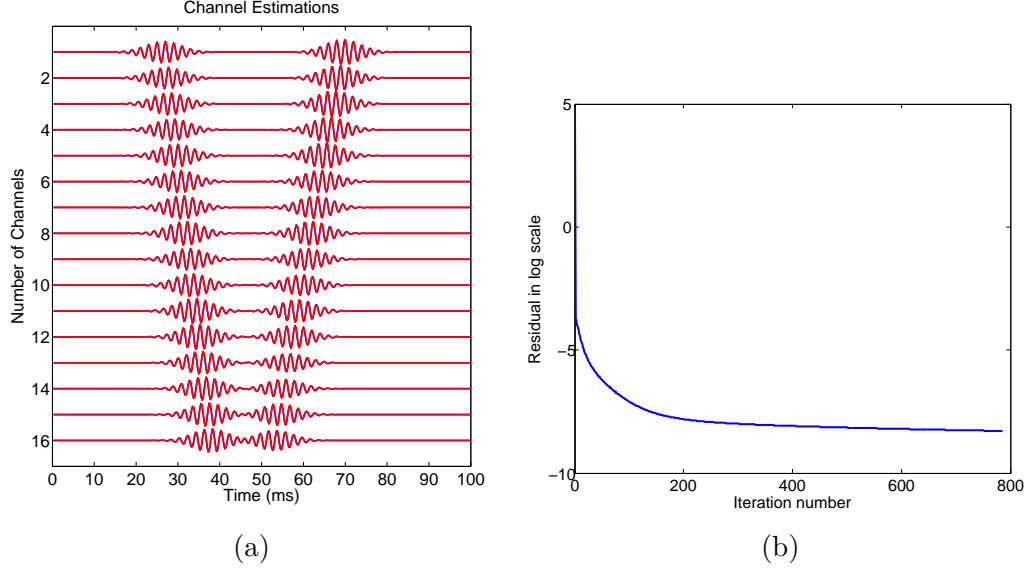


Figure 3.6: *Recovery for 16 CIRs and the convergence performance for NC09 channels. (a)  $M = 16$  multipath channels are recovery exactly using a bilinear channel model. The original CIRs and estimated CIRs are plotted on top of each other. (b) The residual in each power method iteration, and our method shows a stable convergence.*

### 3.6.2 Santa Barbara Channel experimental data simulations

In this section, we present results using bilinear channel models derived from Santa Barbara Channel experiment. Whereas in Section 3.6.1, the subspace basis  $\Phi$  is generated through varying parameters of lines, where arrival-times fall along , here we generate  $\Phi$  from a collection of realizations of arrival-times extracted by the ray-based method. A priori arrival-time information is extracted from acoustic measurements gathered during an experiment performed mid-September, 2016 in the Santa Barbara shipping channel (depth  $\approx 580$  m). The Santa Barbara Channel (SBC) operation areas and the VLA locations are plotted in Fig. 3.7. In this experiment, four 32-element VLAs were deployed in the Santa Barbara shipping channel and recorded ocean noise continuously for a week. Each array consisted of two sub-arrays of large aperture ( $\approx 56$ m) and small aperture ( $\approx 15$  m) with uniform 1 m and 3.75 m element spacing respectively. The arrays were moored between the north and south band shipping lanes where commercial vessels would be common sources of opportunity.

In addition to collecting acoustic data, the Santa Barbara experiment utilized CTD casts and bottom-profilers to obtain supplementary details of the environment, such as sound speed profiles and bathymetry information.

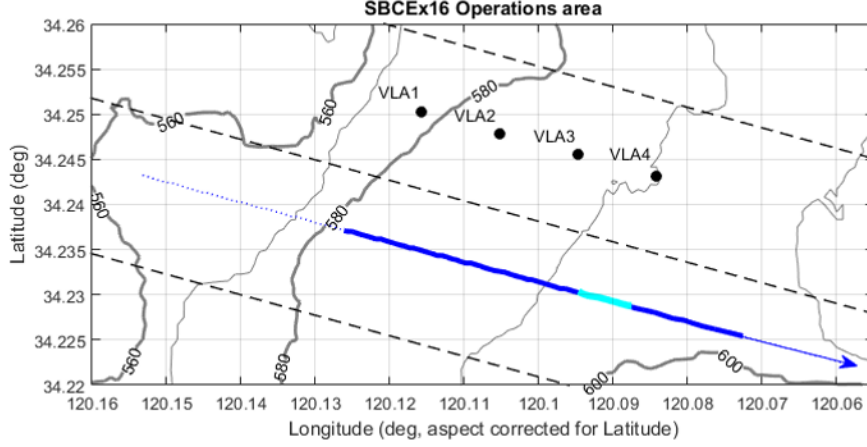


Figure 3.7: *Illustration of the Santa Barbara Channel Experiment. Four 32-elements are deployed in the Santa Barbara shipping channel. In our simulation, we used data collected from VLA3 from the source of opportunity, which is the passing container ship Anna Maersk passed by the blue line track.*

The Anna Maersk, a passing container ship, was used as a source of opportunity. The ray-based blind deconvolution (RBD) algorithm was first performed to extract arrival-times of CIRs. In our simulation, we used data collected from VLA3 when the Anna Maersk was passing on the blue track in Fig. 3.7. The RBD method was performed to deconvolve the CIRs of 500 snapshots, which are linearly spaced throughout the course of one minute (12:15:18–12:16:18) and covering ranges from 1.71 km to 1.94 km as the vessel Anna Maersk cruises further away from VLA3. Arrival-times of the direct path in all 500 snapshots are plotted in Fig. 3.8a. The arrival-time of the first receiver in all the snapshots are aligned at time  $t_0 = 20$  ms. The CIR vectors have  $K = 500$  samples, and throughout the simulation in this section, the sampling frequency is  $f_s = 10000$  Hz. Using the method described in Section III, we used 500 snapshots as a collection of realizations of CIRs and built

the subspace basis matrix  $\Phi$ , where  $\Phi$  has a dimension of 42. The multichannel blind deconvolution algorithm is then performed when the subspace basis  $\Phi$  is known. The CIRs we wish to recover is randomly chosen from the snapshots, and the recovery results is perfect with a signal-to-noise ratio 25.83 dB as shown in Fig. 3.8b.

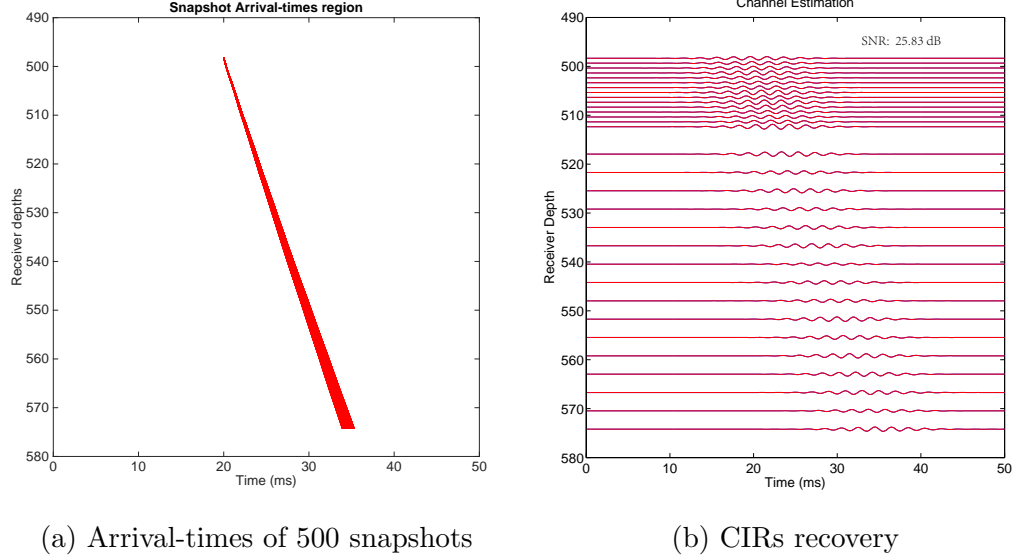


Figure 3.8: *Recovery of  $M = 31$  CIRs using bilinear channel model. (Discarded one channel from the VLA because of hardware problem) (a) 500 snapshots of arrival-times for CIRs when the ship is cruising away from VLA3 at range 1.71 km to 1.94 km. (b) The estimated CIRs (red) plot on top of the original CIRs, and the recovery SNR is 25dB.*

Building the subspace basis matrix  $\Phi$  directly from all snapshots CIRs as above can accurately approximate any realization of CIRs within the range of measurements. However, the pre-calculation of all 500 snapshots using RBD method is expensive. Since the distance between the source (Anna Maersk) and VLA3 ( $\approx 1800$  m) are larger than the total aperture of VLA3 ( $\approx 70$  m), we can well model the arrival-times of each receiver has a linear relationship with its depth. Under this assumption, if we can estimate one snapshot within the range and linearize arrival-times on a known line, the subspace basis matrix  $\Phi$  can then be built by varying the slope of the line with a fixed point (the arrival-time of the first channel). The  $\Phi$  built here by the linear assumption of all arrival-times are not as accurate as by using all snapshots,

but the dimension of the basis is much smaller. Approximating CIRs of one snapshot in this subspace will generate a model error, which is approximately 12 dB in terms of SNR. However, the multichannel blind deconvolution method introduced in section IV is robust enough and still can successfully recover the CIRs of one snapshot using only the convolution measurements and a priori information  $\Phi$ . The arrival-times on various lines are illustrated in Fig. 3.9a and the subspace basis matrix  $\Phi$  is generated from them. The CIRs recovery results are plotted in Fig. 3.9b, where the recovery SNR is 11.65 dB.

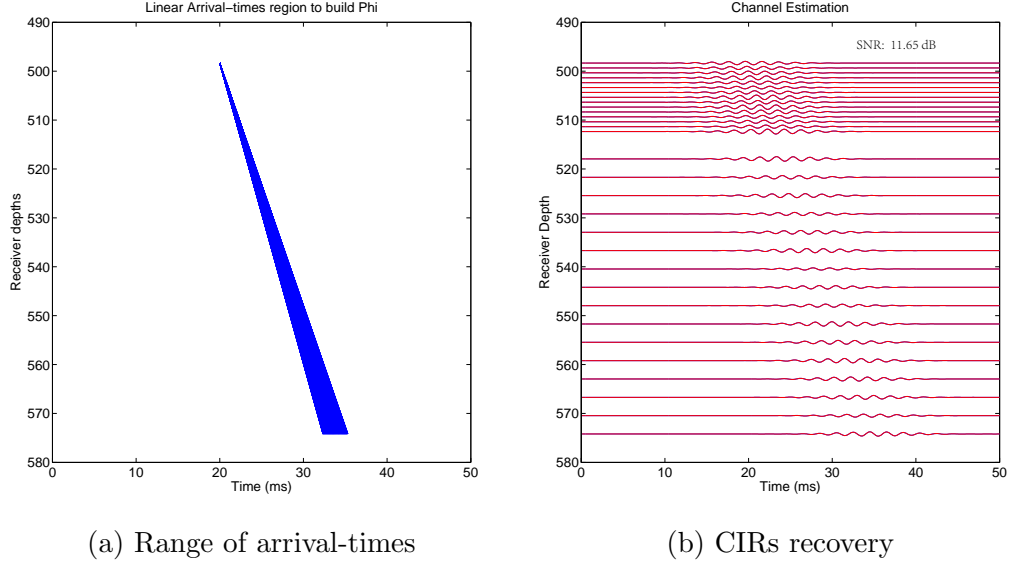


Figure 3.9: *Recovery of  $M = 31$  CIRs using bilinear channel model. (Discarded one channel from the VLA because of hardware problem) (a) Line approximations of arrival-times for CIRs when the ship is  $\approx 1.8$  km away from VLA3, the line approximations are a rough estimation of the 500 snapshots shown in Fig. 3.8a. (b) The estimated CIRs (red) plot on top of the original CIRs, and the recovery SNR is  $\approx 12$  dB.*

The simulation above shows that the RTPM blind deconvolution method is robust towards model error which is generated by arrival-time off-line non-linearity. In the next section, the robustness performance is studied carefully both in terms of model error and measurement noise.

### 3.6.3 Robustness performance in underwater acoustic channels

Robustness performance of the RTPM method for solving the multichannel blind deconvolution problem using the bilinear channel model is studied in this section. The robustness of bilinear channel model errors is first studied. In both NC09 noise data and SBC experiment data, the subspace basis matrix  $\Phi$  is build by treating all channels jointly, which is based on the linear relation of all arrival-times. However, it is very likely that arrival-times are not exactly on a line because of the disturbance in the environment. The arrival-times off-line model errors are inherited from the bilinear channel model assumption, and therefore, the robustness performance towards such error is critical in realistic applications.

The Monte-Carlo simulations are performed to estimate the robustness performance of the arrival-times off-line model error. We first used the same subspace basis matrix  $\Phi$ , which is built from all the arrival-times on various lines within the range, shown in Fig. 3.9a. The off-line model error is controlled by adding a small random perturbation that is proportional with a variable  $\sigma$ . The model approximation SNR is defined as  $10\log_{10}(\|\mathbf{h}_k\|_2/\|\mathbf{h}_k - \mathbf{h}_{k_{\text{Approx}}}\|_2)$ , where  $\mathbf{h}_{k_{\text{Approx}}}$  is an approximation of CIRs using the subspace basis  $\Phi$ . The CIR estimation SNR is defined as  $10\log_{10}(\|\mathbf{h}_k\|_2/\|\mathbf{h}_k - \mathbf{h}_{k_{\text{Estimation}}}\|_2)$ , where  $\mathbf{h}_{k_{\text{Estimation}}}$  is estimated CIRs using RTPM method. Figure 3.10 shows that with the increase of the arrival-times off-line error, the model approximation SNR decreases. However, the SNR of estimated CIRs demonstrated that the deconvolution is successful as long as the bilinear model still can well approximate the CIRs, roughly speaking above 8 dB in terms of model approximation SNR.

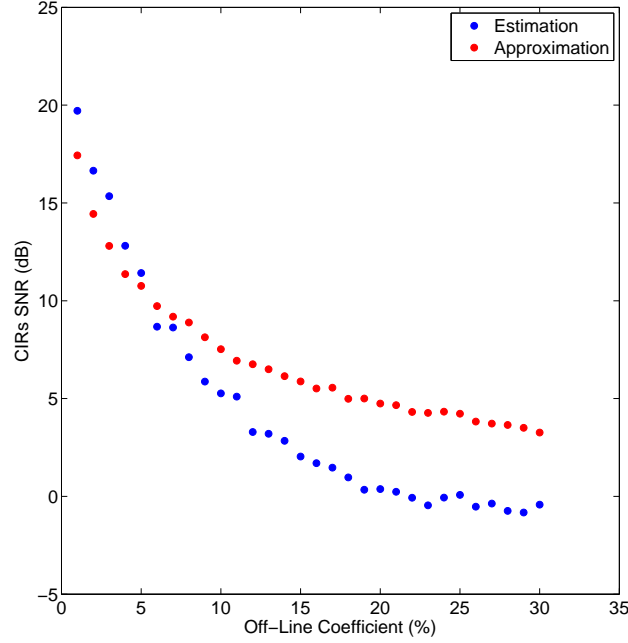


Figure 3.10: *The algorithm robustness performance when arrival-times are not exactly on a line while the bilinear model is formed with the assumption that all arrival-times fall along a line. The red dots indicate the approximation error when using such channel model, and the blue dots are the estimation error using such channel model to perform blind deconvolution. The model error are measured by a off-line coefficient which indicates the ratio between the off-line time and the arrival-time differences among channels.*

The RTPM blind deconvolution method using bilinear channel model is also able to cope with CIRs in a larger range. Figure. 3.11a indicates a larger range of possible arrival-times, and another subspace basis matrix  $\Phi$  is constructed using the same technique as before. As the range of the arrival-times increases, so does the dimension of the basis. The following Monte-Carlo simulations shown in Fig. 3.11b demonstrates that the method is still robust towards the arrival-times off-line model errors. The simulations are run identically as the previous Monte-Carlo simulation except the choice of  $\Phi$  as a priori information. We observed that the SNRs of estimated CIRs are slightly worse than the results in Fig. 3.10.

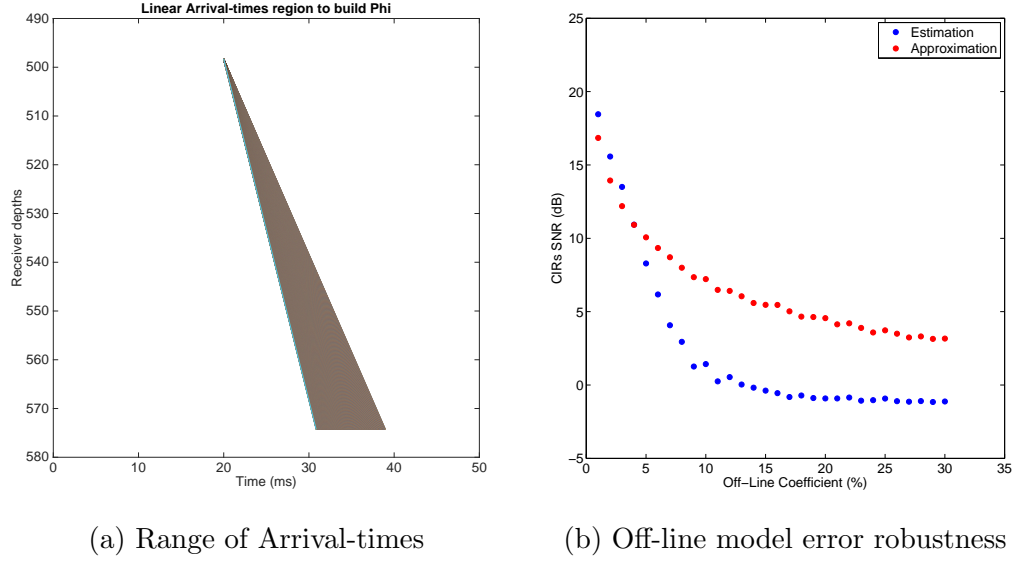


Figure 3.11: (a) Compared to Fig. 3.9a, a subspace with a larger dimension is used in this simulation, which is generated from a wider range of lines. (b) The red dots indicate the approximation error when using such channel model, and the blue dots are the estimation error using such channel model to perform blind deconvolution. The model error are measured by a off-line coefficient which indicates the ratio between the off-line time and the arrival-time differences among channels.

The robustness performance towards the measurement noise is then studied using SBC arrival-times information. White gaussian noises are added to the measurements of each channel. The noise level SNR is defined as  $\text{SNR} = 10\log_{10}(\|\mathbf{y}_k\|_2/\|\mathbf{e}_k\|_2)$ , and the CIR recovery SNR is defined as  $10\log_{10}(\|\mathbf{h}_k\|_2/\|\mathbf{h}_k - \mathbf{h}_{k_{\text{Approx}}}\|_2)$ . In this trial of simulations, the model error is not included. A Monte Carlo simulation with  $T = 100$  trials for each noise level is conducted and a stable robustness performance against the measurement noise is demonstrated in Fig. 3.12.

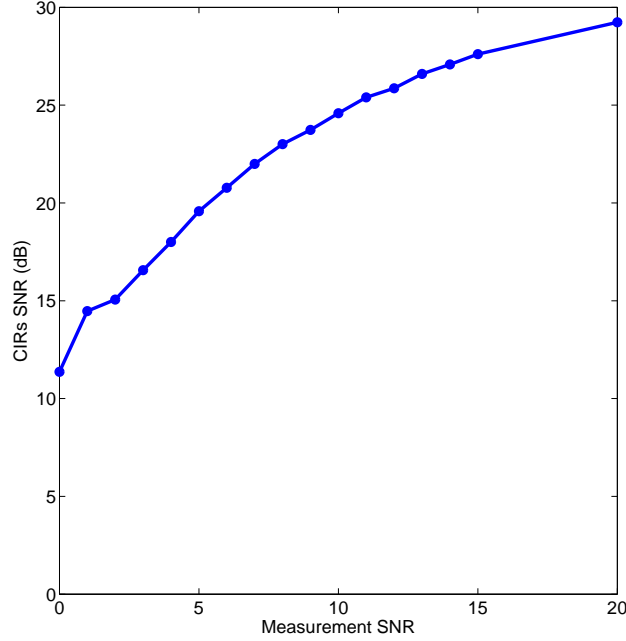


Figure 3.12: Monte Carlo simulation for recovery performance with noisy measurements.

#### 3.6.4 Robustness performance using generic subspaces

In this section, we provide observation on empirical performance of the alternating eigenvectors method (AltEig) in Algorithm 1 and the rank-1 truncated power method (RTPM) in Algorithm 2, both initialized by the spectral initialization in Algorithm 3. We compare the two iterative algorithms to the classical cross-convolution method (CC) by Xu et al. [1], which only imposes the time-limited model on impulse responses, and to the subspace-constrained cross-convolution method (SCCC) [83], which imposes a linear subspace model on impulse responses. This comparison will demonstrate how the estimation error improves progressively as we impose a stronger prior model (bilinear channel model) on impulse responses.

In our first experiment, we tested the algorithms on generic data where the basis  $\Phi$  is an i.i.d. Gaussian matrix. The input source signal  $\mathbf{x}$ , subspace coefficient vector  $\mathbf{b}$ , and additive noise are i.i.d. Gaussian too. The channel gain vector is generated by adding random perturbation to all-one vector so that  $\mathbf{a} = \mathbf{1}_{M,1} + \alpha \boldsymbol{\xi} / \|\boldsymbol{\xi}\|_\infty$ , where



$\boldsymbol{\xi} = [\xi_1, \dots, \xi_M]^\top$  and  $\xi_1, \dots, \xi_M$  are independent copies of a uniform random variable on  $[-1, 1)$ . We use a performance metric given as the 95th percentile of the estimation error in the sine of the principal angle between the estimate and the ground truth out of 1,000 trials. This amounts to the error for the worst-case except 5% of the instances. In other words, the estimation error is less than this threshold with high probability no less than 0.95.

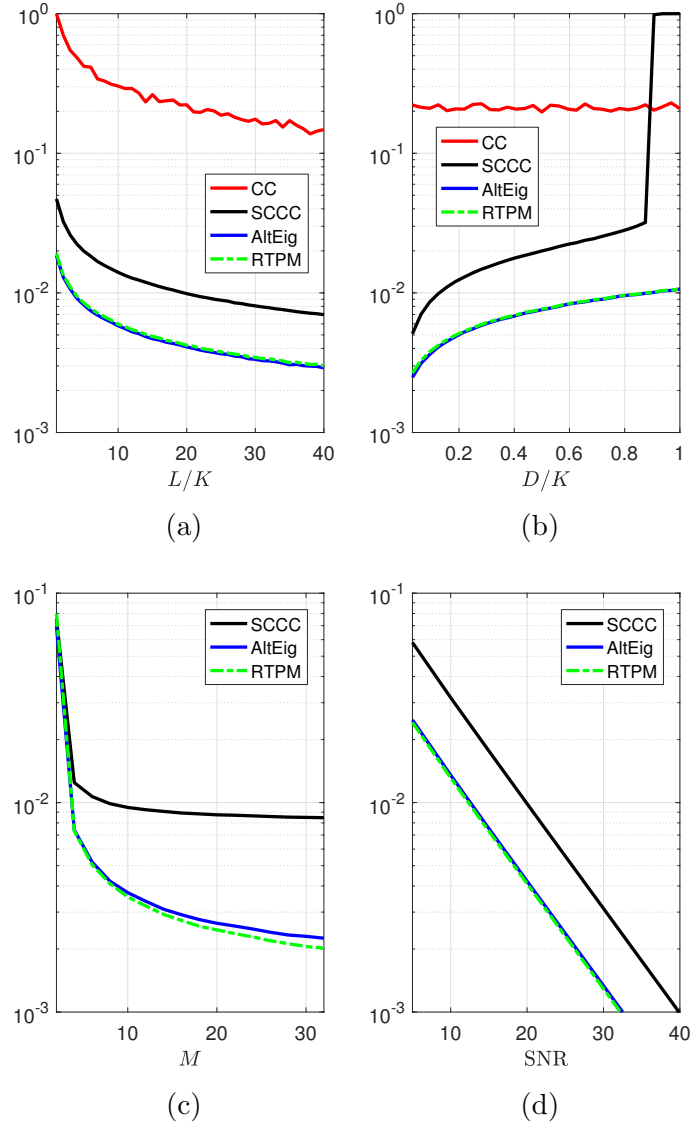


Figure 3.13: Comparison of cross-convolution (CC), subspace-constrained cross-convolution (SCCC), alternating eigenvectors method (AltEig), and rank-1 truncated power method (RTPM). Default parameter setting:  $M = 8$ ,  $K = 256$ ,  $D = 32$ ,  $L = 20K$ ,  $\text{SNR} = 20$  dB. The 95th percentile estimation error is plotted in a logarithmic scale as we vary each parameter as follows: (a)  $L$ , (b)  $D$ , (c)  $M$ , (d) SNR.

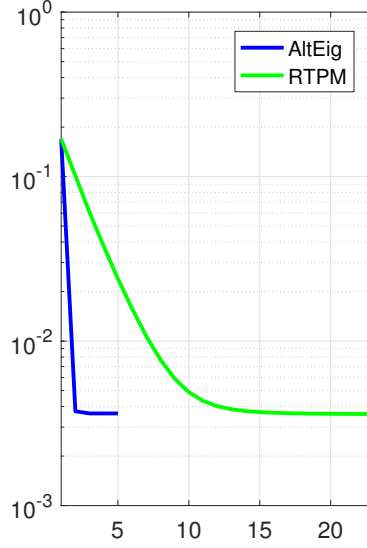


Figure 3.14: Convergence of alternating eigenvectors method (AltEig) and rank-1 truncated power method (RTPM) for a random instance.  $x$ -axis: iteration index,  $y$ -axis: log of the estimation error.  $M = 8$ ,  $K = 256$ ,  $D = 32$ ,  $L = 20K$ ,  $\text{SNR} = 20$  dB.

Figure 3.13 compares the estimation error by the four algorithms as we vary the problem parameters. Figure 3.13a shows that the error as a function of the oversampling factor  $L/K$ , which is the ratio of the length of observation  $L$  to the number of nonzero coefficients in each impulse response. SCCC provides smaller estimation error than CC in order of magnitude by exploiting the additional linear subspace prior. Then AltEig and RTPM provide further reduced estimation error again in order of magnitude compared to SCCC by exploiting the bilinear prior that imposes the separability structure in addition to the linear subspace prior. As expected, longer observation provides smaller estimation error for all methods. Furthermore, as shown in Figure 3.13b, the estimation error increases as a function of the ratio  $D/K$ , which accounts for the relative dimension of the subspace. More interestingly, as our main theorems imply, the performance difference between SCCC and AltEig/RTPM becomes more significant as we add more channels (Figure 3.13c). The estimation error by these method scales proportionally as a function of SNR (Figure 3.13d). More-

over, when the two iterative algorithms (AltEig and RTPM) provide stable estimate, they converge fast. Figure 3.14 illustrate the convergence of the two algorithms for a random instance. The estimation error decays progressively for RTPM, whereas AltEig converges faster within less than 5 iterations. However AltEig is not as stable as RTPM working with our acoustic channel subspace.

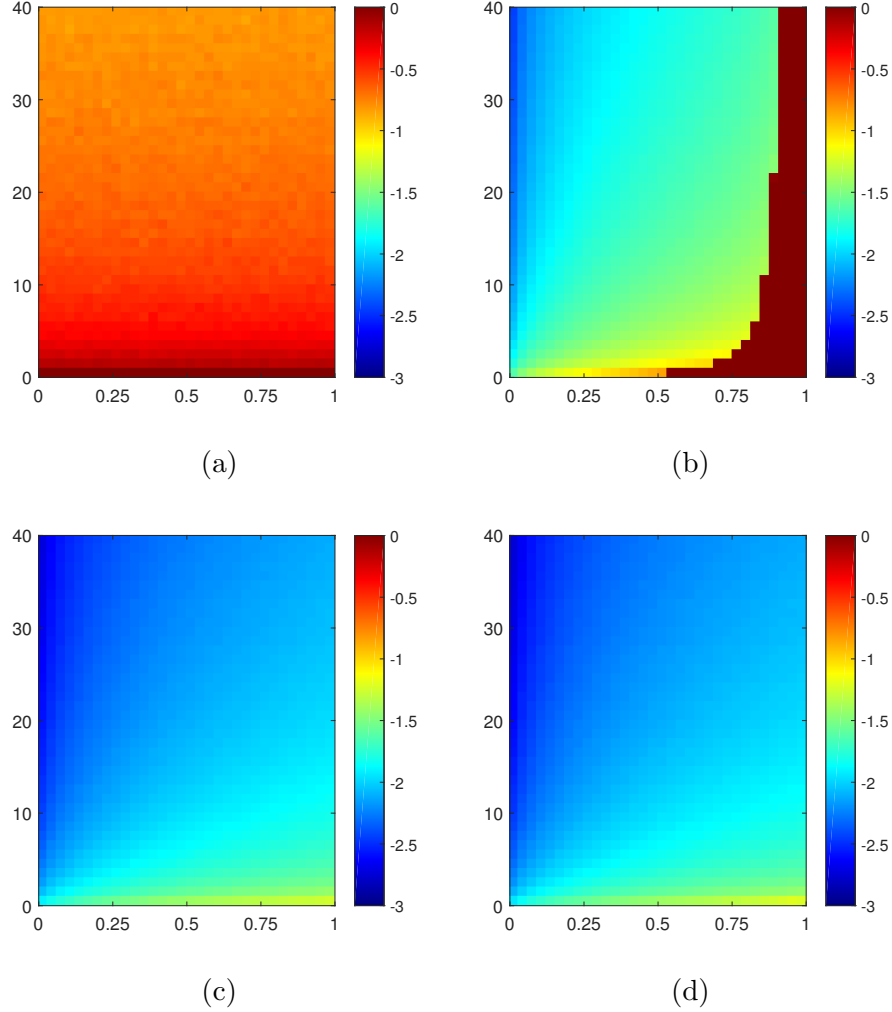


Figure 3.15: *Empirical phase transition in the 95th percentile of the log of the estimation error.  $x$ -axis:  $D/K$ .  $y$ -axis:  $L/K$ .  $K = 256$ ,  $M = 8$ ,  $\text{SNR} = 20$  dB. (a) cross-convolution method [1]. (2) subspace-constrained cross-convolution method [83]. (c) alternating eigenvectors method ( $\hat{\sigma}_w^2 = \sigma_w^2$ ). (d) rank-1 truncated power method ( $\hat{\sigma}_w^2 = \sigma_w^2$ ).*

To better visualize the overall trend, we performed a Monte Carlo simulation for the empirical phase transition, which is illustrated in Figure 3.15 with a color coding

that uses a logarithmic scale with blue denoting the smallest and red the largest error within the regime of  $(D/K, L/K)$ . The error in the estimate by CC is large ( $\geq 0.1$ ) regardless of  $D/K$  for the entire regime (Figure 3.15a). SCCC provides accurate estimates for small  $D/K$  and for large enough  $L/K$  (Figure 3.15b). On the other hand, it totally fails unless the dimension  $D$  of subspace is not less than a certain threshold. Finally, AltEig and RTPM show almost the same empirical phase transitions, which imply robust recovery for larger  $D/K$  and for smaller  $L/K$  (Figures 3.15c and 3.15d).

### 3.7 Conclusion

We studied two iterative algorithms and their performances for a multichannel blind deconvolution that imposes a bilinear model on CIRs and implemented our method on real world underwater acoustic channels. Such a bilinear model is obtained, for example, by embedding a parametric model for the shapes of pulses *jointly* into a low-dimensional subspace through manifold embedding, while the channel gains are treated as independent variables. Under the bilinear model, we modified classical cross-convolution method based on the commutativity of the convolution to overcome its critical weakness of sensitivity to noise. The bilinear system model imposes a strong prior on the unknown channel impulse responses, which enables us to recover the system with short observation. The constraint enforced by the bilinear model, on the other hand, makes the recovery no longer a simple eigenvalue decomposition problem. We propose two iterative algorithms along with a simple spectral initialization. We have shown that the proposed algorithms converge linearly to a stable estimate of the unknown channel parameters when the basis in the bilinear model is generic. In the end, our methods are validated by series of experimentally derived simulations using at-sea data recorded in shallow water from short vertical line arrays at Coronado Bank and Santa Barbara shipping channel.

## CHAPTER 4

### SUBSPACE LEARNING FOR MULTICHANNEL DECONVOLUTION

#### 4.1 Introduction

The multichannel blind deconvolution methods presented in Chapter 2 and Chapter 3 rely on the exploitation of the channel structure to solve the multichannel blind deconvolution problem. In Chapter 2 and Chapter 3, we have examined two types of channel models: the linear model and bilinear model. Our deconvolution methods are based on the fact that we have a priori knowledge about the channel impulse responses, namely that it lies in a low-dimensional subspace, and that we can estimate this subspace beforehand.

In this chapter, we investigate how to estimate the low-dimensional subspace that can represent the CIRs of all snapshots from indirect measurements of the CIRs. The technique to build the subspace for underwater acoustic channels in previous chapters relies on performing a ray-based method to learn all possible arrival-times, and then we can construct the subspace for the CIRs using Principal Component Analysis (PCA). However, ray-based methods usually require a long observation time for each measurement and we need many measurements to learn all possible arrival-times, which is time-consuming to perform. Moreover, the subspace we built using a priori knowledge might not be accurate, and our previous deconvolution methods would break down from a large subspace model error. Therefore, we investigate subspace learning methods by using multiple snapshots of convolutive measurements, which we can use to learn the subspace without using PCA and increase the accuracy and robustness of the channel model. We will introduce two algorithms to solve the

subspace learning problem and provide brief descriptions in a later section.

Subspace learning is a dimensionality reduction technique that has a wide variety of applications such as image compression [89], face recognition [90] and computer vision [91], etc. Many of current subspace learning algorithms are based on least squares estimation techniques and using “full” data, such as principal component analysis (PCA), linear discriminant analysis (LDA), and locality preserving projection. Our approach to address the problem is to learn the subspace from indirect nonlinear measurements by solving optimization problems. In our approach, we learn the subspace and perform the multichannel blind deconvolution simultaneously. We mathematically formulate the problem in a later section, taking advantage of the multiple snapshots of the convolutive measurements between CIRs and the unknown source signals.

The problem scenario is motivated by the fact that in many real world applications of the multichannel deconvolution problem we can observe multiple snapshots of convolutions between time-variant CIRs and source signals. In each snapshot, the source signal is time-invariant and uncorrelated from other snapshots, and the CIRs are time-invariant and vary slightly from other snapshots. Therefore, the CIRs of all snapshots are highly correlated, and the CIRs can be well modeled by a fixed subspace. For example, in underwater acoustic channels, receivers on a Vertical Line Array (VLA) can keep measuring all sources of opportunity (e.g. ship noise) in a region. We can have multiple snapshots of measurements when a ship passes by the region, and the CIRs in each snapshot vary slightly because the ship travels a short distance against the VLA in each snapshot. As we studied in previous chapters, when the region is small, the arrival times of the pulses among all snapshots are close to each other and the CIRs are highly correlated. Therefore, a low-dimensional subspace exists for the CIRs of all snapshots. We can further populate the collection of snapshots when other ships pass the same region. Knowing the existence of a

low-dimensional subspace for all CIRs of multiple snapshots, we want to learn the subspace and deconvolve the CIRs.

Applications of subspace learning for multichannel deconvolution are not only found in our study of underwater acoustic channels. We can apply our methods to any multichannel deconvolution problems where the CIRs of all snapshots lie in a low-dimensional subspace and learn the subspace model from multiple snapshots of convolutive measurements. For example, the subspace learning method can also be applied in the auto-calibration process of the multi-coil dynamic MRI and sensor array networks, where the CIRs are correlated in each snapshot.

The rest of the chapter is organized as follows. Section 4.2 presents the mathematical formulations of the subspace learning for multichannel blind deconvolution from multiple snapshots. Section 4.3 discusses our algorithms and necessary calculation details in solving the problem by optimizing over a Grassmannian manifold and using low-rank matrix recovery. Section 4.4 presents the numeric results of our methods and demonstrates the effectiveness and robustness performance of our methods.

## 4.2 Subspace Learning Problem Formulation

We first recall the multichannel measurements scenario in Fig. 1.1a: A common source signal  $\mathbf{s}$  drives  $M$  different channels with the CIRs  $\mathbf{h}_1, \mathbf{h}_2, \dots, \mathbf{h}_M$ , and we observe samples of convolution outputs  $\mathbf{y}_1, \dots, \mathbf{y}_M$ , where  $\mathbf{y}_m = \mathbf{s} \circledast \mathbf{h}_m + \mathbf{w}_m$ . We further collect  $P$  snapshots of such convolution measurements, and for each snapshot, the channels are time-invariant with the CIRs belonging to the same subspace. The measurements can be written as

$$\mathbf{y}_m(p) = \mathbf{h}_m(p) \circledast \mathbf{s}(p) + \mathbf{w}_m(p), \quad m = 1, \dots, M, \quad (4.1)$$



where the index for snapshots  $p = 1, \dots, P$ , and for all  $p$  and  $m$ ,  $\mathbf{h}_m(p) = \Phi_m \mathbf{u}_m(p)$ . We note here that, throughout this chapter, the subscript  $m$  denotes the  $m$ th channel and  $(p)$  in the parentheses denotes the  $p$ th snapshot.

The essential structural assumption we make is that each CIR snapshot  $\mathbf{h}_m(p)$  ( $m = 1, \dots, M$  and  $p = 1, \dots, P$ ) lies in a common subspace and each source signal  $\mathbf{s}(p)$  is uncorrelated. If we define  $\mathbf{h}(p) = [\mathbf{h}_1(p)^\top, \dots, \mathbf{h}_M(p)^\top]^\top$ , the CIRs in the  $p$ th snapshot can be written as

$$\mathbf{h}(p) = \Phi \mathbf{u}(p), \quad (4.2)$$

where as before

$$\Phi = \begin{bmatrix} \Phi_1 & \mathbf{0} & \dots & \mathbf{0} \\ \mathbf{0} & \Phi_2 & \dots & \mathbf{0} \\ \vdots & \vdots & \ddots & \vdots \\ \mathbf{0} & \mathbf{0} & \dots & \Phi_M \end{bmatrix}, \quad \Phi_m \in \mathbb{R}^{K \times D}.$$

In Section 3.3, we saw that the classical cross-convolution method for multichannel blind deconvolution [1] originated from the idea using the convolution commutivity property. If we rewrite the classical cross-convolution method in our multiple snapshots measurements scenario, we want to solve the following problem in each snapshot to deconvolve  $\mathbf{h}(p)$ :

$$\mathbf{Y}(p) \mathbf{h}(p) = \mathbf{0}. \quad (4.3)$$

The block Toeplitz matrix  $\mathbf{Y}(p)$  for the  $p$ th snapshot is the same as Eq. 3.11. We need to note that there are  $P$  such block Toeplitz matrices and we denote the  $p$ th

matrix corresponding to the  $p$ th snapshot.

$$\mathbf{Y}(p) = \begin{bmatrix} \mathbf{Y}^{(1)}(p) \\ \mathbf{Y}^{(2)}(p) \\ \vdots \\ \mathbf{Y}^{(M-1)}(p) \end{bmatrix}, \quad \mathbf{Y}^{(i)}(p) = \begin{bmatrix} \mathbf{0}_{L,K} & \dots & \mathbf{0}_{L,K} & \mathbf{T}_{\mathbf{y}_{i+1}(p)} & -\mathbf{T}_{\mathbf{y}_i(p)} \\ \vdots & & \vdots & \vdots & \ddots \\ \underbrace{\mathbf{0}_{L,K} \dots \mathbf{0}_{L,K}}_{(i-1) \text{ blocks}} & \underbrace{\mathbf{T}_{\mathbf{y}_M(p)} \dots -\mathbf{T}_{\mathbf{y}_i(p)}}_{(M-i+1) \text{ blocks}} \end{bmatrix}, \quad (4.4)$$

where  $\mathbf{T}_{\mathbf{y}_m(p)}$  is the matrix whose action is convoluting  $\mathbf{y}_m(p)$  with a signal of length  $K$ . We plug in the linear model in Eq. (4.2) so that the problem we want to solve for each snapshot can be written as:

$$\underset{\mathbf{u}(p)}{\text{minimize}} \quad \mathbf{u}(p)^* \mathbf{\Phi}^* \mathbf{Y}(p)^* \mathbf{Y}(p) \mathbf{\Phi} \mathbf{u}(p) \quad \text{subject to} \quad \|\mathbf{u}(p)\|_2 = 1. \quad (4.5)$$

Our objective in this chapter is to learn the subspaces spanned by the columns of the matrices  $\mathbf{\Phi}_m \in \mathbb{R}^{K \times D}$  for  $m = 1, \dots, M$  given  $P$  snapshots of multiple channel outputs  $\{\mathbf{y}_m(p) \mid 1 \leq m \leq M, 1 \leq p \leq P\}$ . In Eq. (4.5), the matrix  $\mathbf{\Phi}_m$  is the  $m$ th diagonal block of the matrix  $\mathbf{\Phi}$ , and  $\mathbf{\Phi}$  is shared for all snapshots.

#### 4.2.1 Optimization over a Grassmannian manifold

The Grassmannian manifold is a space which parametrizes all  $K$ -dimensional linear subspaces of the  $D$ -dimensional vector space. The subspace of the  $m$ th channel, which is spanned by the column vectors of  $\mathbf{\Phi}_m$ , is an element of the Grassmannian manifold  $\text{Grass}(K, D)$ . We formulate the subspace learning problem as an optimization problem over a Grassmannian manifold, jointly using all the snapshots in the objective function. If we solve the problem defined in Eq. (4.5) jointly, we are minimizing the term of  $\sum_{p=1}^P \mathbf{u}(p)^* \mathbf{\Phi}^* \mathbf{Y}(p)^* \mathbf{Y}(p) \mathbf{\Phi} \mathbf{u}(p)$ . Since we require  $\|\mathbf{u}(p)\|_2 = 1$ , the summation term is equivalent to  $\sum_{p=1}^P \lambda_{\min}(\mathbf{\Phi}^* \mathbf{Y}(p)^* \mathbf{Y}(p) \mathbf{\Phi})$ . Therefore, we form the optimization problem by enforcing the shared-subspace channel structure across

snapshots by optimizing over the subspaces denoted by  $\{\mathbf{Q}_m\}_{m=1}^M$ . The optimization problem we want to solve can be written as below:

$$\begin{aligned} & \underset{\{\mathbf{Q}_m\}_{m=1}^M}{\text{minimize}} && \sum_{p=1}^P \lambda_{\min}(\mathbf{Q}^* \mathbf{Y}(p)^* \mathbf{Y}(p) \mathbf{Q}) \\ & \text{subject to} && \mathbf{Q}_m^* \mathbf{Q}_m = \mathbf{I}_D, \quad \forall m = 1, \dots, M, \end{aligned} \tag{4.6}$$

where

$$\mathbf{Q} = \begin{bmatrix} \mathbf{Q}_1 & \mathbf{0} & \dots & \mathbf{0} \\ \mathbf{0} & \mathbf{Q}_2 & \dots & \mathbf{0} \\ \vdots & \vdots & \ddots & \vdots \\ \mathbf{0} & \mathbf{0} & \dots & \mathbf{Q}_M \end{bmatrix}, \quad \mathbf{Q}_m \in \mathbb{R}^{K \times D}.$$

We need to note here that we are only interested in estimating the subspace spanned by columns of  $\mathbf{Q}_m$ . Therefore, the subspace  $\{\mathbf{Q}_m\}_{m=1}^M$  is a collection of  $M$  vector subspaces live on a point of the Grassmannian manifold given as  $\text{Grass}(K, D)^M$ , where  $K$  is the length of each CIR,  $D$  is the dimension of the subspace. In the noiseless case,  $\sum_{p=1}^P \lambda_{\min}(\mathbf{\Phi}^* \mathbf{Y}(p)^* \mathbf{Y}(p) \mathbf{\Phi})$  is zero, and  $\mathbf{\Phi}$  is the solution to (4.6). In the problem formulation (4.6), by minimizing the summation of the least eigenvalues, we are enforcing the cross-convolution method to solve the blind deconvolution problem jointly across all snapshots. Therefore, the solution to (4.6) is the common subspace where the CIRs for all snapshots lie in.

Our method treats this problem as an optimization problem over a Grassmannian manifold, and we adapted a gradient-based method from [92] to solve it. We need to note here that such algorithm is not the only method to solve the problem defined in (4.6), but we use it to demonstrate the efficiency and robustness performance of our subspace learning method.

#### 4.2.2 Subspace learning via low-rank recovery

We also formulate the subspace learning problem via low-rank matrix recovery and introduce another algorithm to solve the problem, which interprets the problem from another perspective. From our linear channel model assumption  $\mathbf{h}_m(p) = \mathbf{\Phi}_m \mathbf{u}_m(p)$ , this also means that a matrix constructed by stacking all  $\mathbf{h}_m(p)$  for a fixed  $m$  as column vectors has rank- $D$  structure. Let's define a matrix  $\mathbf{H} \in \mathbb{R}^{MK \times P}$  and a matrix  $\mathbf{H}_m \in \mathbb{R}^{K \times P}$  as below,

$$\mathbf{H} = \begin{bmatrix} \mathbf{h}_1(1) & \mathbf{h}_1(2) & \dots & \mathbf{h}_1(P) \\ \mathbf{h}_2(1) & \mathbf{h}_2(2) & \dots & \mathbf{h}_2(P) \\ \vdots & \vdots & \ddots & \vdots \\ \mathbf{h}_M(1) & \mathbf{h}_M(2) & \dots & \mathbf{h}_M(P) \end{bmatrix}, \quad \mathbf{h}(p) = \begin{bmatrix} \mathbf{h}_1(p) \\ \mathbf{h}_2(p) \\ \vdots \\ \mathbf{h}_M(p) \end{bmatrix}, \quad (4.7)$$

$$\text{and } \mathbf{H}_m = \begin{bmatrix} \mathbf{h}_m(1), \mathbf{h}_m(2), \dots, \mathbf{h}_m(P) \end{bmatrix}.$$

We estimate  $\mathbf{h}(p)$  for all snapshots jointly using the basic idea of cross-convolution while enforcing the low-rank structure of  $\mathbf{H}_m$ . The subspace that spans all CIRs  $\mathbf{h}_m(p)$  is just a rank- $D$  projection of  $\mathbf{H}_m$  once the following optimization problem is solved:

$$\begin{aligned} & \underset{\{\mathbf{h}(p)\}_{p=1}^P}{\text{minimize}} && \sum_{p=1}^P \mathbf{h}(p)^* \mathbf{Y}(p)^* \mathbf{Y}(p) \mathbf{h}(p) \\ & \text{subject to} && \text{rank}(\mathbf{H}_m) \leq D, \|\mathbf{H}_m\|_F = 1, \quad \forall m = 1, \dots, M, \end{aligned} \quad (4.8)$$

We first briefly discuss the robustness of the above two subspace learning methods. If  $P < D$ , that is the number of snapshot is smaller than the dimension of the subspace, we cannot learn a subspace by solving the optimization problem above. However, if  $P \gg D$ , then the joint optimization is feasible and increases the robustness performance against noise as the number of snapshots increases. In the

cross-convolution method, the concatenation of the true CIRs  $\mathbf{h}(p)$  is obtained as the least dominant eigenvector of  $\mathbf{Y}(p)^*\mathbf{Y}(p)$ . In single snapshot estimation, the gap between two smallest eigenvalues can be tiny, which results in the energy of the CIRs vector “leaking” into other invariant subspaces. Let  $\mathbf{n}(p)$  be an eigenvector of  $\mathbf{Y}(p)^*\mathbf{Y}(p)$  corresponding to the second smallest eigenvalues (different from the smallest eigenvector  $\mathbf{h}(p)$ ). In the  $p$ th snapshot,  $\mathbf{n}(p)^*\mathbf{Y}(p)^*\mathbf{Y}(p)\mathbf{n}(p)$  is equal to the second smallest eigenvalue of  $\mathbf{Y}(p)^*\mathbf{Y}(p)$ , and therefore is very small. However, in the  $p'$  snapshot ( $p' \neq p$ ), because the source  $\mathbf{s}(p')$  and the random noise  $\mathbf{w}_m(p')$  have changed,  $\mathbf{n}(p)$  is no longer the second smallest eigenvector of  $\mathbf{Y}(p')^*\mathbf{Y}(p')$ , and the value of  $\mathbf{n}(p)^*\mathbf{Y}(p')^*\mathbf{Y}(p')\mathbf{n}(p)$  is not necessarily small. Therefore, minimizing the summation in (4.8) and (4.6) can provide a robust estimation of the subspace model. In Section 4.4, we show that the robustness performance of our methods increases as the number of snapshots  $P$  increases.

### 4.3 Optimization Algorithms

We have formulated the subspace learning problem in (4.6) and (4.8) and both formulations require us to solve non-convex problems. For the first formulation in (4.6), we implement a gradient-based algorithm for optimization over the Grassmannian manifold. We present the details of the calculation of the gradient in a later section for implementation. For the second method, we again use a truncated power iteration method.

#### 4.3.1 Optimization over a Grassmannian manifold

Our solver requires inputs of the objective function in (4.6) and the gradient of the objective function in terms of  $\mathbf{Q}_m$ . Let  $f$  denote the objective function as below

$$f(\mathbf{Q}_1, \dots, \mathbf{Q}_M) = \sum_{p=1}^P \lambda_{\min}(\mathbf{Q}^*\mathbf{Y}(p)^*\mathbf{Y}(p)\mathbf{Q}). \quad (4.9)$$

One computational advantage of our formulation with a subspace basis matrix  $\mathbf{Q}$  is that the size of the problem scales with  $MD \times MD$  instead of  $MK \times MK$  for classical cross-convolution method. We implement a fast way of calculating  $\mathbf{Q}^* \mathbf{Y}(p)^* \mathbf{Y}(p) \mathbf{Q}$  using the Fast Fourier Transform. In terms of computational cost, the increase of the number of snapshots  $P$  is just a linear increase of the summation operations of the objective functions and their gradients. This linear scaling makes the calculation scalable to large number of snapshots  $P$ . The cost function is straightforward to calculate, and we present the details of how to calculate the gradient of the objective function as below.

To simplify notations in deriving the gradient, we first denote the  $(m, m')$ th block of matrix  $\mathbf{Y}(p)^* \mathbf{Y}(p)$  to be

$$\mathbf{B}_{m,m'}(p) = (\mathbf{e}_m^* \otimes \mathbf{I}_K) \mathbf{Y}(p)^* \mathbf{Y}(p) (\mathbf{e}_m \otimes \mathbf{I}_K), \quad \mathbf{B}_{m,m'}(p) \in \mathbb{R}^{K \times K}.$$

We remind that  $\mathbf{e}_m$  is a standard basis vector and  $\otimes$  denotes the Kronecker product, which is first explained in Eq. (3.6). Let  $\boldsymbol{\xi}(p) \in \mathbb{R}^{MD \times 1}$  be the eigenvector of  $\mathbf{Q}^* \mathbf{Y}(p)^* \mathbf{Y}(p) \mathbf{Q}$  corresponding to the smallest eigenvalue. We assume that the multiplicity of the smallest eigenvalue is 1, which is generally the case. Otherwise the expression of the partial derivative becomes more complicated. The derivative of the smallest eigenvalues of a matrix has been derived by Overton et al [93]. The partial derivatives of the eigenvalue with respect to the  $(i, j)$ th element of the matrix  $\mathbf{Q}_m$  can be written as:

$$\frac{\partial \lambda_{\min}(\mathbf{Q}^* \mathbf{Y}(p)^* \mathbf{Y}(p) \mathbf{Q})}{\partial (\mathbf{Q}_m)_{ij}} = \left\langle \boldsymbol{\xi}(p) \boldsymbol{\xi}(p)^*, \frac{\partial \mathbf{Q}^* \mathbf{Y}(p)^* \mathbf{Y}(p) \mathbf{Q}}{\partial (\mathbf{Q}_m)_{ij}} \right\rangle.$$

We can then write the gradient in terms of the matrix  $\mathbf{Q}_m$  as

$$\begin{aligned} \frac{\partial \lambda_{\min}(\mathbf{Q}^* \mathbf{Y}(p)^* \mathbf{Y}(p) \mathbf{Q})}{\partial \mathbf{Q}_m} &= 2 \mathbf{B}_{m,m}(p) \mathbf{Q}_m (\mathbf{e}_m^* \otimes \mathbf{I}_D) \boldsymbol{\xi}(p) \boldsymbol{\xi}(p)^* (\mathbf{e}_m \otimes \mathbf{I}_D) \\ &\quad + 2 \sum_{\substack{m'=1 \\ m' \neq m}}^M \mathbf{B}_{m,m'}(p) \mathbf{Q}_{m'} (\mathbf{e}_{m'}^* \otimes \mathbf{I}_D) \boldsymbol{\xi}(p) \boldsymbol{\xi}(p)^* (\mathbf{e}_m \otimes \mathbf{I}_D). \end{aligned}$$

Then the gradient of the objective function  $f$  with respect to  $\mathbf{Q}_m$  in the geodesic distance in the Grassmannian manifold is written as

$$\begin{aligned} (\text{grad} f(\mathbf{Q}_1, \dots, \mathbf{Q}_M))_{\mathbf{Q}_m} &= \left( \text{grad} \sum_{p=1}^P \lambda_{\min}(\mathbf{Q}^* \mathbf{Y}(p)^* \mathbf{Y}(p) \mathbf{Q}) \right)_{\mathbf{Q}_m} \\ &= 2 \sum_{p=1}^P (\mathbf{I}_K - \mathbf{Q}_m \mathbf{Q}_m^*) \mathbf{B}_{m,m}(p) \mathbf{Q}_m (\mathbf{e}_m^* \otimes \mathbf{I}_D) \boldsymbol{\xi}(p) \boldsymbol{\xi}(p)^* (\mathbf{e}_m \otimes \mathbf{I}_D) \\ &\quad + 2 \sum_{p=1}^P \sum_{\substack{m'=1 \\ m' \neq m}}^M (\mathbf{I}_K - \mathbf{Q}_m \mathbf{Q}_m^*) \mathbf{B}_{m,m'}(p) \mathbf{Q}_{m'} (\mathbf{e}_{m'}^* \otimes \mathbf{I}_D) \boldsymbol{\xi}(p) \boldsymbol{\xi}(p)^* (\mathbf{e}_m \otimes \mathbf{I}_D). \end{aligned}$$

With the objective function and gradient of the objective function calculated, we then use a trust-region method because the standard gradient decent method is slow in convergence and the Newton's method does not distinguish all critical points that are asymptotically stable. Trust-region methods form an alternative class of algorithms that combine desirable global convergence properties with a local superlinear rate of convergence. More details of the trust-region methods on the Grassmannian manifold can be found at the monograph by Absil et al. [92]. In our simulation, we use a standard Matlab toolbox Manopt [94] to implement the trust-region method and we only need to provide the objective function and its gradient as inputs.

#### 4.3.2 Subspace learning via low-rank recovery

In order to solve the problem in (4.8), we want to solve multiple snapshots of blind deconvolution jointly with a low-rank structural constraint. We implement an iter-

ative method to enforce the low-rank constraint and solve the blind deconvolution problem by finding the smallest eigenvector of  $\mathbf{A}$ . We first define  $\mathbf{A} = \mathbf{\Gamma}^* \mathbf{\Gamma}$  in this multiple snapshots case, where  $\mathbf{\Gamma}$  is defined as

$$\mathbf{\Gamma} = \begin{bmatrix} \mathbf{Y}(1) & \mathbf{0} & \dots & \mathbf{0} \\ \mathbf{0} & \mathbf{Y}(2) & \dots & \mathbf{0} \\ \vdots & \vdots & \ddots & \vdots \\ \mathbf{0} & \mathbf{0} & \dots & \mathbf{Y}(P) \end{bmatrix}, \quad \mathbf{Y}(p) \in \mathbb{R}^{MK \times MK}$$

A standard tool from numerical linear algebra to compute the largest eigenvector of a symmetric matrix is the *power method*. Similarly as we explained in Section 3.4.2, we define  $\mathbf{B} = \gamma \mathbf{I}_{MKP} - \mathbf{A}$ , and  $\gamma = \|\mathbf{A}\|$ . Applying a standard power method on matrix  $\mathbf{B}$  to find the largest eigenvector of  $\mathbf{B}$  is equivalent to find the smallest eigenvector of  $\mathbf{A}$ .

We summarize the subspace learning low-rank recovery method in Algorithm 4

---

**Algorithm 4:** Subspace learning via low-rank recovery

---

**input :**  $\mathbf{B}$ ,  $\mathbf{v}_0$   
**output:**  $\mathbf{v}_t$ , a vectorized block-wise rank- $D$  matrix  $\mathbf{H}$

```

1  $t \leftarrow 1$ ;
2 while stop condition not satisfied do
3    $\tilde{\mathbf{v}}_t \leftarrow \mathbf{B} \mathbf{v}_{t-1}$ ;
4    $\hat{\mathbf{V}}_t \leftarrow \text{BlockRankDApprox}(\text{mat}(\tilde{\mathbf{v}}_t))$ ;
5    $\mathbf{v}_t \leftarrow \text{vec}(\hat{\mathbf{V}}_t) / \|\text{vec}(\hat{\mathbf{V}}_t)\|_2$ ;
6    $t \leftarrow t + 1$ ;
7 end
```

---

We note here that the BlockRankDApprox operation in Algorithm 4 means that we take the vector  $\tilde{\mathbf{v}}$  and arrange it to the matrix  $\tilde{\mathbf{V}} \in \mathbb{R}^{MK \times P}$  as  $\mathbf{H}$  we have defined in Eq. (4.7). We then perform a rank- $D$  approximation on the submatrix  $\tilde{\mathbf{V}}_m \in \mathbb{R}^{K \times P}$ , where  $\tilde{\mathbf{V}}_m$  is the  $m$ th row block of  $\tilde{\mathbf{V}}$ . After  $M$  rank- $D$  approximations on  $M$  submatrices, we generate the matrix  $\hat{\mathbf{V}}$ .



## 4.4 Numeric Results

In this section, our subspace learning methods are implemented and the effectiveness and robustness of the algorithms are demonstrated for generic and stylized realistic CIRs. In simulations, the common driving source signal,  $\mathbf{s}(p) \in \mathbb{R}^L$ , is a Gaussian white noise signal, which differs for each snapshot.

### 4.4.1 Generic channels

In this section, the two subspace learning methods are implemented with additive noise measurements in simulated generic channels. Since our methods are based on the classical cross-convolution method, the deconvolution of CIRs using the classical method for each snapshots will be exact in the noise-free measurements when the length of measurements  $L$  is bigger than the channel length  $K$ . In order to compare the performance of subspace learning method with the single snapshot blind deconvolution method, we compare the average SNR for the estimated CIRs for all snapshots. We corrupted all measurements with 20dB SNR noise level. Even though these generic CIR assumptions do not directly represent any specific underwater acoustic channels, we can demonstrate the efficiency of our method and simulations on underwater acoustic channels will be discussed later in this section.

We first compare the classical cross-convolution method with our subspace learning method for solving blind deconvolution estimation. In our simulation, we assume the number of channels  $M = 5$ , the length of channels  $K = 64$ , the dimension of the subspace  $D = 5$ , the length of measurements  $L = 80$ , the number of snapshots  $P = 50$ , and the measurement error SNR = 10 dB. A classical cross-convolution method is performed on all snapshots individually. Figure 4.1a shows that the estimation is a failure for each snapshots. Figure 4.1b shows that if we use subspace learning method in (4.6), the estimation is accurate. In this simulation, we initialize

our starting point for  $\mathbf{Q}_m$  by collecting the eigenvectors of  $\sum_{p=1}^P \mathbf{B}_{m,m}(p)$  corresponding to the  $D$ -smallest eigenvalues, where  $\mathbf{B}_{m,m}(p) = (\mathbf{e}_m^\top \otimes \mathbf{I}_K) \mathbf{Y}(p)^\top \mathbf{Y}(p) (\mathbf{e}_m \otimes \mathbf{I}_K)$ .

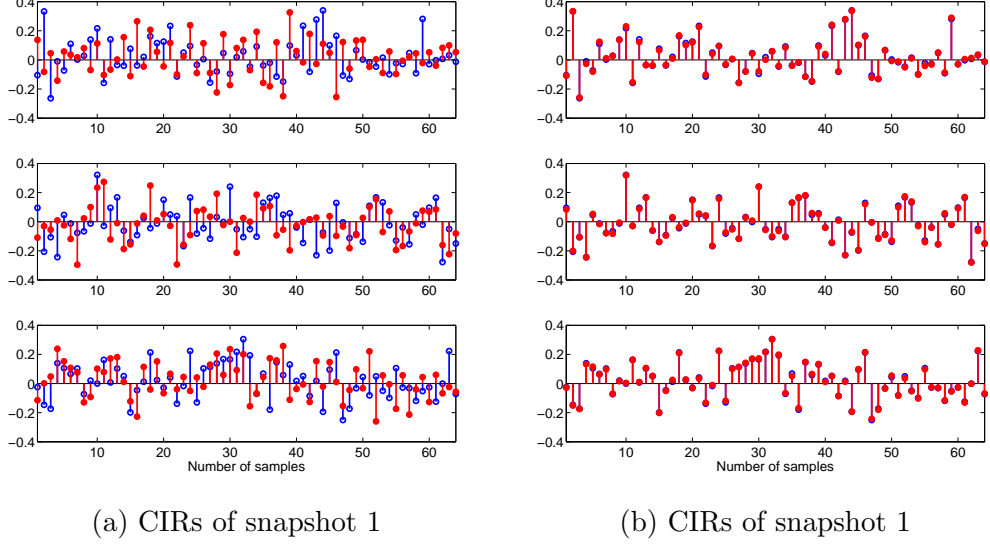


Figure 4.1: (a) Estimated CIRs from the cross-convolution method by solving each snapshot separately. Blue stems are elements of the original CIRs, and the red stems are the estimation samples. The estimation SNR  $\approx 1$  dB (b) Estimated CIRs from subspace learning method. Blue stems are elements of the original CIRs, and the red stems are the estimation samples. The estimation is accurate with a SNR  $\approx 30$  dB.

In order to compare the robustness performance, we design two simulations and assume the number of channels  $M = 3$ , the length of channels  $K = 64$ , the dimension of the subspace  $D = 5$  and the number of snapshots  $P = 50$ . We vary the length of the measurement  $L$  from  $K$  to  $3K$ . For the classical blind deconvolution method, which solves each snapshots independently, Fig. 4.2a shows that when the measurement length  $L$  is relatively short and the classical method is not stable when the measurement noise level is at 20 dB. However, our subspace learning method estimates the CIRs accurately from an initialization of 10 dB SNR.

In Fig. 4.2b, we set the length of the measurements to  $L = 128$ , vary the number of snapshots  $P$  from 10 to 50, and the rest of parameters are the same. We can see that for classical method adding more snapshots does not affect the overall recovery accuracy. However, through subspace learning methods, we can observe a noticeable

decrease of estimation error as  $P$  gets larger.

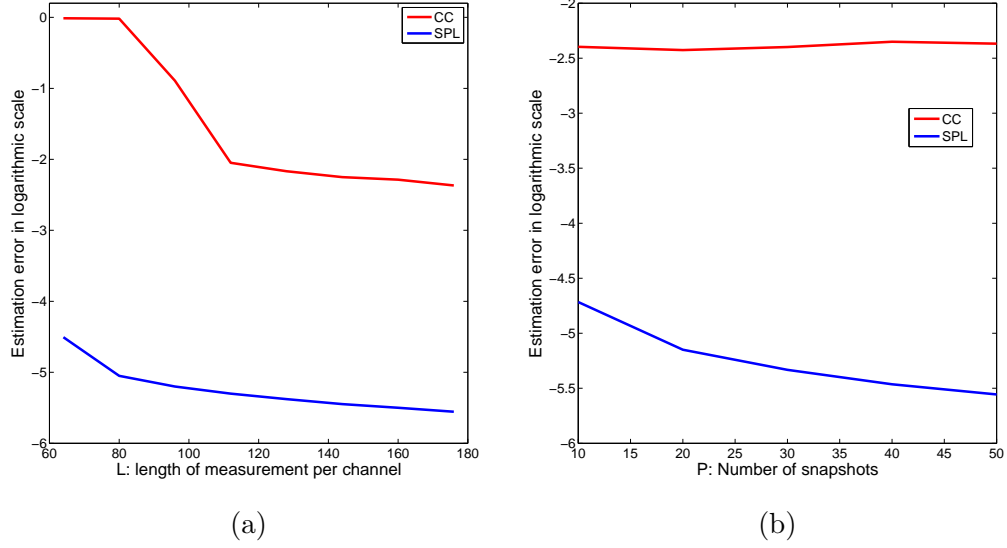


Figure 4.2: Comparison of average CIRs estimation error between the classical cross-convolution method (red line) and the subspace learning method (blue line). (a) The number of snapshots for each method is  $P = 50$  and the length of measurements  $L$  from  $K$  to  $3K$ .  $x$ -axis: the length of measurement length  $L$ ,  $y$ -axis: log of the estimation error when the measurements  $\text{SNR} = 20$  dB. (b) The length of measurements  $L = 128$  and the number of snapshots for each method  $P$  varies from 10 to 50.  $x$ -axis: the number of snapshots  $P$ ,  $y$ -axis: log of the estimation error when the measurements  $\text{SNR} = 20$  dB.

We also perform a Monte Carlo simulation with 100 trials to demonstrate how stable the method performs as the number of snapshots  $P$  and the length of measurement  $L$  vary.

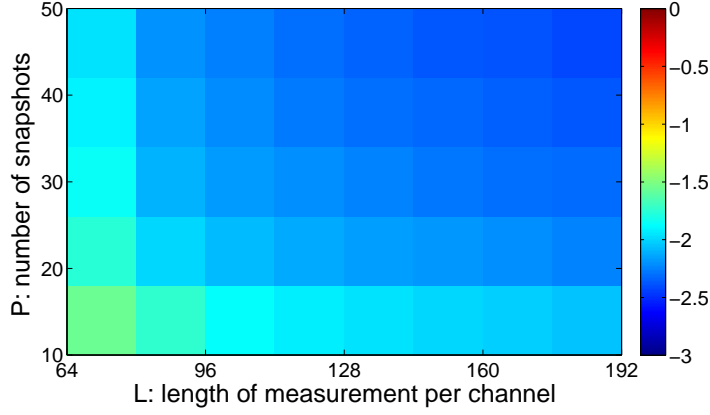


Figure 4.3: *Phase transition in estimation error for the subspace learning method from Monte Carlo simulation. x-axis:  $P$ : the length of measurement, y-axis:  $P$ : number of snapshots.*

Figure 4.3 shows that for a fixed length of measurements, as we make more snapshots of measurements, we have more diverse indirect sensing samples of the channel subspace, and therefore the estimation of subspace and CIRs of each snapshot is more accurate.

#### 4.4.2 Acoustic channels

In this section, we implement our method on stylized acoustic channels which correspond to single path CIRs on a vertical line array. In the simulation, we assume a scenario that an accurate estimation of the channel model is not available, so the multichannel blind deconvolution methods we have discussed in previous chapters cannot provide us an accurate estimation of the CIRs. However, we are presented with multiple snapshots of the measurements. We show that using the subspace learning method we can learn a more accurate subspace of the CIRs and deconvolve the CIRs accurately.

In the simulation of Fig. 4.4, we assume the number of channels  $M = 5$ , the length of channels  $K = 64$ , the length of measurements  $L = 200$ , and the number of snapshots  $P = 50$ . We assume that the pulses of CIRs are band-limited in  $(400 - 600)$

Hz and concentrated in a time window, and the width of the arrival-time uncertainty window is  $20t_s$ , where  $t_s$  is the sampling time. Using the discrete prolate spheroidal (slepian) sequences, we can form an subspace basis matrix  $\hat{\Phi}_m \in \mathbb{R}^{K \times D}$  to approximate the  $m$ th CIRs roughly. Let us further assume the dimension of the subspace  $D$  is 12.

The problems we formed in (4.6) and (4.8) are non-convex, so we need to have a starting point within a small neighborhood to the true solution. Let's denote the true subspace matrix is  $\Phi$  for all CIRs and  $\Phi_m$  for the  $m$ th CIRs as in (4.2). The distance between  $\Phi$  and  $\hat{\Phi}$  is defined as  $d = \sum_{m=1}^M \|\Phi_m \Phi_m^* - \hat{\Phi}_m \hat{\Phi}_m^*\|_F / D / M$ . In this simulation, the distance between the true subspace basis and our rough estimation  $\hat{\Phi}$  is  $d = 0.1064$ , which empirically can reach the global minimum. If we project the true CIRs  $\mathbf{h}(p)$  onto  $\hat{\Phi}$ , we actually have a good approximation of  $\mathbf{h}(p)$  with an approximation SNR  $\approx 25$  dB.

We now compare the CIR estimation results from the blind deconvolution method using linear model  $\hat{\Phi}$  and from the subspace learning method using linear model  $\hat{\Phi}$  as an initialization for the subspace learning. The measurements for all snapshots are corrupted with noise at a level SNR = 30 dB. The single snapshot multichannel blind deconvolution using the linear channel model  $\hat{\Phi}$  didn't provide a stable performance, and the estimations of the CIRs are not successful as shown in Fig. 4.4a. We define the estimation error as

$$e = \sqrt{\frac{1}{MP} \sum_{m,p=1}^{M,P} \left\| \frac{\mathbf{h}_m(p) \mathbf{h}_m(p)^*}{\|\mathbf{h}_m(p)\|^2} - \frac{\hat{\mathbf{h}}_m(p) \hat{\mathbf{h}}_m(p)^*}{\|\hat{\mathbf{h}}_m(p)\|^2} \right\|_F^2}.$$

The estimation error of CIRs for all snapshots using linear model  $\hat{\Phi}$  is  $e_{sccc} = 0.7054$  or SNR  $\approx 3$  dB.

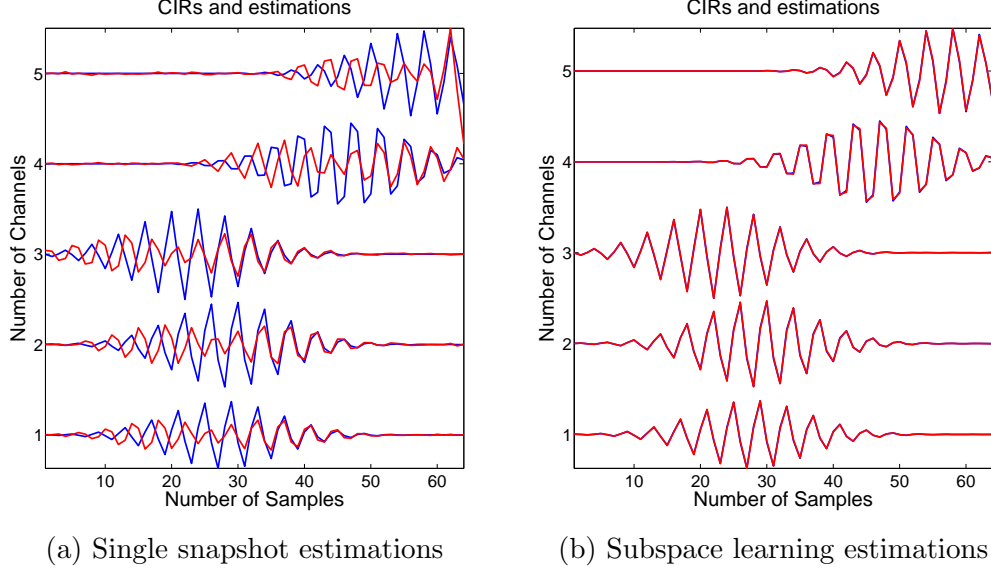


Figure 4.4: (a) The estimations of CIRs (red) using the multichannel blind method from single snapshot with an inaccurate subspace model. The estimation SNR  $\approx 3$  dB. (b) Estimated CIRs (red) from subspace learning method. The starting point are the same inaccurate subspace estimations we used in from Fig. 4.4a. The estimation is accurate with a SNR  $\approx 28$  dB.

In contrast, using the linear model  $\hat{\Phi}$  as a starting point for our subspace learning method in (4.6), we actually can exactly recover the CIRs for all snapshots. The distance between the estimated subspace  $\tilde{\Phi}$  and the true subspace  $\Phi$  is  $d = 0.03220$ . The estimation error of CIRs for all snapshots using the learned subspace  $\tilde{\Phi}$  is  $e_{spl} = 0.005850$  or SNR  $\approx 28$  dB which is much smaller than  $e_1$ . The estimation results are plotted in Fig. 4.4b, which match exactly as the original CIRs plotted in blue.

#### 4.5 Conclusion and Future Work

We investigated two methods to learn the subspace model for CIRs from indirect measurements given as multiple snapshots in the context of solving multichannel blind deconvolution. We proposed two algorithms to solve this subspace learning problem. We first formed the subspace learning problem as an optimization problem over a Grassmannian manifold, which can be solved using a gradient-based method. The second problem formulation stated that the subspace learning problem could be solved

via a low-rank matrix recovery. Two algorithms solved the problem by optimization over the Grassmannian manifold and low-rank matrix recovery respectively. Numeric results of our methods were presented both for generic and under water acoustic channel models. We demonstrated that the subspace learning methods are robust in the presence of noise and can accurately estimate the CIRs by using multiple snapshots jointly when single-snapshot methods failed. Performance guarantees of the methods will be further investigated in future work.

## CHAPTER 5

### CONCLUSIONS

The multichannel sensing framework arises in many applications such as digital communication, medical imaging, ocean tomography and acoustic imaging. The multichannel deconvolution problem wants to estimate both unknown input signals and channel impulse responses from observations of their convolution. This thesis addresses this ubiquitous inverse problem using sources of opportunity in underwater acoustic channels.

We first introduced a method for solving this multichannel deconvolution problem using a priori information about the CIR via the low-rank recovery formulation. We developed a systematic way to build an efficient and accurate linear model incorporating a priori information about the structure of expected CIR's arrival-times so that the low-rank recovery method can be implemented. An fast and scalable heuristic solver was developed, which can work with large-scale problems with efficient usage of memory during computation. Stylized numerical simulations demonstrated that the proposed method perfectly deconvolved both the source signal and CIRs simultaneously. In the presence of additive measurement noises and model errors in the CIR parameterization, the method was also robust and stable. The effectiveness of the method was demonstrated both numerically and experimentally for estimating multipath CIRs in shallow water using shipping noise and short bottom-mounted VLAs. This method is likely to be applicable to other environments supporting waveguide-like propagation (e.g., seismic or structural waveguides).

A blind source separation technique was developed in the multiple-input-multiple-output (MIMO) system. A multichannel deconvolution step based on low-rank re-



covery and a linear source separation step was performed to separate multiple sources from their convolutive mixing measurements.

Two non-convex iterative algorithms and their performances for the multichannel blind deconvolution problem were also studied theoretically and demonstrated numerically. A bilinear model, which is obtained by embedding a parametric model for the shapes of pulse *jointly* into a low-dimensional subspace through manifold embedding while the channel gains are treated as independent variables, was presented. The bilinear system model imposed a strong prior on the unknown channel impulse responses, which enabled us to recover the system more robustly. Performance guarantees of our methods were analyzed and demonstrated when low-dimensional subspace was generic and a series of numerical results demonstrated that the empirical performance was consistent with the presented theories. Our methods were also validated by series of experimentally derived simulations. Subspace learning methods that can estimate the channel models directly from multiple snapshots of the convolutive measurements were presented in the end.

# Appendices

## APPENDIX A

### PROOF OF THE MAIN RESULTS

The main results in Theorems 3.5.1 and 3.5.2 are obtained by the following proposition, the proof of which is deferred to Section A.1.

**Proposition A.0.1.** *Suppose the assumptions in (A1) and (A2) hold,  $\rho_x$  satisfies (3.30),  $L \geq 3K$ ,  $\mu = O(1)$ , and  $\nu = \Omega(1)$ . For any  $\beta \in \mathbb{N}$ , there exist absolute constants  $C > 0, \alpha \in \mathbb{N}$  and constants  $C_1, C_2$  that only depend on  $\beta$ , for which the following holds: If*

$$K \geq C_1 D \log^\alpha(MKL), \quad (\text{A.1})$$

$$M \geq C_1 \log^\alpha(MKL), \quad (\text{A.2})$$

and

$$L \geq C_1 \log^\alpha(MKL) \left[ \frac{\rho_{x,w}^2}{\eta K \sigma_w^2 \|\mathbf{x}\|_2^2} \left( \frac{D}{K \wedge M} + \frac{K}{M^2} + 1 \right) + \frac{D}{\eta^2} \right] \quad (\text{A.3})$$

then

$$\sin \angle(\underline{\mathbf{h}}_t, \underline{\mathbf{h}}) \leq 2^{-t} \sin \angle(\underline{\mathbf{h}}_0, \underline{\mathbf{h}}) + \kappa, \quad \forall t \in \mathbb{N} \quad (\text{A.4})$$

with probability  $1 - CK^{-\beta}$ , where  $\kappa$  satisfies (A.13).

Then the proofs for Theorems 3.5.1 and 3.5.2 are given by combining Proposition A.0.1 with the following lemmas, taken from [83], which provide tail estimates on the signal autocorrelation and the signal-noise cross correlation.

**Lemma A.0.2** ([83, Lemma 3.9]). *Suppose (A2) holds and let  $\mathbf{x}$  be a fixed sequence of numbers obeying (3.30). For any  $\beta \in \mathbb{N}$ , there exists an absolute constant  $C$  such*

that

$$\rho_{x,w} \leq CK\sigma_w\sqrt{\rho_x}\sqrt{1 + \log M + \beta \log K}$$

holds with probability  $1 - K^{-\beta}$ .

**Lemma A.0.3** ([83, Lemma 3.10]). *Suppose (A2) holds and let  $\mathbf{x}$  be a sequence of zero-mean iid subgaussian random variables with variance  $\sigma_x^2$ . Then*

$$\frac{\rho_x}{\|\mathbf{x}\|_2^2} \leq \frac{L + C_\beta K \log^{3/2} L \sqrt{\log K}}{L - \sqrt{2L\beta \log K}}$$

and

$$\frac{\rho_{x,w}}{\sigma_w \|\mathbf{x}\|_2} \leq \frac{C_\beta K \log^5(MKL)}{\sqrt{L - \sqrt{2L\beta \log K}}}$$

hold with probability  $1 - 3K^{-\beta}$ .

## A.1 Proof of Proposition A.0.1

The proof of Proposition A.0.1 is given by a set of propositions, which provide guarantees for Algorithms 3, Algorithms 1 and Algorithm 2. The first proposition provides a performance guarantee for the initialization by Algorithm 3. The proof of Proposition A.1.1 is given in Section B.

**Proposition A.1.1** (Initialization). *Suppose the assumptions in (A1) and (A2) hold,  $\rho_x$  satisfies (3.30), and  $L \geq 3K$ . Let  $\mu, \nu, \eta$  be defined in (3.23), (3.24), (3.22), respectively. For any  $\beta \in \mathbb{N}$ , there exist absolute constants  $C > 0, \alpha \in \mathbb{N}$  and constants  $C_1, C_2$  that only depend on  $\beta$ , for which the following holds: If*

$$M \geq C_1 \log^\alpha(MKL) \cdot \left(\frac{\mu}{\nu}\right)^2 \tag{A.5}$$

and

$$L \geq C_1 \log^\alpha(MKL) \cdot \left[ \frac{\rho_{x,w}^2}{\eta K \sigma_w^2 \|\mathbf{x}\|_2^2} \cdot \left( \frac{\mu^2 K}{\nu^4 M^2} + \frac{D}{\nu^2 M} \right) + \frac{D}{\eta^2 \nu^4 M} \right], \quad (\text{A.6})$$

then the estimate  $\hat{\mathbf{b}}$  by Algorithm 3 satisfies

$$\sin \angle(\hat{\mathbf{b}}, \mathbf{b}) \leq C_2 \log^\alpha(MKL) \left[ \frac{\mu}{\nu \sqrt{M}} + \frac{\rho_{x,w}}{\sqrt{\eta K L \sigma_w} \|\mathbf{x}\|_2} \cdot \left( \frac{\mu \sqrt{K}}{\nu^2 M} + \frac{\sqrt{D}}{\nu \sqrt{M}} \right) + \frac{\sqrt{D}}{\eta \nu^2 \sqrt{ML}} \right] \quad (\text{A.7})$$

holds with probability  $1 - CK^{-\beta}$ .

The second proposition, proved in Section C.1.2, provides a performance guarantee for the update of  $\hat{\mathbf{a}}$  by Step 3 of Algorithm 1.

**Proposition A.1.2** (Update of Channel Gains). *Suppose the assumptions in (A1) and (A2) hold,  $\rho_x$  satisfies (3.30),  $L \geq 3K$ , and the previous estimate  $\hat{\mathbf{b}}$  satisfies*

$$\angle(\mathbf{b}, \hat{\mathbf{b}}) \leq \frac{\pi}{4}. \quad (\text{A.8})$$

For any  $\beta \in \mathbb{N}$ , there exist absolute constants  $C > 0, \alpha \in \mathbb{N}$  and constants  $C_1, C_2$  that only depend on  $\beta$ , for which the following holds: If

$$K \geq C_1 \mu^4 D \log^\alpha(MKL), \quad (\text{A.9})$$

$$M \geq C_1 \mu^4 \log^\alpha(MKL), \quad (\text{A.10})$$

and

$$L \geq C_1 \log^\alpha(MKL) \left[ \frac{\rho_{x,w}^2}{\eta K \sigma_w^2 \|\mathbf{x}\|_2^2} \left( \mu^2 \left( \frac{D}{K \wedge M} + \frac{K}{M^2} \right) + 1 \right) + \frac{D}{\eta^2} \right] \quad (\text{A.11})$$

then the updated  $\widehat{\mathbf{a}}$  by Step 3 of Algorithm 1 satisfies

$$\sin \angle(\mathbf{a}, \widehat{\mathbf{a}}) \leq \frac{1}{2} \sin \angle(\mathbf{b}, \widehat{\mathbf{b}}) + \kappa \quad (\text{A.12})$$

with probability  $1 - CK^{-\beta}$ , where  $\kappa$  satisfies

$$\kappa \leq C_2 \log^\alpha(MKL) \left[ \frac{\rho_{x,w}}{\sqrt{\eta KL} \sigma_w \|\mathbf{x}\|_2} \left( \mu \left( \frac{\sqrt{K}}{M} + \sqrt{\frac{D}{M}} + \sqrt{\frac{D}{K}} \right) + 1 \right) + \frac{\sqrt{D}}{\eta \sqrt{ML}} \right]. \quad (\text{A.13})$$

We have a similar result for the update of  $\widehat{\mathbf{b}}$  by Step 3 of Algorithm 1, which is stated in the following proposition. The proof of Proposition A.1.3 is provided in Section C.1.3.

**Proposition A.1.3** (Update of Subspace Coefficients). *Suppose the assumptions in (A1) and (A2) hold,  $\rho_x$  satisfies (3.30),  $L \geq 3K$ , and the previous estimate  $\widehat{\mathbf{a}}$  satisfies*

$$\angle(\mathbf{a}, \widehat{\mathbf{a}}) \leq \frac{\pi}{4}. \quad (\text{A.14})$$

*For any  $\beta \in \mathbb{N}$ , there exist absolute constants  $C > 0, \alpha \in \mathbb{N}$  and constants  $C_1, C_2$  that depend on  $\beta$ , for which the following holds: If (A.9), (A.10), and (A.11) are satisfied, then the updated  $\widehat{\mathbf{b}}$  by Step 3 of Algorithm 1 satisfies*

$$\sin \angle(\mathbf{b}, \widehat{\mathbf{b}}) \leq \frac{1}{2} \sin \angle(\mathbf{a}, \widehat{\mathbf{a}}) + \kappa$$

*with probability  $1 - CK^{-\beta}$ , where  $\kappa$  satisfies (A.13).*

The next proposition shows the convergence of the rank-1 truncated power method from a good initialization. See Section C.2 for the proof.

**Proposition A.1.4** (Local Convergence of Rank-1 Truncated Power Method). *Suppose the assumptions in (A1) and (A2) hold,  $\rho_x$  satisfies (3.30), and  $L \geq 3K$ . Let*

$0 < \mu < 1$ ,  $0 < \tau < \frac{1}{3\sqrt{2}}$ , and

$$c(\mu, \tau) = \min \left( \frac{1}{\mu\sqrt{1-\tau^2}}, \frac{(1+\mu)\tau}{1-\mu} \right).$$

For any  $\beta \in \mathbb{N}$ , there exist absolute constants  $C > 0, \alpha \in \mathbb{N}$ , constants  $C'_1, C'_2$  that only depend on  $\beta$ , for which the following holds: If (A.9), (A.10), and (A.11) are satisfied for  $C_1 = c(\mu, \tau)C'_1, C_2 = c(\mu, \tau)C'_2$  and  $\mathbf{u}_0$  satisfies

$$\sin \angle(\mathbf{u}_0, \mathbf{u}) \leq \tau,$$

then  $(\mathbf{u}_t)_{t \in \mathbb{N}}$  by Algorithm 2 for  $\mathbf{B} = \|\mathbb{E}[\mathbf{A}]\|\mathbf{I}_{MD} - \mathbf{A}$  with  $\mathbf{u}_0$  satisfies

$$\sin \angle(\mathbf{u}_t, \mathbf{u}) \leq \mu^t \sin \angle(\mathbf{u}_0, \mathbf{u}) + \frac{(1+\mu)\kappa}{1-\mu}, \quad \forall t \in \mathbb{N} \quad (\text{A.15})$$

with probability  $1 - CK^{-\beta}$ , where  $\kappa$  satisfies (A.13).

Finally, we derive the proof of Proposition A.0.1 by combining the above propositions.

*Proof of Proposition A.0.1.* Similarly to the proof of [83, Proposition 3.3], we show that

$$\sin \angle(\underline{\mathbf{h}}_t, \underline{\mathbf{h}}) \leq \frac{\sigma_{\max}(\underline{\Phi})}{\sigma_{\min}(\underline{\Phi})} \cdot \sqrt{2} \sin \angle(\mathbf{u}_t, \mathbf{u}) \quad (\text{A.16})$$

and

$$\sin \angle(\mathbf{u}_t, \mathbf{u}) \leq \max \left[ \sin \angle(\mathbf{a}_t, \mathbf{a}), \sin \angle(\mathbf{b}_t, \mathbf{b}) \right]. \quad (\text{A.17})$$

Furthermore, as we choose  $C_1$  in (A.1) sufficiently large, we can upper bound the condition number of  $\underline{\Phi}$  by a constant (e.g., 3) with high probability. We proceed the proof under this event. Then the convergence results in Propositions A.1.2, A.1.3, and A.1.4 imply (A.4).

Since  $\mu = O(1)$ , the conditions in (A.9), (A.10), (A.11) respectively reduce (A.1),

(A.2), (A.3). Furthermore, since  $\nu = \Omega(1)$ , (A.6) is implied by (A.3). By choosing  $C_1$  large enough, we can make the initial error bound in (A.7) small so that the conditions for previous estimates in Propositions A.1.2, A.1.3, A.1.4 are satisfied and the assertion is obtained by these propositions.  $\square$



## APPENDIX B

### ANALYSIS OF SPECTRAL INITIALIZATION

We prove Proposition A.1.1 in this section. Recall that Algorithm 3 computes an initial estimate  $\hat{\mathbf{b}}$  of the true parameter vector  $\mathbf{b}$  as an eigenvector of  $\mathbf{\Gamma}\mathbf{\Gamma}^* - \sum_{m=1}^M \sigma_w^2 L \mathbf{\Phi}_m^* \mathbf{\Phi}_m$  corresponding to the largest eigenvalue in magnitude. Let us decompose the matrix  $\mathbf{\Gamma}$  in (3.18) as  $\mathbf{\Gamma} = \mathbf{\Gamma}_s + \mathbf{\Gamma}_n$ , where  $\mathbf{\Gamma}_s$  and  $\mathbf{\Gamma}_n$  respectively correspond to the noise-free portion and noise portion of  $\mathbf{\Gamma}$ . In other words,  $\mathbf{\Gamma}_s$  is obtained as we replace  $\mathbf{y}_m = \mathbf{h}_m \otimes \mathbf{x} + \mathbf{w}_m$  in the expression of  $\mathbf{\Gamma}$  in (3.19) by its first summand  $\mathbf{h}_m \otimes \mathbf{x}$ . Similarly,  $\mathbf{\Gamma}_n$  is obtained as we replace  $\mathbf{y}_m$  by  $\mathbf{w}_m$ . Then it follows that

$$\mathbb{E}_w[\mathbf{\Gamma}_n \mathbf{\Gamma}_n^*] = \sum_{m=1}^M \sigma_w^2 L \mathbf{\Phi}_m^* \mathbf{\Phi}_m.$$

By direct calculation, we obtain that the expectation of  $\mathbf{\Gamma}_s$  is written as

$$\mathbb{E}[\mathbf{\Gamma}_s] = \sum_{m=1}^M K a_m \mathbf{b} \mathbf{x}^\top = K \|\mathbf{a}\|_1 \mathbf{b} \mathbf{x}^\top. \quad (\text{B.1})$$

Therefore,

$$\mathbb{E}[\mathbf{\Gamma}_s] \mathbb{E}[\mathbf{\Gamma}_s]^* = K^2 \|\mathbf{x}\|_2^2 \|\mathbf{a}\|_1^2 \mathbf{b} \mathbf{b}^*. \quad (\text{B.2})$$

It is straightforward to check that the rank-1 matrix  $\mathbb{E}[\mathbf{\Gamma}_s] \mathbb{E}[\mathbf{\Gamma}_s]^*$  has an eigenvector, which is collinear with  $\mathbf{b}$ . Thus as we interpret  $\mathbf{\Gamma}\mathbf{\Gamma}^* - \sum_{m=1}^M \sigma_w^2 L \mathbf{\Phi}_m^* \mathbf{\Phi}_m$  as a perturbed version of  $\mathbb{E}[\mathbf{\Gamma}_s] \mathbb{E}[\mathbf{\Gamma}_s]^*$ , the error in  $\hat{\mathbf{b}}$  is upper bounded by the classical result in linear algebra known as the Davis-Kahan theorem [95]. Among numerous variations of the original Davis-Kahan theorem available in the literature, we will use a consequence of a particular version [96, Theorem 8.1.12], which is stated as the following lemma.

**Lemma B.0.1** (A Special Case of the Davis-Kahan Theorem). *Let  $\mathbf{M}, \underline{\mathbf{M}} \in \mathbb{C}^{n \times n}$  be symmetric matrices and  $\lambda$  denote the largest eigenvalue of  $\underline{\mathbf{M}}$  in magnitude. Suppose that  $\lambda > 0$  and has multiplicity 1. Let  $\mathbf{Q} = [\mathbf{q}_1, \mathbf{Q}_2] \in \mathbb{C}^{n \times n}$  be a unitary matrix such that  $\mathbf{q}_1$  is an eigenvector of  $\underline{\mathbf{M}}$  corresponding to  $\lambda$ . Partition the matrix  $\mathbf{Q}^* \underline{\mathbf{M}} \mathbf{Q}$  as follows:*

$$\mathbf{Q}^* \underline{\mathbf{M}} \mathbf{Q} = \begin{bmatrix} \lambda & \mathbf{0}_{1,n-1} \\ \mathbf{0}_{n-1,1} & \mathbf{D} \end{bmatrix}.$$

If

$$\|\mathbf{D}\| + \|\mathbf{M} - \underline{\mathbf{M}}\| \leq \frac{\lambda}{5}, \quad (\text{B.3})$$

then the largest eigenvalue of  $\mathbf{M}$  in magnitude has multiplicity 1 and the corresponding eigenvector  $\tilde{\mathbf{q}}$  satisfies

$$\sin \angle(\tilde{\mathbf{q}}, \mathbf{q}_1) \leq \frac{4\|(\mathbf{M} - \underline{\mathbf{M}})\mathbf{q}_1\|_2}{\lambda}. \quad (\text{B.4})$$

**Remark B.0.2.** In Lemma B.0.1, the rank-1 matrix  $\lambda \mathbf{q}_1 \mathbf{q}_1^*$  is considered as the ground truth matrix. Then  $\mathbf{M} - \underline{\mathbf{M}} + \mathbf{Q}_2 \mathbf{D} \mathbf{Q}_2^*$  corresponds to perturbation in  $\mathbf{M}$  relative to the ground truth matrix  $\underline{\mathbf{M}}$ . Also note that  $\mathbf{Q}_2 \mathbf{D} \mathbf{Q}_2^* \mathbf{q}_1 = \mathbf{0}$ .

In the remainder of this section, we obtain an upper bound on the error in  $\hat{\mathbf{b}}$  by applying Lemma B.0.1 to  $\underline{\mathbf{M}} = \mathbb{E}[\mathbf{\Gamma}_s] \mathbb{E}[\mathbf{\Gamma}_s]^*$ ,  $\mathbf{M} = \mathbf{\Gamma} \mathbf{\Gamma}^* - \sum_{m=1}^M \sigma_w^2 L \mathbf{\Phi}_m^* \mathbf{\Phi}_m$ ,  $\mathbf{q}_1 = \mathbf{b}$ , and  $\hat{\mathbf{q}} = \hat{\mathbf{b}}$ .

By (B.2), we have  $\mathbf{D} = \mathbf{0}$  and  $\lambda = K^2 \|\mathbf{x}\|_2^2 \|\mathbf{a}\|_1^2 \|\mathbf{b}\|_2^2$ . Then we show that the

spectral norm of the perturbation term, which is rewritten as

$$\begin{aligned} & \mathbf{\Gamma}\mathbf{\Gamma}^* - \mathbb{E}_w[\mathbf{\Gamma}_n\mathbf{\Gamma}_n^*] - \mathbb{E}[\mathbf{\Gamma}_s]\mathbb{E}[\mathbf{\Gamma}_s]^* \\ &= \mathbf{\Gamma}_s\mathbf{\Gamma}_s^* - \mathbb{E}[\mathbf{\Gamma}_s]\mathbb{E}[\mathbf{\Gamma}_s]^*, \end{aligned} \quad (\text{B.5a})$$

$$+ \mathbf{\Gamma}_s\mathbf{\Gamma}_n^* + \mathbf{\Gamma}_n\mathbf{\Gamma}_s^*, \quad (\text{B.5b})$$

$$+ \mathbf{\Gamma}_n\mathbf{\Gamma}_n^* - \mathbb{E}_w[\mathbf{\Gamma}_n\mathbf{\Gamma}_n^*], \quad (\text{B.5c})$$

satisfies (B.3). We will compute an upper estimate of the spectral norm of each summand, divided by  $\lambda$ , separately. Then we combine these estimates using the triangle inequality.

**Perturbation due to signal term:** Note that the first summand  $\mathbf{\Gamma}_s\mathbf{\Gamma}_s^* - \mathbb{E}[\mathbf{\Gamma}_s]\mathbb{E}[\mathbf{\Gamma}_s]^*$  in (B.5a) has entries, which are fourth-order Gaussian random variables. We decompose it using second-order random variables as

$$\begin{aligned} & \mathbf{\Gamma}_s\mathbf{\Gamma}_s^* - \mathbb{E}[\mathbf{\Gamma}_s]\mathbb{E}[\mathbf{\Gamma}_s]^* \\ &= (\mathbf{\Gamma}_s - \mathbb{E}[\mathbf{\Gamma}_s])(\mathbf{\Gamma}_s - \mathbb{E}[\mathbf{\Gamma}_s])^* + \mathbb{E}[\mathbf{\Gamma}_s](\mathbf{\Gamma}_s - \mathbb{E}[\mathbf{\Gamma}_s])^* + (\mathbf{\Gamma}_s - \mathbb{E}[\mathbf{\Gamma}_s])\mathbb{E}[\mathbf{\Gamma}_s]^*. \end{aligned} \quad (\text{B.6})$$

We have already computed  $\mathbb{E}[\mathbf{\Gamma}_s]$  in (B.1). It remains to upper bound the spectral norm of  $\mathbf{\Gamma}_s - \mathbb{E}[\mathbf{\Gamma}_s]$ . By the definitions of  $\mathbf{\Gamma}_s$  and  $\rho_x$ , we obtain

$$\begin{aligned} \|\mathbf{\Gamma}_s - \mathbb{E}[\mathbf{\Gamma}_s]\| &\leq \left\| \sum_{m=1}^M a_m (\mathbf{\Phi}_m^* \mathbf{S} \mathbf{C} \mathbf{S}^* \mathbf{\Phi}_m \mathbf{b} - \mathbb{E}_\phi[\mathbf{\Phi}_m^* \mathbf{S} \mathbf{C} \mathbf{S}^* \mathbf{\Phi}_m \mathbf{b}]) \check{\mathbf{S}}^* \check{\mathbf{S}} \mathbf{C} \mathbf{x} \right\| \\ &\leq \left\| \sum_{m=1}^M a_m (\mathbf{\Phi}_m^* \mathbf{S} \mathbf{C} \mathbf{S}^* \mathbf{\Phi}_m \mathbf{b} - \mathbb{E}_\phi[\mathbf{\Phi}_m^* \mathbf{S} \mathbf{C} \mathbf{S}^* \mathbf{\Phi}_m \mathbf{b}]) \check{\mathbf{S}}^* \right\| \|\check{\mathbf{S}} \mathbf{C} \mathbf{x}\| \\ &\leq \sqrt{\rho_x} \left\| \sum_{m=1}^M a_m (\mathbf{\Phi}_m^* \mathbf{S} \mathbf{C} \mathbf{S}^* \mathbf{\Phi}_m \mathbf{b} - \mathbb{E}_\phi[\mathbf{\Phi}_m^* \mathbf{S} \mathbf{C} \mathbf{S}^* \mathbf{\Phi}_m \mathbf{b}]) \check{\mathbf{S}}^* \right\|, \end{aligned} \quad (\text{B.7})$$

where  $\check{\mathbf{S}} \in \mathbb{R}^{(2K-1) \times L}$  is defined by

$$\check{\mathbf{S}} = \begin{bmatrix} \begin{bmatrix} \mathbf{0}_{K-1, L-K+1} & \mathbf{I}_{K-1} \end{bmatrix} \\ \begin{bmatrix} \mathbf{I}_K & \mathbf{0}_{K, L-K} \end{bmatrix} \end{bmatrix}.$$

The right-hand side of (B.7) except the constant factor  $\sqrt{\rho_x}$  is upper bounded by the following lemma.

**Lemma B.0.3.** *Suppose that (A2) holds. For any  $\beta \in \mathbb{N}$ , there is a constant  $C(\beta)$  that depends only on  $\beta$  such that*

$$\left\| \sum_{m=1}^M a_m (\Phi_m^* \mathbf{S} \mathbf{C}_{\mathbf{S}^* \Phi_m \mathbf{b}} - \mathbb{E}_\phi \Phi_m^* \mathbf{S} \mathbf{C}_{\mathbf{S}^* \Phi_m \mathbf{b}}) \check{\mathbf{S}}^* \right\| \leq C(\beta) K \sqrt{M} \|\mathbf{a}\|_\infty \|\mathbf{b}\|_2 \log^\alpha(MKL) \quad (\text{B.8})$$

holds with probability  $1 - K^{-\beta}$ .

By applying (B.1), (B.7), Lemma B.0.3 together with the fact  $\sqrt{\rho_x} \leq C_0 \|\mathbf{x}\|_2$  to (B.6), we obtain that

$$\frac{\|\mathbf{\Gamma}_s \mathbf{\Gamma}_s^* - \mathbb{E}[\mathbf{\Gamma}_s] \mathbb{E}[\mathbf{\Gamma}_s]^*\|}{\lambda} \leq \frac{C(\beta) \sqrt{M} \|\mathbf{a}\|_\infty \log^\alpha(MKL)}{\|\mathbf{a}\|_1} \leq \frac{C(\beta) \mu \log^\alpha(MKL)}{\nu \sqrt{M}} \quad (\text{B.9})$$

holds with probability  $1 - K^{-\beta}$ .

**Perturbation due to signal-noise cross term:** Next we consider the second term in (B.5b). By the triangle inequality, we have

$$\|\mathbf{\Gamma}_s \mathbf{\Gamma}_n^* + \mathbf{\Gamma}_n \mathbf{\Gamma}_s^*\| \leq \|\mathbf{\Gamma}_s \mathbf{\Gamma}_n^*\| + \|\mathbf{\Gamma}_n \mathbf{\Gamma}_s^*\| \leq 2 \|\mathbf{\Gamma}_s \mathbf{\Gamma}_n^*\|.$$

Therefore, it suffices to upper estimate  $\|\mathbf{\Gamma}_s \mathbf{\Gamma}_n^*\|$ . To this end, we decompose  $\mathbf{\Gamma}_s \mathbf{\Gamma}_n^*$  as

$$\mathbf{\Gamma}_s \mathbf{\Gamma}_n^* = (\mathbf{\Gamma}_s - \mathbb{E}[\mathbf{\Gamma}_s]) \mathbf{\Gamma}_n^* + \mathbb{E}[\mathbf{\Gamma}_s] \mathbf{\Gamma}_n^*. \quad (\text{B.10})$$

Note that the first summand in the right-hand-side of (B.10) is written as

$$(\mathbf{\Gamma}_s - \mathbb{E}[\mathbf{\Gamma}_s])\mathbf{\Gamma}_n^* = \left( \sum_{m=1}^M a_m \mathbf{\Phi}_m^* \mathbf{S} \mathbf{C}_{\mathbf{S}^* \mathbf{\Phi}_m \mathbf{b}} \check{\mathbf{S}}^* - \mathbb{E}_\phi[a_m \mathbf{\Phi}_m^* \mathbf{S} \mathbf{C}_{\mathbf{S}^* \mathbf{\Phi}_m \mathbf{b}} \check{\mathbf{S}}^*] \right) \left( \sum_{m'=1}^M \check{\mathbf{S}} \mathbf{C}_x \mathbf{C}_{\mathbf{w}_{m'}}^* \mathbf{S}^* \mathbf{\Phi}_{m'} \right), \quad (\text{B.11})$$

where the first and second factors of the right-hand-side of (B.11) are upper bounded in the spectral norm respectively by Lemma B.0.3 and by the following lemma.

**Lemma B.0.4.** *Suppose that (A1) and (A2) hold. For any  $\beta \in \mathbb{N}$ , there is a constant  $C(\beta)$  that depends only on  $\beta$  such that*

$$\left\| \sum_{m=1}^M \check{\mathbf{S}} \mathbf{C}_x \mathbf{C}_{\mathbf{w}_m}^* \mathbf{S}^* \mathbf{\Phi}_m \right\| \leq C(\beta) \rho_{x,w} \sqrt{MK} \log^\alpha(MKL) \quad (\text{B.12})$$

holds with probability  $1 - K^{-\beta}$ .

By applying Lemmas B.0.3 and (B.0.4) to (B.11), we obtain that

$$\|(\mathbf{\Gamma}_s - \mathbb{E}[\mathbf{\Gamma}_s])\mathbf{\Gamma}_n^*\| \leq C(\beta) \rho_{x,w} MK^{3/2} \|\mathbf{a}\|_\infty \|\mathbf{b}\|_2 \log^\alpha(MKL) \quad (\text{B.13})$$

holds with probability  $1 - K^{-\beta}$ .

Next, the second summand in the right-hand-side of (B.10) is written as

$$\mathbb{E}[\mathbf{\Gamma}_s]\mathbf{\Gamma}_n^* = K \|\mathbf{a}\|_1 \mathbf{b} \left( \sum_{m'=1}^M \mathbf{e}_1^* \mathbf{C}_x \mathbf{C}_{\mathbf{w}_{m'}}^* \mathbf{S}^* \mathbf{\Phi}_{m'} \right), \quad (\text{B.14})$$

whose spectral norm is upper bounded by using the following lemma.

**Lemma B.0.5.** *Suppose that (A1) and (A2) hold. For any  $\beta \in \mathbb{N}$ , there is a constant  $C(\beta)$  that depends only on  $\beta$  such that*

$$\left\| \sum_{m'=1}^M \mathbf{e}_1^* \mathbf{C}_x \mathbf{C}_{\mathbf{w}_{m'}}^* \mathbf{S}^* \mathbf{\Phi}_{m'} \right\| \leq C(\beta) \rho_{x,w} \sqrt{MD} \log^\alpha(MKL)$$

holds with probability  $1 - K^{-\beta}$ .

The proof of Lemma B.0.5 is very similar to that of Lemma B.0.4. The proof of Lemma B.0.4 involves the following optimization formulation:

$$\max_{\mathbf{z} \in B_2^{2K-1}} \max_{\mathbf{q} \in B_2^D} \sum_{m=1}^M \mathbf{z}^* \check{\mathbf{S}} \mathbf{C}_x \mathbf{C}_{w_m}^* \mathbf{S}^* \Phi_m \mathbf{q}.$$

Instead of maximizing over  $\mathbf{z} \in B_2^{2K-1}$ , we fix  $\mathbf{z}$  to  $\check{\mathbf{S}} \mathbf{e}_1$ . Equivalently, we replace the unit ball  $B_2^{2K-1}$  by the singleton set  $\{\check{\mathbf{S}} \mathbf{e}_1\}$ . This replacement simply removes the entropy integral corresponding to  $B_2^{2K-1}$ . Except this point, the proofs for the two lemmas are identical. Thus we omit further details.

Applying Lemma B.0.5 to (B.14) implies that

$$\|\mathbb{E}[\mathbf{\Gamma}_s] \mathbf{\Gamma}_n^*\| \leq C(\beta) \rho_{x,w} \sqrt{MK} \sqrt{D} \|\mathbf{a}\|_1 \|\mathbf{b}\|_2 \log^\alpha(MKL) \quad (\text{B.15})$$

holds with probability  $1 - K^{-\beta}$ .

By combining (B.13) and (B.15), after plugging in the definitions of  $\eta$ ,  $\mu$ , and  $\nu$ , we obtain that

$$\frac{\|\mathbf{\Gamma}_s \mathbf{\Gamma}_n^* + \mathbf{\Gamma}_n \mathbf{\Gamma}_s^*\|}{\lambda} \leq \frac{C(\beta) \log^\alpha(MKL)}{\sqrt{\eta}} \cdot \frac{\rho_{x,w}}{\|\mathbf{x}\|_2 \sigma_w \sqrt{L}} \cdot \left( \frac{\mu}{\nu^2 M} + \frac{\sqrt{D}}{\nu \sqrt{MK}} \right) \quad (\text{B.16})$$

holds with probability  $1 - 2K^{-\beta}$ .

**Perturbation due to noise term:** Finally, we derive an upper bound on the spectral norm of the last term in (B.5c) using the following lemma.

**Lemma B.0.6.** *Suppose that (A2) holds. For any  $\beta \in \mathbb{N}$ , there is a constant  $C(\beta)$  that depends only on  $\beta$  such that*

$$\|\mathbf{\Gamma}_n \mathbf{\Gamma}_n^* - \mathbb{E}_w[\mathbf{\Gamma}_n \mathbf{\Gamma}_n^*]\| \leq C(\beta) \rho_w M^{3/2} \sqrt{KD} \log^\alpha(MKL)$$

holds with probability  $1 - K^{-\beta}$ .

We also a tail bound on  $\rho_w$  given by the following lemma from [83].

**Lemma B.0.7** ([83, Lemma 5.9]). *Suppose that (A2) holds. For any  $\beta \in \mathbb{N}$ , there is a constant  $C(\beta)$  that depends only on  $\beta$  such that*

$$\rho_w \leq C(\beta) \sigma_w^2 \sqrt{KL} \log^\alpha(MKL) \quad (\text{B.17})$$

*holds with probability  $1 - K^{-\beta}$ .*

By Lemma B.0.7 and (3.22), the corresponding relative perturbation is upper bounded by

$$\frac{\|\mathbf{\Gamma}_n \mathbf{\Gamma}_n^* - \mathbb{E}_w[\mathbf{\Gamma}_n \mathbf{\Gamma}_n^*]\|}{K^2 \|\mathbf{x}\|_2^2 \|\mathbf{a}\|_1^2 \|\mathbf{b}\|_2^2} \leq \frac{C(\beta) \log^\alpha(MKL)}{\eta} \cdot \frac{\sqrt{D}}{\nu^2 \sqrt{ML}} \quad (\text{B.18})$$

with probability  $1 - K^{-\beta}$ .

Then it follows from (B.9), (B.16), and (B.18) that the condition in (B.3) is satisfied by the assumptions in (A.6) and (A.5). Therefore, Lemma B.0.1 provides the upper bound on the estimation error in (A.7), which is obtained by plugging (B.9), (B.16), and (B.18) to (B.4). This completes the proof.

## APPENDIX C

### CONVERGENCE OF NON-CONVEX OPTIMIZATION ALGORITHMS

#### C.1 Convergence of the Alternating Eigenvectors Method

Algorithm 1 iteratively updates the estimates of  $\mathbf{a}$ ,  $\mathbf{b}$  from a function of the matrix  $\mathbf{A} = \Phi^*(\mathbf{Y}^*\mathbf{Y} - \sigma_w^2(M-1)L\mathbf{I}_{MK})\Phi$  and previous estimates. Propositions A.1.2 and A.1.3 show the convergence of the iterations in Algorithm 1 that alternately update the estimates  $\hat{\mathbf{a}}$  and  $\hat{\mathbf{b}}$  under the randomness assumptions in (A1) and (A2). Similarly to the analysis of the spectral initialization in Section B, we prove Propositions A.1.2 and A.1.3 by using the Davis-Kahan Theorem in Lemma B.0.1. To this end, we first compute tail estimates of norms of the deviation of the random matrix  $\mathbf{A}$  from its expectation  $\underline{\mathbf{A}} = \mathbb{E}[\mathbf{A}]$  below.

##### C.1.1 Tail estimates of deviations

Algorithm 1 updates the estimates  $\hat{\mathbf{a}}$  as the least dominant eigenvector of  $(\mathbf{I}_M \otimes \hat{\mathbf{b}}^*)\mathbf{A}(\mathbf{I}_M \otimes \hat{\mathbf{b}})$  where  $\hat{\mathbf{b}}$  denotes the estimate in the previous step. The other estimate  $\hat{\mathbf{b}}$  is updated similarly from  $(\hat{\mathbf{a}}^* \otimes \mathbf{I}_D)\mathbf{A}(\hat{\mathbf{a}} \otimes \mathbf{I}_D)$ . The matrices involved in these updates are restricted version of  $\mathbf{A}$  with separable projection operators.

In order to get a tightened perturbation bound for the estimates, we introduce a new matrix norm with this separability structure. To define the new norm, we need operators that rearrange an  $M$ -by- $D$  matrix into a column vector of length  $MD$  and



vice versa. For  $\mathbf{V} = [\mathbf{v}_1, \dots, \mathbf{v}_M] \in \mathbb{C}^{M \times D}$ , define

$$\text{vec}(\mathbf{V}) = [\mathbf{v}_1^\top, \dots, \mathbf{v}_M^\top]^\top.$$

Let  $\text{mat}(\cdot)$  denote the inverse of  $\text{vec}(\cdot)$  so that

$$\text{mat}(\text{vec}(\mathbf{V})) = \mathbf{V}, \quad \forall \mathbf{V} \in \mathbb{C}^{M \times D}$$

and

$$\text{vec}(\text{mat}(\mathbf{v})) = \mathbf{v}, \quad \forall \mathbf{v} \in \mathbb{C}^{MD}.$$

With these vectorization and matricization operators, we define the matricized  $S_p$ -norm of  $\mathbf{v} \in \mathbb{C}^{MD}$  by

$$||| \mathbf{v} |||_{S_p} = \|\text{mat}(\mathbf{v})\|_{S_p}.$$

Then the matricized operator norm of  $\mathbf{M} \in \mathbb{C}^{MD \times MD}$  is defined by

$$||| \mathbf{M} |||_{S_p \rightarrow S_q} := \max_{||| \mathbf{v} |||_{S_p} \leq 1} ||| \mathbf{M} \mathbf{v} |||_{S_q}.$$

For  $p = 1$  and  $q = \infty$ , by the Courant-Fischer minimax principle, the matricized operator norm is written as a variational form

$$\begin{aligned} ||| \mathbf{M} |||_{S_1 \rightarrow S_\infty} &= \max_{\mathbf{r}, \mathbf{r}' \in \mathbb{C}^{M \times D}} |\langle \text{vec}(\mathbf{r}'), \mathbf{M} \text{vec}(\mathbf{r}) \rangle| \\ &\text{subject to } \|\mathbf{r}\|_{S_1} \leq 1, \|\mathbf{r}'\|_{S_1} \leq 1. \end{aligned}$$

Since the unit ball with respect to the  $S_1$ -norm is given as the convex hull of all

unit- $S_2$ -norm matrices of rank-1,  $||| \mathbf{M} |||_{S_1 \rightarrow S_\infty}$  is equivalently rewritten as

$$\begin{aligned} ||| \mathbf{M} |||_{S_1 \rightarrow S_\infty} &= \max_{\mathbf{\Upsilon}, \mathbf{\Upsilon}' \in \mathbb{C}^{M \times D}} |\langle \text{vec}(\mathbf{\Upsilon}'), \mathbf{M} \text{vec}(\mathbf{\Upsilon}) \rangle| \\ &\text{subject to } \|\mathbf{\Upsilon}\|_{S_2} \leq 1, \|\mathbf{\Upsilon}'\|_{S_2} \leq 1 \\ &\text{rank}(\mathbf{\Upsilon}) = \text{rank}(\mathbf{\Upsilon}') = 1. \end{aligned} \quad (\text{C.1})$$

Therefore, by dropping the rank-1 constraints in (C.1), we obtain

$$||| \mathbf{M} |||_{S_1 \rightarrow S_\infty} \leq \|\mathbf{M}\|, \quad \forall \mathbf{M} \in \mathbb{C}^{MD \times MD}. \quad (\text{C.2})$$

The following lemma provides a tail estimate of  $||| \mathbf{E} |||_{S_1 \rightarrow S_\infty}$  divided by  $K^2 \|\mathbf{x}\|_2^2 \|\mathbf{u}\|_2^2$ , which amounts to the spectral gap between the two smallest eigenvalues of  $\underline{\mathbf{A}}$ . Compared to the analogous tail estimate for its spectral norm, derived in [83, Section 3.2], the tail estimate for  $||| \mathbf{E} |||_{S_1 \rightarrow S_\infty}$  is smaller in order. This is the reason why we obtain a better sample complexity by introducing the extra rank-1 structure to the prior model on impulse responses.

**Lemma C.1.1.** *Let  $\mathbf{E} = \mathbf{A} - \underline{\mathbf{A}}$ . For any  $\beta \in \mathbb{N}$ , there exist a numerical constant  $C$  and a constant  $C(\beta)$  that depends only on  $\beta$  such that*

$$\begin{aligned} \frac{||| \mathbf{E} |||_{S_1 \rightarrow S_\infty}}{K^2 \|\mathbf{x}\|_2^2 \|\mathbf{u}\|_2^2} &\leq C(\beta) \log^\alpha(MKL) \left[ \left( \frac{1}{\sqrt{M}} + \sqrt{\frac{D}{K}} \right) \mu^2 \right. \\ &\quad \left. + \frac{\rho_{x,w}}{\sqrt{\eta K L \sigma_w} \|\mathbf{x}\|_2} \left( \mu \left( \frac{\sqrt{K}}{M} + \sqrt{\frac{D}{M}} + \sqrt{\frac{D}{K}} \right) + 1 \right) + \frac{\sqrt{D}}{\eta \sqrt{L}} \right] \end{aligned} \quad (\text{C.3})$$

*holds with probability  $1 - CK^{-\beta}$ .*

*Proof of Lemma C.1.1.* The derivation of (C.3) is similar to that for the analogous tail estimate for  $\|\mathbf{E}\|$  in [83, Section 3.2]. We use the same decomposition of  $\mathbf{E}$ , which is briefly summarized below.

We decompose  $\mathbf{Y}$  as  $\mathbf{Y} = \mathbf{Y}_s + \mathbf{Y}_n$ , where the noise-free portion  $\mathbf{Y}_s$  (resp. the noise portion  $\mathbf{Y}_n$ ) is obtained as we replace  $\mathbf{y}_m = \mathbf{h}_m \otimes \mathbf{x} + \mathbf{w}_m$  in  $\mathbf{Y}$  by its first

summand  $\mathbf{h}_m \otimes \mathbf{x}$  (resp. by its second summand  $\mathbf{w}_m$ ) for all  $m = 1, \dots, M$ . Then  $\mathbf{E}$  is written as the sum of three matrices whose entries are given as polynomials of subgaussian random variables of different order as follows.

$$\mathbf{E} = \Phi^* \mathbf{Y}_s^* \mathbf{Y}_s \Phi - \mathbb{E}[\Phi^* \mathbf{Y}_s^* \mathbf{Y}_s \Phi] \quad (\text{C.4})$$

$$+ \Phi^* \mathbf{Y}_s^* \mathbf{Y}_n \Phi + \Phi^* \mathbf{Y}_n^* \mathbf{Y}_s \Phi \quad (\text{C.5})$$

$$+ \Phi^* (\mathbf{Y}_n^* \mathbf{Y}_n - \sigma_w^2 (M-1) L \mathbf{I}_{MK}) \Phi. \quad (\text{C.6})$$

We first compute tail estimates of the components; the tail estimate in (C.3) is then obtained by combining these results via the triangle inequality.

For the first summand in (C.4) and the last summand in (C.6), we were not able to reduce their tail estimates in order compared to the spectral norms. Thus we use their tail estimates on the spectral norms derived in [83, Section 3.2], which are also valid tail estimates by (C.2). For the completeness, we provide the corresponding lemmas below.

**Lemma C.1.2** ([83, Lemma 3.5]). *Suppose that (A1) holds. For any  $\beta \in \mathbb{N}$ , there exist a numerical constant  $\alpha \in \mathbb{N}$  and a constant  $C(\beta)$  that depends only on  $\beta$  such that*

$$\frac{\|\Phi^* \mathbf{Y}_s^* \mathbf{Y}_s \Phi - \mathbb{E}[\Phi^* \mathbf{Y}_s^* \mathbf{Y}_s \Phi]\|}{K^2 \|\mathbf{x}\|_2^2 \|\mathbf{u}\|_2^2} \leq C(\beta) \log^\alpha(MKL) \left( \sqrt{\frac{1}{M}} + \sqrt{\frac{D}{K}} \right) \mu^2 \quad (\text{C.7})$$

*holds with probability  $1 - CK^{-\beta}$ .*

**Lemma C.1.3** ([83, Lemma 3.7]). *Suppose that (A1) holds. For any  $\beta \in \mathbb{N}$ , there is a constant  $C(\beta)$  that depends only on  $\beta$  such that*

$$\frac{\|\Phi^* (\mathbf{Y}_n^* \mathbf{Y}_n - \sigma_w^2 (M-1) L \mathbf{I}_{MK}) \Phi\|}{K^2 \|\mathbf{x}\|_2^2 \|\mathbf{u}\|_2^2} \leq \frac{C(\beta) \log^\alpha(MKL)}{\eta} \cdot \sqrt{\frac{D}{L}} \quad (\text{C.8})$$

with probability  $1 - CK^{-\beta}$ .

For the second and third terms in (C.5), we use their tail estimates given in the following lemma.

**Lemma C.1.4.** *Suppose that (A1) holds. For any  $\beta \in \mathbb{N}$ , there exists a constant  $C(\beta)$  that depends only on  $\beta$  such that, conditional on the noise vector  $\mathbf{w}$ ,*

$$\frac{||| \Phi^* \mathbf{Y}_s^* \mathbf{Y}_n \Phi |||_{S_1 \rightarrow S_\infty}}{K^2 \|\mathbf{x}\|_2^2 \|\mathbf{u}\|_2^2} \leq \frac{C(\beta) \rho_{x,w}}{\sqrt{\eta K L} \sigma_w \|\mathbf{x}\|_2} \left( \mu \left( \frac{\sqrt{K}}{M} + \sqrt{\frac{D}{M}} + \sqrt{\frac{D}{K}} \right) + 1 \right) \quad (\text{C.9})$$

holds with probability  $1 - CK^{-\beta}$ .

Finally, the tail estimate in (C.3) is obtained by combining (C.7), (C.7), and (C.9) via the triangle inequality. This completes the proof.  $\square$

We will also make use of a tail estimate of  $||| \mathbf{E} \mathbf{u} |||_{S_\infty} / \|\mathbf{u}\|_2$ , again normalized by factor  $K^2 \|\mathbf{x}\|_2^2 \|\mathbf{u}\|_2^2$ . The following lemma, which provides a relevant tail estimate, is a direct consequence of Lemma C.1.4 and [83, Lemma 3.8].

**Lemma C.1.5.** *Let  $\mathbf{E} = \mathbf{A} - \underline{\mathbf{A}}$ . For any  $\beta \in \mathbb{N}$ , there exist a numerical constant  $C$  and a constant  $C(\beta)$  that depends only on  $\beta$  such that*

$$\frac{||| \mathbf{E} \mathbf{u} |||_{S_\infty}}{K^2 \|\mathbf{x}\|_2^2 \|\mathbf{u}\|_2^2} \leq C(\beta) \log^\alpha(MKL) \left[ \frac{\rho_{x,w}}{\sqrt{\eta K L} \sigma_w \|\mathbf{x}\|_2} \left( \mu \left( \frac{\sqrt{K}}{M} + \sqrt{\frac{D}{M}} + \sqrt{\frac{D}{K}} \right) + 1 \right) + \frac{\sqrt{D}}{\eta \sqrt{ML}} \right] \quad (\text{C.10})$$

holds with probability  $1 - CK^{-\beta}$ .

### C.1.2 Proof of Proposition A.1.2

To simplify notations, let  $\theta = \angle(\mathbf{b}, \hat{\mathbf{b}})$  denote the principal angle between the two subspaces spanned respectively by  $\mathbf{b}$  and  $\hat{\mathbf{b}}$ , i.e.,  $\theta \in [0, \pi/2]$  satisfies

$$\sin \theta = \|\mathbf{P}_{\mathbf{b}^\perp} \hat{\mathbf{b}}\|_2, \quad \cos \theta = \|\mathbf{P}_{\mathbf{b}} \hat{\mathbf{b}}\|_2,$$

where  $\mathbf{P}_{\mathbf{b}}$  denotes the orthogonal projection onto the span of  $\mathbf{b}$ . The assumption in (A.8) implies  $\theta \leq \pi/4$ .

Recall that Algorithm 1 updates  $\hat{\mathbf{a}}$  from a given estimate  $\hat{\mathbf{b}}$  in the previous step as the eigenvector of the matrix  $(\mathbf{I}_M \otimes \hat{\mathbf{b}}^*)\mathbf{A}(\mathbf{I}_M \otimes \hat{\mathbf{b}})$  corresponding to the smallest eigenvalue. Without loss of generality, we may assume that  $\|\hat{\mathbf{b}}\|_2 = 1$ .

By direct calculation, we obtain that  $\underline{\mathbf{A}} = \mathbb{E}[\mathbf{A}]$  is rewritten as

$$\underline{\mathbf{A}} = K^2\|\mathbf{x}\|_2^2\|\mathbf{b}\|_2^2(\|\mathbf{a}\|_2^2\mathbf{I}_M - \text{diag}(|\mathbf{a}|^2)) \otimes \mathbf{P}_{\mathbf{b}^\perp} + K^2\|\mathbf{x}\|_2^2\|\mathbf{b}\|_2^2(\|\mathbf{a}\|_2^2\mathbf{I}_M - \mathbf{a}\mathbf{a}^*) \otimes \mathbf{P}_{\mathbf{b}}. \quad (\text{C.11})$$

Then

$$(\mathbf{I}_M \otimes \hat{\mathbf{b}}^*)\underline{\mathbf{A}}(\mathbf{I}_M \otimes \hat{\mathbf{b}}) = K^2\|\mathbf{x}\|_2^2\|\mathbf{b}\|_2^2(\|\mathbf{a}\|_2^2\mathbf{I}_M - \cos^2\theta \mathbf{a}\mathbf{a}^*) - K^2\|\mathbf{x}\|_2^2\|\mathbf{b}\|_2^2 \sin^2\theta \text{diag}(|\mathbf{a}|^2). \quad (\text{C.12})$$

Here  $|\mathbf{a}|^2$  denotes the vector whose  $k$ th entry is the squared magnitude of the  $k$ th entry of  $\mathbf{a}$  and  $\text{diag}(|\mathbf{a}|^2)$  is a diagonal matrix whose diagonal entries are given by  $|\mathbf{a}|^2$ .

We verify that the matrix  $\|\mathbf{a}\|_2^2\mathbf{I}_M - \cos^2\theta \mathbf{a}\mathbf{a}^*$  is positive definite and its smallest eigenvalue, which has multiplicity 1, is smaller than the next smallest eigenvalue by  $\|\mathbf{a}\|_2^2 \cos^2\theta$ . Furthermore,  $\mathbf{a}$  is collinear with the eigenvector corresponding to the smallest eigenvalue.

Let us consider the following matrix:

$$\begin{aligned} & K^2\|\mathbf{x}\|_2^2\|\mathbf{b}\|_2^2\|\mathbf{a}\|_2^2\mathbf{I}_M - (\mathbf{I}_M \otimes \hat{\mathbf{b}}^*)\mathbf{A}(\mathbf{I}_M \otimes \hat{\mathbf{b}}) \\ &= K^2\|\mathbf{x}\|_2^2\|\mathbf{b}\|_2^2 \cos^2\theta \mathbf{a}\mathbf{a}^* \\ &+ K^2\|\mathbf{x}\|_2^2\|\mathbf{b}\|_2^2 \sin^2\theta \text{diag}(|\mathbf{a}|^2) - (\mathbf{I}_M \otimes \hat{\mathbf{b}}^*)\mathbf{E}(\mathbf{I}_M \otimes \hat{\mathbf{b}}), \end{aligned}$$

which we considered as a perturbed version of  $K^2\|\mathbf{x}\|_2^2\|\mathbf{b}\|_2^2 \cos^2\theta \mathbf{a}\mathbf{a}^*$ . Then the

perturbation, that is the difference of the two matrices, satisfies

$$\begin{aligned}
& \left\| K^2 \|\mathbf{x}\|_2^2 \|\mathbf{b}\|_2^2 \|\mathbf{a}\|_2^2 \mathbf{I}_M - (\mathbf{I}_M \otimes \widehat{\mathbf{b}}^*) \mathbf{A} (\mathbf{I}_M \otimes \widehat{\mathbf{b}}) - K^2 \|\mathbf{x}\|_2^2 \|\mathbf{b}\|_2^2 \cos^2 \theta \mathbf{a} \mathbf{a}^* \right\| \\
& \leq \left\| K^2 \|\mathbf{x}\|_2^2 \|\mathbf{b}\|_2^2 \sin^2 \theta \text{diag}(|\mathbf{a}|^2) \right\| + \|(\mathbf{I}_M \otimes \widehat{\mathbf{b}}^*) \mathbf{E} (\mathbf{I}_M \otimes \widehat{\mathbf{b}})\| \\
& \leq K^2 \|\mathbf{x}\|_2^2 \|\mathbf{b}\|_2^2 \|\mathbf{a}\|_\infty^2 \sin^2 \theta + ||| \mathbf{E} |||_{S_1 \rightarrow S_\infty}.
\end{aligned} \tag{C.13}$$

For sufficiently large  $C_1(\beta)$ , the conditions in (A.8), (A.9), (A.10), (A.11) imply

$$K^2 \|\mathbf{x}\|_2^2 \|\mathbf{b}\|_2^2 \|\mathbf{a}\|_2^2 \cos^2 \theta > 2(K^2 \|\mathbf{x}\|_2^2 \|\mathbf{b}\|_2^2 \|\mathbf{a}\|_\infty^2 \sin^2 \theta + ||| \mathbf{E} |||_{S_1 \rightarrow S_\infty}).$$

Therefore,  $\widehat{\mathbf{a}}$  is a unique dominant eigenvector of  $K^2 \|\mathbf{x}\|_2^2 \|\mathbf{b}\|_2^2 \|\mathbf{a}\|_2^2 \mathbf{I}_M - (\mathbf{I}_M \otimes \widehat{\mathbf{b}}^*) \mathbf{A} (\mathbf{I}_M \otimes \widehat{\mathbf{b}})$ .

Next we apply Lemma B.0.1 for

$$\begin{aligned}
\mathbf{M} &= K^2 \|\mathbf{x}\|_2^2 \|\mathbf{b}\|_2^2 \cos^2 \theta \mathbf{a} \mathbf{a}^*, \\
\mathbf{M} &= K^2 \|\mathbf{x}\|_2^2 \|\mathbf{b}\|_2^2 \|\mathbf{a}\|_2^2 \mathbf{I}_M - (\mathbf{I}_M \otimes \widehat{\mathbf{b}}^*) \mathbf{A} (\mathbf{I}_M \otimes \widehat{\mathbf{b}}), \\
\mathbf{q}_1 &= \frac{\mathbf{a}}{\|\mathbf{a}\|_2}, \quad \widetilde{\mathbf{q}} = \widehat{\mathbf{a}}.
\end{aligned}$$

Then  $\lambda$  and  $\mathbf{D}$  in Lemma B.0.1 are given as  $\lambda = K^2 \|\mathbf{x}\|_2^2 \|\mathbf{b}\|_2^2 \|\mathbf{a}\|_2^2 \cos^2 \theta$  and  $\mathbf{D} = \mathbf{0}$ .

By (C.13), we have

$$\begin{aligned}
\frac{\|\mathbf{M} - \mathbf{M}\|}{\lambda} &\leq \frac{\|\mathbf{a}\|_\infty^2 \sin^2 \theta}{\|\mathbf{a}\|_2^2 \cos^2 \theta} + \frac{||| \mathbf{E} |||_{S_1 \rightarrow S_\infty}}{K^2 \|\mathbf{x}\|_2^2 \|\mathbf{b}\|_2^2 \|\mathbf{a}\|_2^2 \cos^2 \theta} \\
&\leq \frac{\mu^2}{M} + \frac{2||| \mathbf{E} |||_{S_1 \rightarrow S_\infty}}{K^2 \|\mathbf{x}\|_2^2 \|\mathbf{b}\|_2^2 \|\mathbf{a}\|_2^2},
\end{aligned}$$

where the last step follows from (A.8). Therefore, for sufficiently large  $C_1(\beta)$ , the conditions in (A.9), (A.10), (A.11) combined with Lemma C.1.1 satisfy (B.3) in Lemma B.0.1 and we obtain the error bound in (B.4).

It remains to compute  $\|(\mathbf{N} - \mathbf{M})\mathbf{q}_1\|_2/\lambda$ . The  $\ell_2$ -norm of  $(\mathbf{M} - \mathbf{M})\mathbf{q}_1$  satisfies

$$\begin{aligned} \|(\mathbf{M} - \mathbf{M})\mathbf{q}_1\|_2 &\leq \frac{K^2\|\mathbf{x}\|_2^2\|\mathbf{b}\|_2^2\sin^2\theta\|\text{diag}(|\mathbf{a}|^2)\mathbf{a}\|_2}{\|\mathbf{a}\|_2} + \frac{\|(\mathbf{I}_M \otimes \widehat{\mathbf{b}}^*)\mathbf{E}(\mathbf{a} \otimes \widehat{\mathbf{b}})\|_2}{\|\mathbf{a}\|_2} \\ &\leq K^2\|\mathbf{x}\|_2^2\|\mathbf{b}\|_2^2\|\mathbf{a}\|_\infty^2\sin^2\theta + 3\sin\theta\|\mathbf{E}\|_{S_1 \rightarrow S_\infty} + \frac{\cos^2\theta\|\mathbf{E}(\mathbf{a} \otimes \mathbf{b})\|_{S_\infty}}{\|\mathbf{a}\|_2\|\mathbf{b}\|_2}, \end{aligned} \quad (\text{C.14})$$

where the second step follow from the decomposition of  $\widehat{\mathbf{b}}$  given by

$$\widehat{\mathbf{b}} = \mathbf{P}_b\widehat{\mathbf{b}} + \mathbf{P}_{b^\perp}\widehat{\mathbf{b}}.$$

which satisfies  $\|\mathbf{P}_b\widehat{\mathbf{b}}\|_2 = \cos\theta$  and  $\|\mathbf{P}_{b^\perp}\widehat{\mathbf{b}}\|_2 = \sin\theta$ . By dividing the right-hand side of (C.14) by  $\lambda$ , we obtain

$$\begin{aligned} \frac{4\|(\mathbf{M} - \mathbf{M})\mathbf{q}_1\|_2}{\lambda} &\leq \frac{4\|\mathbf{a}\|_\infty^2\sin^2\theta}{\|\mathbf{a}\|_2^2\cos^2\theta} + \frac{12\sin^2\theta\|\mathbf{E}\|_{S_1 \rightarrow S_\infty}}{K^2\|\mathbf{x}\|_2^2\|\mathbf{b}\|_2^2\|\mathbf{a}\|_2^2\cos^2\theta} + \frac{4\|\mathbf{Eu}\|_{S_\infty}}{K^2\|\mathbf{x}\|_2^2\|\mathbf{u}\|_2^3} \\ &\leq \left(\frac{8\mu^2}{M} + \frac{24\|\mathbf{E}\|_{S_1 \rightarrow S_\infty}}{K^2\|\mathbf{x}\|_2^2\|\mathbf{u}\|_2^2}\right)\sin\theta + \frac{4\|\mathbf{Eu}\|_{S_\infty}}{K^2\|\mathbf{x}\|_2^2\|\mathbf{u}\|_2^3}, \end{aligned} \quad (\text{C.15})$$

where the second step follows from (A.8).

By Lemma C.1.1, the constant factor for  $\sin\theta$  in (C.15) becomes less than  $1/2$  as we choose  $C_1(\beta)$  in (A.9), (A.10), (A.11) sufficiently large. This gives (A.12), where the expression for  $\kappa$  follows from Lemma C.1.5. This completes the proof.

### C.1.3 Proof of Proposition A.1.3

The proof of Proposition A.1.3 is similar to that of Proposition A.1.2. Thus we will only highlight the differences between the two proofs.

Without loss of generality, we assume that  $\|\widehat{\mathbf{a}}\|_2 = 1$ . Let  $\check{\theta} = \angle(\mathbf{a}, \widehat{\mathbf{a}})$ . The assumption in (A.14) implies  $\check{\theta} \leq \pi/4$ . This time, we compute the least dominant

eigenvector of  $(\hat{\mathbf{a}}^* \otimes \mathbf{I}_D) \mathbf{A}(\hat{\mathbf{a}} \otimes \mathbf{I}_D)$ . From (C.11), we obtain

$$(\hat{\mathbf{a}}^* \otimes \mathbf{I}_D) \underline{\mathbf{A}}(\hat{\mathbf{a}} \otimes \mathbf{I}_D) = K^2 \|\mathbf{x}\|_2^2 \|\mathbf{a}\|_2^2 (\|\mathbf{b}\|_2^2 \mathbf{I}_D - \cos^2 \check{\theta} \mathbf{b} \mathbf{b}^*) - K^2 \|\mathbf{x}\|_2^2 \|\mathbf{b}\|_2^2 \|\mathbf{a}\| \odot \hat{\mathbf{a}} \| \hat{\mathbf{a}} \|_2^2 \mathbf{P}_{\mathbf{b}^\perp}. \quad (\text{C.16})$$

We consider the matrix

$$\begin{aligned} & K^2 \|\mathbf{x}\|_2^2 \|\mathbf{b}\|_2^2 \|\mathbf{a}\|_2^2 \mathbf{I}_D - (\hat{\mathbf{a}}^* \otimes \mathbf{I}_D) \mathbf{A}(\hat{\mathbf{a}} \otimes \mathbf{I}_D) \\ &= K^2 \|\mathbf{x}\|_2^2 \|\mathbf{a}\|_2^2 \cos^2 \check{\theta} \mathbf{b} \mathbf{b}^* \\ &+ K^2 \|\mathbf{x}\|_2^2 \|\mathbf{b}\|_2^2 \|\mathbf{a}\| \odot \hat{\mathbf{a}} \| \hat{\mathbf{a}} \|_2^2 \mathbf{P}_{\mathbf{b}^\perp} - (\hat{\mathbf{a}}^* \otimes \mathbf{I}_D) \mathbf{E}(\hat{\mathbf{a}} \otimes \mathbf{I}_D) \end{aligned}$$

as a perturbed version of  $K^2 \|\mathbf{x}\|_2^2 \|\mathbf{a}\|_2^2 \cos^2 \check{\theta} \mathbf{b} \mathbf{b}^*$ . The difference of the two matrices satisfies

$$\begin{aligned} & \left\| K^2 \|\mathbf{x}\|_2^2 \|\mathbf{b}\|_2^2 \|\mathbf{a}\|_2^2 \mathbf{I}_D - (\hat{\mathbf{a}}^* \otimes \mathbf{I}_D) \underline{\mathbf{A}}(\hat{\mathbf{a}} \otimes \mathbf{I}_D) - K^2 \|\mathbf{x}\|_2^2 \|\mathbf{b}\|_2^2 \|\mathbf{a}\|_2^2 \cos^2 \check{\theta} \mathbf{P}_{\mathbf{b}} \right\| \\ & \leq \left\| K^2 \|\mathbf{x}\|_2^2 \|\mathbf{b}\|_2^2 \|\mathbf{a}\| \odot \hat{\mathbf{a}} \| \hat{\mathbf{a}} \|_2^2 \mathbf{P}_{\mathbf{b}^\perp} \right\| + \|(\hat{\mathbf{a}}^* \otimes \mathbf{I}_D) \mathbf{E}(\hat{\mathbf{a}} \otimes \mathbf{I}_D)\| \\ & \leq K^2 \|\mathbf{x}\|_2^2 \|\mathbf{b}\|_2^2 \|\mathbf{a}\|_\infty^2 + \| \mathbf{E} \|_{S_1 \rightarrow S_\infty}. \end{aligned}$$

For sufficiently large  $C_1(\beta)$ , the conditions in (A.8), (A.9), (A.10), (A.11) imply

$$K^2 \|\mathbf{x}\|_2^2 \|\mathbf{b}\|_2^2 \|\mathbf{a}\|_2^2 \cos^2 \theta > 2(K^2 \|\mathbf{x}\|_2^2 \|\mathbf{b}\|_2^2 \|\mathbf{a}\|_\infty^2 \sin^2 \theta + \| \mathbf{E} \|_{S_1 \rightarrow S_\infty}).$$

Therefore,  $\hat{\mathbf{b}}$  is also a unique dominant eigenvector of  $K^2 \|\mathbf{x}\|_2^2 \|\mathbf{b}\|_2^2 \|\mathbf{a}\|_2^2 \mathbf{I}_D - (\hat{\mathbf{a}}^* \otimes \mathbf{I}_D) \mathbf{A}(\hat{\mathbf{a}} \otimes \mathbf{I}_D)$ .



Next we apply Lemma B.0.1 for

$$\begin{aligned}\underline{\mathbf{M}} &= K^2 \|\mathbf{x}\|_2^2 \|\mathbf{a}\|_2^2 \cos^2 \check{\theta} \mathbf{b} \mathbf{b}^*, \\ \mathbf{M} &= K^2 \|\mathbf{x}\|_2^2 \|\mathbf{b}\|_2^2 \|\mathbf{a}\|_2^2 \mathbf{I}_D - (\hat{\mathbf{a}}^* \otimes \mathbf{I}_D) \mathbf{A} (\hat{\mathbf{a}} \otimes \mathbf{I}_D), \\ \mathbf{q}_1 &= \frac{\mathbf{b}}{\|\mathbf{b}\|_2}, \quad \tilde{\mathbf{q}} = \hat{\mathbf{b}}.\end{aligned}$$

Then  $\lambda$  and  $\mathbf{D}$  in Lemma B.0.1 are given as  $\lambda = K^2 \|\mathbf{x}\|_2^2 \|\mathbf{b}\|_2^2 \|\mathbf{a}\|_2^2 \cos^2 \check{\theta}$  and  $\mathbf{D} = \mathbf{0}$ .

Similarly to the proof of Proposition A.1.2, we show

$$\frac{\|\mathbf{M} - \underline{\mathbf{M}}\|}{\lambda} \leq \frac{2\mu^2}{M} + \frac{2\|\mathbf{E}\|_{S_1 \rightarrow S_\infty}}{K^2 \|\mathbf{x}\|_2^2 \|\mathbf{b}\|_2^2 \|\mathbf{a}\|_2^2}$$

and

$$\frac{4\|(\mathbf{M} - \underline{\mathbf{M}})\mathbf{q}_1\|_2}{\lambda} \leq \frac{24\|\mathbf{E}\|_{S_1 \rightarrow S_\infty}}{K^2 \|\mathbf{x}\|_2^2 \|\mathbf{u}\|_2^2} \sin \theta + \frac{4\|\mathbf{Eu}\|_{S_\infty}}{K^2 \|\mathbf{x}\|_2^2 \|\mathbf{u}\|_2^3}.$$

Here we used the decomposition of  $\hat{\mathbf{a}}$  given by

$$\hat{\mathbf{a}} = \mathbf{P}_a \hat{\mathbf{a}} + \mathbf{P}_{a^\perp} \hat{\mathbf{a}}.$$

which satisfies  $\|\mathbf{P}_a \hat{\mathbf{a}}\|_2 = \cos \check{\theta}$  and  $\|\mathbf{P}_{a^\perp} \hat{\mathbf{a}}\|_2 = \sin \check{\theta}$ .

The remaining steps are identical to those in the proof of Proposition A.1.2 and we omit further details.

## C.2 Convergence of the Rank-1 Truncated Power Iteration Method

In this section, we prove Proposition A.1.4. First we present a theorem that shows local convergence of the rank-1 truncated power method for general matrix input  $\mathbf{B}$ . Then we will show the proof of Proposition A.1.4 as its corollary.

The separability structure in (1.5) corresponds to the rank-1 structure when the

eigenvector is rearranged as a matrix. We introduce a collection of structured subspaces, where their Minkowski sum is analogous to the support in the sparsity model. For  $(\mathbf{a}, \mathbf{b}) \in \mathbb{C}^M \times \mathbb{C}^D$ , we define

$$T(\mathbf{a}, \mathbf{b}) := \{\mathbf{a} \otimes \boldsymbol{\xi} + \mathbf{q} \otimes \mathbf{b} \mid \boldsymbol{\xi} \in \mathbb{C}^D, \mathbf{q} \in \mathbb{C}^M\}.$$

Then

$$\text{mat}(T(\mathbf{a}, \mathbf{b})) = \{\text{mat}(\mathbf{v}) \mid \mathbf{v} \in T(\mathbf{a}, \mathbf{b})\}$$

is equivalent to the tangent space of the rank-1 matrix  $\mathbf{U} = \mathbf{a}\mathbf{b}^\top$ .

Now we state a local convergence result for the rank-1 truncated power method in the following theorem, the proof of which is postponed to Section C.2.1.

**Theorem C.2.1.** *Let  $\mathbf{u} = \mathbf{a} \otimes \mathbf{b}$  be a unique dominant eigenvector of  $\underline{\mathbf{B}}$ . Define*

$$\tilde{\lambda}_2(\underline{\mathbf{B}}) := \sup_{\mathbf{v}, (\hat{\mathbf{a}}, \hat{\mathbf{b}}), (\tilde{\mathbf{a}}, \tilde{\mathbf{b}})} \left\{ \mathbf{v}^* \underline{\mathbf{B}} \mathbf{v} \mid \|\mathbf{v}\|_2 \leq 1, \mathbf{v} \in \mathbf{u}^\perp \cap [T(\mathbf{a}, \mathbf{b}) + T(\hat{\mathbf{a}}, \hat{\mathbf{b}}) + T(\tilde{\mathbf{a}}, \tilde{\mathbf{b}})] \right\}.$$

Suppose that

$$\frac{\sqrt{5}(\tilde{\lambda}_2(\underline{\mathbf{B}}) + 6\|\mathbf{B} - \underline{\mathbf{B}}\|_{S_1 \rightarrow S_\infty})}{\sqrt{1 - \tau^2} \lambda_1(\underline{\mathbf{B}}) - \tau \tilde{\lambda}_2(\underline{\mathbf{B}}) - 6(\sqrt{1 - \tau^2} + \tau)\|\mathbf{B} - \underline{\mathbf{B}}\|_{S_1 \rightarrow S_\infty}} < \mu, \quad (\text{C.17})$$

$$\frac{4\sqrt{6}\|\mathbf{B} - \underline{\mathbf{B}}\|_{S_1 \rightarrow S_\infty}}{\lambda_1(\underline{\mathbf{B}})} \leq \min \left[ \frac{1}{3\sqrt{2}}, \frac{(1 - \mu)\tau}{1 + \mu} \right], \quad (\text{C.18})$$

and

$$\tilde{\lambda}_2(\underline{\mathbf{B}}) + 6\|\mathbf{B} - \underline{\mathbf{B}}\|_{S_1 \rightarrow S_\infty} \leq \frac{\lambda_1(\underline{\mathbf{B}})}{5} \quad (\text{C.19})$$

hold for some  $0 < \mu < 1$  and  $0 < \tau < \frac{1}{3\sqrt{2}}$ . If  $\sin \angle(\mathbf{u}_0, \mathbf{u}) \leq \tau$ , then  $(\mathbf{u}_t)_{t \in \mathbb{N}}$  produced by Algorithm 2 satisfies

$$\sin \angle(\mathbf{u}_t, \mathbf{u}) \leq \mu \sin \angle(\mathbf{u}_{t-1}, \mathbf{u}) + \frac{(1 + \mu)4\sqrt{6}\|(\mathbf{B} - \underline{\mathbf{B}})\mathbf{u}\|_{S_\infty}}{\lambda_1(\underline{\mathbf{B}})}, \quad \forall t \in \mathbb{N}. \quad (\text{C.20})$$

Proposition A.1.4 is a direct consequence of Theorem C.2.1 for the case where the input matrix  $\mathbf{B}$  is given as  $\mathbf{B} = \|\mathbb{E}[\mathbf{A}]\| \mathbf{I}_{MD} - \mathbf{A}$ . We provide the proof below.

*Proof of Proposition A.1.4.* Given  $\mathbf{B} = \|\mathbb{E}[\mathbf{A}]\| \mathbf{I}_{MD} - \mathbf{A}$ , we apply Theorem C.2.1 for

$$\underline{\mathbf{B}} = K^2 \|\mathbf{x}\|_2^2 \mathbf{u} \mathbf{u}^*.$$

Then the difference between  $\mathbf{B}$  and  $\underline{\mathbf{B}}$  is given by

$$\mathbf{B} - \underline{\mathbf{B}} = (\|\mathbb{E}[\mathbf{A}]\| - K^2 \|\mathbf{x}\|_2^2 \|\mathbf{u}\|_2^2) \mathbf{I}_{MD} + K^2 \|\mathbf{x}\|_2^2 \mathbf{\Upsilon} - \mathbf{E}. \quad (\text{C.21})$$

In Section C.1.2, we have computed  $\underline{\mathbf{A}} = \mathbb{E}[\mathbf{A}]$  in (C.11), which is rewritten as

$$\underline{\mathbf{A}} = K^2 \|\mathbf{x}\|_2^2 (\|\mathbf{u}\|_2^2 \mathbf{P}_{\mathbf{u}^\perp} - \mathbf{\Upsilon}) \quad (\text{C.22})$$

with

$$\mathbf{\Upsilon} = \text{diag}(|\mathbf{a}|^2) \otimes \|\mathbf{b}\|_2^2 \mathbf{P}_{\mathbf{b}^\perp},$$

where  $\mathbf{u} = \mathbf{a} \otimes \mathbf{b}$ .

Therefore, it follows from (C.22) that

$$|\|\underline{\mathbf{A}}\| - K^2 \|\mathbf{x}\|_2^2 \|\mathbf{u}\|_2^2| \leq K^2 \|\mathbf{x}\|_2^2 \|\mathbf{\Upsilon}\| \leq K^2 \|\mathbf{x}\|_2^2 \|\mathbf{b}\|_2^2 \|\mathbf{a}\|_\infty^2. \quad (\text{C.23})$$

Then by plugging in (C.23) to (C.21), we obtain

$$|\|\mathbf{B} - \underline{\mathbf{B}}\||_{S_1 \rightarrow S_\infty} \leq 2K^2 \|\mathbf{x}\|_2^2 \|\mathbf{b}\|_2^2 \|\mathbf{a}\|_\infty^2 + |\|\mathbf{E}\||_{S_1 \rightarrow S_\infty}. \quad (\text{C.24})$$

On the other hand,  $\underline{\mathbf{B}}$  is a rank-1 matrix whose eigenvector is collinear with  $\mathbf{u}$

and the largest eigenvalue is given by

$$\lambda_1(\underline{\mathbf{B}}) = K^2 \|\mathbf{x}\|_2^2 \|\mathbf{b}\|_2^2 \|\mathbf{a}\|_2^2. \quad (\text{C.25})$$

Therefore,  $\underline{\mathbf{B}}$  also satisfies

$$\tilde{\lambda}_2(\underline{\mathbf{B}}) = 0.$$

Since  $\tilde{\lambda}_2(\underline{\mathbf{B}}) = 0$ , (C.17) and (C.18) are implied by

$$\frac{\|\|\mathbf{B} - \underline{\mathbf{B}}\|\|_{S_1 \rightarrow S_\infty}}{\lambda_1(\underline{\mathbf{B}})} \leq C_0 \min \left[ \mu \sqrt{1 - \tau^2}, \frac{(1 - \mu)\tau}{1 + \mu} \right], \quad (\text{C.26})$$

for a numerical constant  $C_0$ .

By applying (C.25) and the tail estimate of  $\|\|\mathbf{E}\|\|_{S_1 \rightarrow S_\infty}$  given in Lemma C.1.1 to (C.24), we verify that the sufficient condition in (C.26) is implied by (A.9), (A.10), and (A.11) for  $C_1 = c(\mu, \tau)C'_1$ ,  $C_2 = c(\mu, \tau)C'_2$  where  $C'_1$  and  $C'_2$  are constants that only depend on  $\beta$ .

Since the conditions in (C.17) and (C.18) are satisfied, Theorem C.2.1 provides the error bound in (A.15). This completes the proof.  $\square$

### C.2.1 Proof of Theorem C.2.1

In order to prove Theorem C.2.1, we first provide lemmas, which show upper bounds on the estimation error, given in terms of the principal angle, in the corresponding steps of Algorithm 2.

The first lemma provides upper bounds on norms of a matrix and a vector when they are restricted with a projection operator onto a subspace with the separability structure.

**Lemma C.2.2.** *Let*

$$\check{T} = \sum_{k=1}^r T(\mathbf{a}_k, \mathbf{b}_k)$$

for  $\{(\mathbf{a}_k, \mathbf{b}_k)\}_{k=1}^r \subset \mathbb{C}^M \times \mathbb{C}^D$ ,  $\mathbf{M} \in \mathbb{C}^{MD \times MD}$ , and  $\mathbf{u} \in \mathbb{C}^{MD}$ . Then

$$\|\mathbf{P}_{\check{T}} \mathbf{M} \mathbf{P}_{\check{T}}\| \leq 2r \|\mathbf{M}\|_{S_1 \rightarrow S_\infty}$$

and

$$\|\mathbf{P}_{\check{T}} \mathbf{M} \mathbf{u}\|_2 \leq \sqrt{2r} \|\mathbf{M} \mathbf{u}\|_{S_\infty}.$$

*Proof.* Let  $\mathbf{v} \in \check{T}$ . Then  $\text{rank}(\text{mat}(\mathbf{v})) \leq 2r$ . Let

$$\text{mat}(\mathbf{v}) = \sum_{l=1}^{2r} \sigma_l \mathbf{q}_l \boldsymbol{\xi}_l^\top$$

denotes the singular value decomposition of  $\text{mat}(\mathbf{v})$ , where  $\|\mathbf{q}_l\|_2 = \|\boldsymbol{\xi}_l\|_2 = 1$  and  $\sigma_l \geq 0$  for  $k = 1, \dots, 2r$ . Then

$$\mathbf{v} = \sum_{l=1}^{2r} \sigma_l \mathbf{q}_l \otimes \boldsymbol{\xi}_l.$$

Similarly, we can represent  $\mathbf{v}' \in \check{T}$  as

$$\mathbf{v}' = \sum_{j=1}^{2r} \sigma'_j \mathbf{q}'_j \otimes \boldsymbol{\xi}'_j.$$

Then

$$\begin{aligned} |\langle \mathbf{v}', \mathbf{M} \mathbf{v} \rangle| &\leq \sum_{j,l=1}^{2r} \sigma_l \sigma'_j |\langle (\mathbf{q}'_j \otimes \boldsymbol{\xi}'_j), \mathbf{M}(\mathbf{q}_l \otimes \boldsymbol{\xi}_l) \rangle| \\ &\leq \sum_{l=1}^{2r} \sigma_l \sum_{j=1}^{2r} \sigma'_j \|\mathbf{M}\|_{S_1 \rightarrow S_\infty} \\ &\leq 2r \|\mathbf{v}\|_2 \|\mathbf{v}'\|_2 \|\mathbf{M}\|_{S_1 \rightarrow S_\infty}. \end{aligned}$$

Therefore,

$$\|\mathbf{P}_{\check{T}}\mathbf{M}\mathbf{P}_{\check{T}}\| = \sup_{\mathbf{v}, \mathbf{v}' \in \check{T}} \{\langle \mathbf{v}', \mathbf{M}\mathbf{v} \rangle \mid \|\mathbf{v}\|_2 = \|\mathbf{v}'\|_2 = 1\} \leq 2r \|\mathbf{M}\|_{S_1 \rightarrow S_\infty}.$$

This proves the first assertion. The second assertion is obtained in a similar way by fixing  $\mathbf{v} = \mathbf{u}$ .  $\square$

The following lemma is a direct consequence of the Davis-Kahan Theorem together with Lemma C.2.2.

**Lemma C.2.3** (Perturbation). *Let  $\{(\mathbf{a}_k, \mathbf{b}_k)\}_{k=1}^r \subset \mathbb{C}^M \times \mathbb{C}^D$  satisfy*

$$T(\mathbf{a}, \mathbf{b}) \subset \sum_{k=1}^r T(\mathbf{a}_k, \mathbf{b}_k) =: \check{T}.$$

*Let  $\mathbf{v}$  (resp.  $\mathbf{u}$ ) be a unique most dominant eigenvector of  $\mathbf{P}_{\check{T}}\mathbf{M}_1\mathbf{P}_{\check{T}}$  (resp.  $\mathbf{P}_{\check{T}}\mathbf{M}_2\mathbf{P}_{\check{T}}$ ).*

*If*

$$\lambda_2(\mathbf{P}_{\check{T}}\mathbf{M}_2\mathbf{P}_{\check{T}}) + 2r \|\mathbf{M}_1 - \mathbf{M}_2\|_{S_1 \rightarrow S_\infty} \leq \frac{\lambda_1(\mathbf{P}_{\check{T}}\mathbf{M}_2\mathbf{P}_{\check{T}})}{5}, \quad (\text{C.27})$$

*then*

$$\sin \angle(\mathbf{v}, \mathbf{u}) \leq \frac{4\sqrt{2r} \|\mathbf{M}_1 - \mathbf{M}_2\mathbf{u}\|_{S_\infty}}{\lambda_1(\mathbf{P}_{\check{T}}\mathbf{M}_2\mathbf{P}_{\check{T}})}.$$

The following lemma shows how the conventional power method converges depending on the largest and second largest eigenvalues.

**Lemma C.2.4** (A Single Iteration of Power Method [97, Theorem 1.1]). *Let  $\mathbf{M}$  have a unique dominant eigenvector  $\mathbf{v}$ . Then*

$$\sin \angle(\mathbf{M}\hat{\mathbf{v}}, \mathbf{v}) \leq \frac{\lambda_2(\mathbf{M}) \sin \angle(\hat{\mathbf{v}}, \mathbf{v})}{\lambda_1(\mathbf{M}) \cos \angle(\hat{\mathbf{v}}, \mathbf{v}) - \lambda_2(\mathbf{M}) \sin \angle(\hat{\mathbf{v}}, \mathbf{v})}$$

*for any  $\hat{\mathbf{v}}$  such that  $\langle \hat{\mathbf{v}}, \mathbf{v} \rangle \neq 0$ .*

The following lemma is a modification of [84, Lemma 12] and shows that the

correlation is partially preserved after the rank-1 truncation. Unlike the canonical sparsity model, where the atoms are mutually orthogonal, in the low-rank atomic model, atoms in an atomic decomposition may have correlation. Our proof addresses this general case and the argument here also applies to an abstract atomic model.

**Lemma C.2.5** (Correlation after the Rank-1 Truncation). *Let  $\check{\mathbf{v}} \in \mathbb{C}^{MD}$  satisfy  $\|\check{\mathbf{v}}\|_2 = 1$  and  $\text{rank}(\text{mat}(\check{\mathbf{v}})) = 1$ . For  $\mathbf{v} \in \mathbb{C}^{MD}$  such that  $\|\mathbf{v}\|_2 = 1$ , let  $\hat{\mathbf{V}} \in \mathbb{C}^{M \times D}$  denote the best rank-1 approximation of  $\mathbf{V} = \text{mat}(\mathbf{v})$  and  $\hat{\mathbf{v}} = \text{vec}(\hat{\mathbf{V}})$ . Then*

$$|\langle \hat{\mathbf{v}}, \check{\mathbf{v}} \rangle| \geq |\langle \mathbf{v}, \check{\mathbf{v}} \rangle| - \min \left( \sqrt{1 - |\langle \mathbf{v}, \check{\mathbf{v}} \rangle|^2}, 2(1 - |\langle \mathbf{v}, \check{\mathbf{v}} \rangle|^2) \right). \quad (\text{C.28})$$

*Proof of Lemma C.2.5.* There exist  $\check{\mathbf{a}} \in \mathbb{C}^M$  and  $\check{\mathbf{b}} \in \mathbb{C}^D$  such that

$$\mathbf{U} = \text{mat}(\check{\mathbf{v}}) = \check{\mathbf{a}}\check{\mathbf{b}}^\top.$$

Let  $\hat{\mathbf{a}} \in \mathbb{C}^D$  and  $\hat{\mathbf{b}} \in \mathbb{C}^D$  respectively denote the left and right singular vectors of the rank-1 matrix  $\hat{\mathbf{V}}$ . Define  $T_1 = T(\{(\check{\mathbf{a}}, \check{\mathbf{b}})\})$ ,  $T_2 = T(\{(\hat{\mathbf{a}}, \hat{\mathbf{b}})\})$ , and  $T_3 = T_1 \cap T_2$ . Then  $T_1 + T_2$  is rewritten as

$$T_1 + T_2 = \mathbf{P}_{T_2^\perp} T_1 \oplus T_2 = \mathbf{P}_{T_2^\perp} T_1 \oplus T_3 \oplus \mathbf{P}_{T_3^\perp} T_2. \quad (\text{C.29})$$

Similarly, we also have

$$T_1 + T_2 = T_1 \oplus \mathbf{P}_{T_1^\perp} T_2 = \mathbf{P}_{T_3^\perp} T_1 \oplus T_3 \oplus \mathbf{P}_{T_1^\perp} T_2. \quad (\text{C.30})$$

By the definition of  $T_2$ , we have

$$\|\mathbf{P}_{T_2} \mathbf{v}\|_2 \geq \|\mathbf{P}_{T_1} \mathbf{v}\|_2.$$

Therefore,

$$\|\mathbf{P}_{\mathbf{P}_{T_3^\perp T_2}} \mathbf{v}\|_2 \geq \|\mathbf{P}_{\mathbf{P}_{T_3^\perp T_1}} \mathbf{v}\|_2.$$

Then by (C.29) and (C.30) it follows that

$$\|\mathbf{P}_{\mathbf{P}_{T_1^\perp T_2}} \mathbf{v}\|_2 \geq \|\mathbf{P}_{\mathbf{P}_{T_2^\perp T_1}} \mathbf{v}\|_2. \quad (\text{C.31})$$

By the Cauchy-Schwartz inequality and the Pythagorean identity, we have

$$|\langle \mathbf{v}, \check{\mathbf{v}} \rangle|^2 = |\langle \mathbf{P}_{T_1} \mathbf{v}, \check{\mathbf{v}} \rangle|^2 \leq \|\mathbf{P}_{T_1} \mathbf{v}\|_2^2 \leq 1 - \|\mathbf{P}_{T_1^\perp} \mathbf{v}\|_2^2 \leq 1 - \|\mathbf{P}_{\mathbf{P}_{T_1^\perp T_2}} \mathbf{v}\|_2^2 \leq 1 - \|\mathbf{P}_{\mathbf{P}_{T_2^\perp T_1}} \mathbf{v}\|_2^2,$$

where the last step follow from (C.31). The above inequality is rearranged as

$$\|\mathbf{P}_{\mathbf{P}_{T_2^\perp T_1}} \mathbf{v}\|_2 \leq \sqrt{1 - |\langle \mathbf{v}, \check{\mathbf{v}} \rangle|^2}. \quad (\text{C.32})$$

We may assume that  $|\langle \mathbf{v}, \check{\mathbf{v}} \rangle| > 2^{-1/2}$ . Otherwise, the right-hand side of (C.28) becomes negative and the inequality holds trivially. Then by (C.32) we have

$$\|\mathbf{P}_{\mathbf{P}_{T_2^\perp T_1}} \mathbf{v}\|_2 < |\langle \mathbf{v}, \check{\mathbf{v}} \rangle|,$$

which also implies

$$\|\mathbf{P}_{\mathbf{P}_{T_2^\perp T_1}} \mathbf{v}\|_2 \|\mathbf{P}_{\mathbf{P}_{T_2^\perp T_1}} \check{\mathbf{v}}\|_2 < |\langle \mathbf{v}, \check{\mathbf{v}} \rangle|. \quad (\text{C.33})$$



Since  $\mathbf{P}_{T_1+T_2}\check{\mathbf{v}} = \check{\mathbf{v}}$ , we have

$$\begin{aligned}
|\langle \mathbf{v}, \check{\mathbf{v}} \rangle| &= |\langle \mathbf{P}_{T_1+T_2} \mathbf{v}, \check{\mathbf{v}} \rangle| \\
&= |\langle (\mathbf{P}_{P_{T_2^\perp T_1}} + \mathbf{P}_{T_2}) \mathbf{v}, \check{\mathbf{v}} \rangle| \\
&= |\langle \mathbf{P}_{P_{T_2^\perp T_1}} \mathbf{v}, \check{\mathbf{v}} \rangle| + |\langle \mathbf{P}_{T_2} \mathbf{v}, \check{\mathbf{v}} \rangle| \\
&\leq \|\mathbf{P}_{P_{T_2^\perp T_1}} \mathbf{v}\|_2 \|\mathbf{P}_{P_{T_2^\perp T_1}} \check{\mathbf{v}}\|_2 + \|\mathbf{P}_{T_2} \mathbf{v}\|_2 \|\mathbf{P}_{T_2} \check{\mathbf{v}}\|_2 \\
&\leq \|\mathbf{P}_{P_{T_2^\perp T_1}} \mathbf{v}\|_2 \|\mathbf{P}_{P_{T_2^\perp T_1}} \check{\mathbf{v}}\|_2 + \sqrt{1 - \|\mathbf{P}_{P_{T_2^\perp T_1}} \mathbf{v}\|_2^2} \sqrt{1 - \|\mathbf{P}_{P_{T_2^\perp T_1}} \check{\mathbf{v}}\|_2^2}
\end{aligned}$$

By solving the above inequality for  $\|\mathbf{P}_{P_{T_2^\perp T_1}} \check{\mathbf{v}}\|_2$  under the condition in (C.33), we obtain

$$\begin{aligned}
\|\mathbf{P}_{P_{T_2^\perp T_1}} \check{\mathbf{v}}\|_2 &\leq \|\mathbf{P}_{P_{T_2^\perp T_1}} \mathbf{v}\|_2 |\langle \mathbf{v}, \check{\mathbf{v}} \rangle| + \sqrt{1 - \|\mathbf{P}_{P_{T_2^\perp T_1}} \mathbf{v}\|_2^2} \sqrt{1 - |\langle \mathbf{v}, \check{\mathbf{v}} \rangle|^2} \\
&\leq \min(1, 2\sqrt{1 - |\langle \mathbf{v}, \check{\mathbf{v}} \rangle|^2}).
\end{aligned} \tag{C.34}$$

Since  $\mathbf{P}_{T_2}(\mathbf{v} - \widehat{\mathbf{v}}) = \mathbf{0}$ , we have

$$\begin{aligned}
|\langle \mathbf{v}, \check{\mathbf{v}} \rangle| - |\langle \widehat{\mathbf{v}}, \check{\mathbf{v}} \rangle| &\leq |\langle \mathbf{v} - \widehat{\mathbf{v}}, \check{\mathbf{v}} \rangle| \\
&= |\langle \mathbf{P}_{P_{T_2^\perp T_1}}(\mathbf{v} - \widehat{\mathbf{v}}), \check{\mathbf{v}} \rangle| \\
&= |\langle \mathbf{P}_{P_{T_2^\perp T_1}} \mathbf{v}, \check{\mathbf{v}} \rangle| \\
&\leq \|\mathbf{P}_{P_{T_2^\perp T_1}} \mathbf{v}\|_2 \|\mathbf{P}_{P_{T_2^\perp T_1}} \check{\mathbf{v}}\|_2 \\
&\leq \min\left(\sqrt{1 - |\langle \mathbf{v}, \check{\mathbf{v}} \rangle|^2}, 2(1 - |\langle \mathbf{v}, \check{\mathbf{v}} \rangle|^2)\right),
\end{aligned}$$

where the last step follows from (C.32) and (C.34). The assertion is obtained by a rearrangement.  $\square$

*Proof of Theorem C.2.1.* We use the mathematical induction and it suffices to show  $\sin \angle(\mathbf{v}_t, \mathbf{u}) \leq \tau$  and (C.20) hold provided that  $\sin \angle(\mathbf{v}_{t-1}, \mathbf{u}) \leq \tau$  for fixed  $t$ .

Since  $\text{rank}(\text{mat}(\mathbf{v}_t)) = 1$ , there exist  $\mathbf{a}_t \in \mathbb{C}^M$  and  $\mathbf{b}_t \in \mathbb{C}^D$  such that  $\mathbf{v}_t = \mathbf{a}_t \otimes \mathbf{b}_t$ . Similarly, there exist  $\mathbf{a}_{t-1} \in \mathbb{C}^M$  and  $\mathbf{b}_{t-1} \in \mathbb{C}^D$  that satisfy  $\mathbf{v}_{t-1} = \mathbf{a}_{t-1} \otimes \mathbf{b}_{t-1}$ . Let

$$\check{T} = T(\mathbf{a}_{t-1}, \mathbf{b}_{t-1}) + T(\mathbf{a}_t, \mathbf{b}_t) + T(\mathbf{a}, \mathbf{b}).$$

Then define

$$\tilde{\mathbf{v}}'_t = \frac{\mathbf{P}_{\check{T}} \mathbf{B} \mathbf{P}_{\check{T}} \mathbf{v}_{t-1}}{\|\mathbf{P}_{\check{T}} \mathbf{B} \mathbf{P}_{\check{T}} \mathbf{v}_{t-1}\|_2}.$$

Note that Algorithm 2 produces the same result even when  $\tilde{\mathbf{v}}_t$  is replaced by  $\tilde{\mathbf{v}}'_t$ . Indeed, since  $\mathbf{P}_{\check{T}} \mathbf{v}_{t-1} = \mathbf{v}_{t-1}$ , it follows that  $\text{mat}(\mathbf{B} \mathbf{v}_{t-1})$  and  $\text{mat}(\mathbf{B} \mathbf{P}_{\check{T}} \mathbf{v}_{t-1})$  are collinear, so are their rank-1 approximations. Moreover, by  $\mathbf{v}_t$  is obtained normalizing as the normalized rearrangement of the rank-1 approximation of  $\text{mat}(\mathbf{B} \mathbf{v}_{t-1})$ , by the construction of  $\check{T}$ , it follows that  $\text{mat}(\mathbf{P}_{\check{T}} \mathbf{B} \mathbf{P}_{\check{T}} \mathbf{v}_{t-1})$  is also collinear with  $\text{mat}(\mathbf{B} \mathbf{v}_{t-1})$ .

Let  $\widehat{\mathbf{V}}'_t$  denote the rank-1 approximation of  $\text{mat}(\tilde{\mathbf{v}}'_t)$  and  $\widehat{\mathbf{u}}'_t = \text{vec}(\widehat{\mathbf{V}}'_t)$ . Then we have

$$\mathbf{v}_t = \widehat{\mathbf{u}}'_t / \|\widehat{\mathbf{u}}'_t\|_2.$$

Let  $\mathbf{v}(\check{T})$  denote a unique most dominant eigenvector of  $\mathbf{P}_{\check{T}} \mathbf{B} \mathbf{P}_{\check{T}}$ . Since  $\|\tilde{\mathbf{v}}'_t\|_2 = 1$ , we have  $\|\widehat{\mathbf{u}}'_t\|_2 \leq 1$ . Therefore,

$$\sin \angle(\mathbf{v}_t, \mathbf{v}(\check{T})) = \sqrt{1 - |\langle \mathbf{v}_t, \mathbf{v}(\check{T}) \rangle|^2} \leq \sqrt{1 - |\langle \widehat{\mathbf{u}}'_t, \mathbf{v}(\check{T}) \rangle|^2}.$$

We apply Lemma C.2.5 with  $\check{\mathbf{v}} = \mathbf{v}(\check{T})$  and  $\mathbf{v} = \tilde{\mathbf{v}}'_t$ . By Lemma C.2.5, we have

$$|\langle \widehat{\mathbf{u}}'_t, \mathbf{v}(\check{T}) \rangle| \geq |\langle \tilde{\mathbf{v}}'_t, \mathbf{v}(\check{T}) \rangle| - \min \left( \sqrt{1 - |\langle \tilde{\mathbf{v}}'_t, \mathbf{v}(\check{T}) \rangle|^2}, 2(1 - |\langle \tilde{\mathbf{v}}'_t, \mathbf{v}(\check{T}) \rangle|^2) \right),$$

which implies

$$\sqrt{1 - |\langle \widehat{\mathbf{u}}'_t, \mathbf{v}(\check{T}) \rangle|^2} \leq \sqrt{5} \sqrt{1 - |\langle \tilde{\mathbf{v}}'_t, \mathbf{u}(\check{T}) \rangle|^2} = \sqrt{5} \sin \angle(\tilde{\mathbf{v}}'_t, \mathbf{v}(\check{T})).$$

We apply Lemma C.2.4 with  $\mathbf{M} = \mathbf{P}_{\check{T}} \mathbf{B} \mathbf{P}_{\check{T}}$ ,  $\mathbf{v} = \mathbf{v}(\check{T})$ , and  $\hat{\mathbf{v}} = \mathbf{v}_{t-1}$ . Then

$$\begin{aligned} \sin \angle(\tilde{\mathbf{v}}'_t, \mathbf{v}(\check{T})) &\leq \frac{\lambda_2(\mathbf{M}) \sin \angle(\mathbf{v}_{t-1}, \mathbf{v}(\check{T}))}{\lambda_1(\mathbf{M}) \cos \angle(\mathbf{v}_{t-1}, \mathbf{v}(\check{T})) - \lambda_2(\mathbf{M}) \sin \angle(\mathbf{v}_{t-1}, \mathbf{v}(\check{T}))} \\ &\leq \frac{\lambda_2(\mathbf{M})}{\lambda_1(\mathbf{M}) \sqrt{1 - \tau^2} - \lambda_2(\mathbf{M}) \tau} \cdot \sin \angle(\mathbf{v}_{t-1}, \mathbf{v}(\check{T})), \end{aligned} \quad (\text{C.35})$$

where the last step follows from  $\sin \angle(\mathbf{v}_{t-1}, \mathbf{v}(\check{T})) \leq \tau'$ .

Next we compute the two largest eigenvalues of  $\mathbf{P}_{\check{T}} \mathbf{B} \mathbf{P}_{\check{T}}$ . Since  $\mathbf{u}$  is a unique dominant eigenvector of  $\underline{\mathbf{B}}$  and  $\mathbf{P}_{\check{T}} \mathbf{u} = \mathbf{u}$ , we have  $\lambda_1(\mathbf{P}_{\check{T}} \underline{\mathbf{B}} \mathbf{P}_{\check{T}}) = \lambda_1(\underline{\mathbf{B}})$ . Therefore, by the triangle inequality,

$$\begin{aligned} \lambda_1(\mathbf{P}_{\check{T}} \mathbf{B} \mathbf{P}_{\check{T}}) &\geq \lambda_1(\mathbf{P}_{\check{T}} \underline{\mathbf{B}} \mathbf{P}_{\check{T}}) - \|\mathbf{P}_{\check{T}}(\mathbf{B} - \underline{\mathbf{B}}) \mathbf{P}_{\check{T}}\| \\ &\geq \lambda_1(\underline{\mathbf{B}}) - 6 \|\mathbf{B} - \underline{\mathbf{B}}\|_{S_1 \rightarrow S_\infty}. \end{aligned} \quad (\text{C.36})$$

By the variational characterization of eigenvalues, we have

$$\lambda_2(\mathbf{P}_{\check{T}} \mathbf{B} \mathbf{P}_{\check{T}}) = \sup_{\mathbf{v}} \{ \mathbf{v}^* \mathbf{B} \mathbf{v} \mid \|\mathbf{v}\|_2 \leq 1, \mathbf{v} \in \mathbf{u}^\perp \cap \check{T} \} \leq \tilde{\lambda}_2(\underline{\mathbf{B}}).$$

Therefore,

$$\begin{aligned} \lambda_2(\mathbf{P}_{\check{T}} \mathbf{B} \mathbf{P}_{\check{T}}) &\leq \lambda_2(\mathbf{P}_{\check{T}} \underline{\mathbf{B}} \mathbf{P}_{\check{T}}) + \|\mathbf{P}_{\check{T}}(\mathbf{B} - \underline{\mathbf{B}}) \mathbf{P}_{\check{T}}\| \\ &\leq \tilde{\lambda}_2(\underline{\mathbf{B}}) + 6 \|\mathbf{B} - \underline{\mathbf{B}}\|_{S_1 \rightarrow S_\infty}. \end{aligned} \quad (\text{C.37})$$

By plugging in (C.36) and (C.37) into (C.35), we obtain that (C.17) implies

$$\sin \angle(\mathbf{v}_t, \mathbf{v}(\check{T})) \leq \mu \sin \angle(\mathbf{v}_{t-1}, \mathbf{v}(\check{T})). \quad (\text{C.38})$$

Moreover, by the transitivity of the angle function [98], we also have

$$\angle(\mathbf{v}_{t-1}, \mathbf{v}(\check{T})) \leq \angle(\mathbf{v}_{t-1}, \mathbf{u}) + \angle(\mathbf{u}, \mathbf{v}(\check{T})). \quad (\text{C.39})$$

Next we apply Lemma C.2.3 for  $\mathbf{M}_1 = \mathbf{B}$ ,  $\mathbf{M}_2 = \underline{\mathbf{B}}$ , and  $\mathbf{v} = \mathbf{v}(\check{T})$ . Since (C.19) implies (C.27), it follows from Lemma C.2.3 that

$$\sin \angle(\mathbf{u}, \mathbf{v}(\check{T})) \leq \frac{4\sqrt{6} \|(\mathbf{B} - \underline{\mathbf{B}})\mathbf{u}\|_{S_\infty}}{\lambda_1(\underline{\mathbf{B}})}.$$

Then (C.18) implies

$$\sin \angle(\mathbf{v}_t, \mathbf{v}(\check{T})) < \frac{1}{3\sqrt{2}}.$$

Since  $\sin \angle(\mathbf{v}_{t-1}, \mathbf{u}) \leq \tau < \frac{1}{3\sqrt{2}}$ , it follows that (C.39) implies

$$\sin \angle(\mathbf{v}_{t-1}, \mathbf{v}(\check{T})) \leq \sin \angle(\mathbf{v}_{t-1}, \mathbf{u}) + \sin \angle(\mathbf{u}, \mathbf{v}(\check{T})). \quad (\text{C.40})$$

By (C.18), (C.38), and (C.40),

$$\sin \angle(\mathbf{v}_t, \mathbf{v}(\check{T})) < \frac{1}{3\sqrt{2}}.$$

Similarly to the previous case, the transitivity of the angle function implies

$$\angle(\mathbf{v}_t, \mathbf{u}) \leq \angle(\mathbf{v}_t, \mathbf{v}(\check{T})) + \angle(\mathbf{v}(\check{T}), \mathbf{u}).$$

Then it follows that

$$\sin \angle(\mathbf{v}_t, \mathbf{u}) \leq \sin \angle(\mathbf{v}_t, \mathbf{v}(\check{T})) + \sin \angle(\mathbf{v}(\check{T}), \mathbf{u}).$$

By collecting the above inequalities, we obtain

$$\sin \angle(\mathbf{v}_t, \mathbf{u}) \leq \mu \sin \angle(\mathbf{v}_t, \mathbf{v}(\check{T})) + (1 + \mu) \sin \angle(\mathbf{v}(\check{T}), \mathbf{u}). \quad (\text{C.41})$$

Finally, we verify that (C.41) and (C.18) imply  $\sin \angle(\mathbf{v}_t, \mathbf{u}) \leq \tau$ .

This completes the proof. □

### C.3 Proof of Lemma 3.4.1

Let  $\mathbf{x}' \in \mathbb{C}^L$  and  $\mathbf{b}' \in \mathbb{C}^D$ . By the definition of an adjoint operator, we have

$$\langle \mathbf{x}' \otimes \mathbf{b}' \otimes \mathbf{1}_{M,1}, \mathcal{A}^*(\underline{\mathbf{y}}) \rangle = \langle \mathcal{A}(\mathbf{x}' \otimes \mathbf{b}' \otimes \mathbf{1}_{M,1}), \underline{\mathbf{y}} \rangle.$$

Then by the definition of  $\mathcal{A}$ , we continue as

$$\begin{aligned} \langle \mathcal{A}(\mathbf{x}' \otimes \mathbf{b}' \otimes \mathbf{1}_{M,1}), \underline{\mathbf{y}} \rangle &= \sum_{m=1}^M \langle \mathbf{C}_{S^* \Phi_m \mathbf{b}'} \mathbf{x}', \mathbf{y}_m \rangle = \sum_{m=1}^M \mathbf{x}'^* \mathbf{C}_{S^* \Phi_m \mathbf{b}'}^* \mathbf{y}_m \\ &= \sum_{m=1}^M \mathbf{x}'^* (\mathfrak{I} S^* \overline{\Phi_m \mathbf{b}'} \circledast \mathbf{y}_m) = \sum_{m=1}^M \mathbf{x}'^* \mathfrak{I} (S^* \overline{\Phi_m \mathbf{b}'} \circledast \mathfrak{I} \mathbf{y}_m) \\ &= \sum_{m=1}^M \mathbf{x}'^* \mathfrak{I} \mathbf{C}_{\mathbf{y}_m}^\top S^* \overline{\Phi_m \mathbf{b}'} \end{aligned}$$

Here we used the fact that the transpose of  $\mathbf{C}_h$  satisfies  $\mathbf{C}_h^\top = \mathbf{C}_{\mathfrak{I}h}$ .

Finally, by tensorizing the last term, we obtain

$$\begin{aligned} \sum_{m=1}^M \mathbf{x}'^* \mathfrak{I} \mathbf{C}_{\mathbf{y}_m}^\top S^* \overline{\Phi_m \mathbf{b}'} &= \sum_{m=1}^M \mathbf{x}'^* ((\mathbf{b}')^* \otimes \mathbf{I}_L) \text{vec}(\mathfrak{I} \mathbf{C}_{\mathbf{y}_m}^\top S^* \overline{\Phi_m}) \\ &= \sum_{m=1}^M (\mathbf{b}' \otimes \mathbf{x}')^* \text{vec}(\mathfrak{I} \mathbf{C}_{\mathbf{y}_m}^\top S^* \overline{\Phi_m}) = \sum_{m=1}^M (\mathbf{x}' \otimes \mathbf{b}')^* \text{vec}(\Phi_m^* \mathbf{S} \mathbf{C}_{\mathbf{y}_m} \mathfrak{I}). \end{aligned}$$

The assertion follows since  $\mathbf{x}'$  and  $\mathbf{b}'$  were arbitrary.

## REFERENCES

- [1] G. Xu, H. Liu, L. Tong, and T. Kailath, “A least-squares approach to blind channel identification,” *Signal Processing, IEEE Transactions on*, vol. 43, no. 12, pp. 2982–2993, 1995.
- [2] G. B. Giannakis and E. Serpedin, “Linear multichannel blind equalizers of non-linear fir volterra channels,” *Signal Processing, IEEE Transactions on*, vol. 45, no. 1, pp. 67–81, 1997.
- [3] E. Moulines, P. Duhamel, J.-F. Cardoso, and S. Mayrargue, “Subspace methods for the blind identification of multichannel fir filters,” *Signal Processing, IEEE Transactions on*, vol. 43, no. 2, pp. 516–525, 1995.
- [4] P. Campisi and K. Egiazarian, *Blind image deconvolution: theory and applications*. CRC press, 2016.
- [5] O. V. Michailovich and D. Adam, “A novel approach to the 2-d blind deconvolution problem in medical ultrasound,” *IEEE transactions on medical imaging*, vol. 24, no. 1, pp. 86–104, 2005.
- [6] A. K. Katsaggelos, *Digital image restoration*. Springer-Verlag Berlin Heidelberg, 1991.
- [7] W. Soudene, K. Abed-Meraim, and A. Beghdadi, “A new look to multichannel blind image deconvolution,” *Image Processing, IEEE Transactions on*, vol. 18, no. 7, pp. 1487–1500, 2009.
- [8] J. M. Mendel, *Optimal seismic deconvolution: an estimation-based approach*. Elsevier, 2013.
- [9] K. G. Sabra, P. Gerstoft, P. Roux, W. Kuperman, and M. C. Fehler, “Surface wave tomography from microseisms in southern california,” *Geophysical Research Letters*, vol. 32, no. 14, 2005.
- [10] K. Sabra and D. Dowling, “Blind deconvolution in oceanic waveguides using artificial time reversal,” *J. Acoust. Soc. Am.*, vol. 116, pp. 262–271, 2004.
- [11] K. G. Sabra, H.-C. Song, and D. R. Dowling, “Ray-based blind deconvolution in ocean sound channels,” *The Journal of the Acoustical Society of America*, vol. 127, no. 2, EL42–EL47, 2010.

- [12] S. H. Abadi, D. Rouseff, and D. R. Dowling, “Blind deconvolution for robust signal estimation and approximate source localization,” *The Journal of the Acoustical Society of America*, vol. 131, no. 4, pp. 2599–2610, 2012.
- [13] S. H. Abadi, H. C. Song, and D. R. Dowling, “Broadband sparse-array blind deconvolution using frequency-difference beamforming,” *The Journal of the Acoustical Society of America*, vol. 132, no. 5, pp. 3018–3029, 2012.
- [14] W. Munk, P. Worcester, and C. Wunsch, *Ocean acoustic tomography*. Cambridge University Press, 2009.
- [15] D. R. Dowling and K. G. Sabra, “Acoustic remote sensing,” *Annual Review of Fluid Mechanics*, vol. 47, pp. 221–243, 2015.
- [16] S. W. Lani, K. G. Sabra, W. S. Hodgkiss, W. Kuperman, and P. Roux, “Coherent processing of shipping noise for ocean monitoring,” *The Journal of the Acoustical Society of America*, vol. 133, no. 2, EL108–EL113, 2013.
- [17] E. Larose, A. Derode, M. Campillo, and M. Fink, “Imaging from one-bit correlations of wideband diffuse wave fields,” *Journal of Applied Physics*, vol. 95, no. 12, pp. 8393–8399, 2004.
- [18] P. Roux, W. Kuperman, N. Group, *et al.*, “Extracting coherent wave fronts from acoustic ambient noise in the ocean,” *The Journal of the Acoustical Society of America*, vol. 116, no. 4, pp. 1995–2003, 2004.
- [19] L. Tong and S. Perreau, “Multichannel blind identification: From subspace to maximum likelihood methods,” *PROCEEDINGS-IEEE*, vol. 86, pp. 1951–1968, 1998.
- [20] G. Harikumar and Y. Bresler, “Analysis and comparative evaluation of techniques for multichannel blind deconvolution,” in *Statistical Signal and Array Processing, 1996. Proceedings., 8th IEEE Signal Processing Workshop on (Cat. No. 96TB10004)*, IEEE, 1996, pp. 332–335.
- [21] L. Tong, G. Xu, and T. Kailath, “Blind identification and equalization based on second-order statistics: A time domain approach,” *Information Theory, IEEE Transactions on*, vol. 40, no. 2, pp. 340–349, 1994.
- [22] L. Tong, G. Xu, B. Hassibi, and T. Kailath, “Blind channel identification based on second-order statistics: A frequency-domain approach,” *Information Theory, IEEE Transactions on*, vol. 41, no. 1, pp. 329–334, 1995.

- [23] G. B. Giannakis and J. M. Mendel, “Identification of nonminimum phase systems using higher order statistics,” *Acoustics, Speech and Signal Processing, IEEE Transactions on*, vol. 37, no. 3, pp. 360–377, 1989.
- [24] M. J. Buckingham, B. V. Berkout, and S. A. Glegg, “Imaging the ocean with ambient noise,” *Nature*, vol. 356, pp. 327–329, 1992.
- [25] R. Snieder and K. Wapenaar, “Imaging with ambient noise,” *Physics Today*, pp. 44–49, 2010.
- [26] A. Ahmed, B. Recht, and J. Romberg, “Blind deconvolution using convex programming,” *Information Theory, IEEE Transactions on*, vol. 60, no. 3, pp. 1711–1732, 2014.
- [27] K. Lee and M. Junge, “Rip-like properties in subsampled blind deconvolution,” *arXiv preprint arXiv:1511.06146*, 2015.
- [28] M. A. Davenport and J. Romberg, “An overview of low-rank matrix recovery from incomplete observations,” *IEEE Journal of Selected Topics in Signal Processing*, vol. 10, no. 4, pp. 608–622, 2016.
- [29] E. J. Candès and B. Recht, “Exact matrix completion via convex optimization,” *Foundations of Computational mathematics*, vol. 9, no. 6, pp. 717–772, 2009.
- [30] E. J. Candès and T. Tao, “The power of convex relaxation: Near-optimal matrix completion,” *IEEE Transactions on Information Theory*, vol. 56, no. 5, pp. 2053–2080, 2010.
- [31] B. Recht, M. Fazel, and P. A. Parrilo, “Guaranteed minimum-rank solutions of linear matrix equations via nuclear norm minimization,” *SIAM Review*, vol. 52, no. 3, pp. 471–501, 2010.
- [32] S. Burer and R. Monteiro, “A nonlinear programming algorithm for solving semidefinite programs via low-rank factorization,” *Math. Program., Ser. B*, vol. 95, pp. 329–357, 2003.
- [33] S. Burer and R. D. Monteiro, “Local minima and convergence in low-rank semidefinite programming,” *Mathematical Programming*, vol. 103, no. 3, pp. 427–444, 2005.
- [34] F. B. Jensen, W. A. Kuperman, M. B. Porter, and H. Schmidt, *Computational ocean acoustics*. Springer Science & Business Media, 2011.



- [35] M. I. Gurelli and C. L. Nikias, "EVAM: An eigenvector-based algorithm for multichannel blind deconvolution of input colored signals," vol. 43, no. 1, pp. 134–149, 1995.
- [36] S. R. Chapin, G. E. Ioup, J. W. Ioup, and G. B. Smith, "Statistical analysis of acoustic greens functions in a shallow ocean environment," *The Journal of the Acoustical Society of America*, vol. 109, no. 5, pp. 2295–2295, 2001.
- [37] G. B. Smith, "Blind deconvolution for multipath mitigation in shallow water acoustics," *The Journal of the Acoustical Society of America*, vol. 107, no. 5, pp. 2868–2868, 2000.
- [38] M. K. Broadhead and L. A. Pflug, "Performance of some sparseness criterion blind deconvolution methods in the presence of noise," *The Journal of the Acoustical Society of America*, vol. 107, no. 2, pp. 885–893, 2000.
- [39] M. J. Roan, M. R. Gramann, J. G. Erling, and L. H. Sibul, "Blind deconvolution applied to acoustical systems identification with supporting experimental results," *The Journal of the Acoustical Society of America*, vol. 114, no. 4, pp. 1988–1996, 2003.
- [40] B. S. Cazzolato, P. Nelson, P. Joseph, and R. J. Brind, "Numerical simulation of optimal deconvolution in a shallow-water environment," *The Journal of the Acoustical Society of America*, vol. 110, no. 1, pp. 170–185, 2001.
- [41] M. K. Broadhead, L. A. Pflug, and R. L. Field, "Use of higher order statistics in source signature estimation," *The Journal of the Acoustical Society of America*, vol. 107, no. 5, pp. 2576–2585, 2000.
- [42] M. A. Davenport and M. B. Wakin, "Compressive sensing of analog signals using discrete prolate spheroidal sequences," *Applied and Computational Harmonic Analysis*, vol. 33, no. 3, pp. 438–472, 2012.
- [43] J. Romberg, N. Tian, and K. Sabra, "Multichannel blind deconvolution using low rank recovery," in *SPIE Defense, Security, and Sensing*, International Society for Optics and Photonics, 2013, 87500E–87500E.
- [44] G. M. Wenz, "Acoustic ambient noise in the ocean: Spectra and sources," *The Journal of the Acoustical Society of America*, vol. 34, no. 12, pp. 1936–1956, 1962.
- [45] M. B. Porter, *The kraken normal mode program*, 2001.
- [46] J. Skinner and W. Hodgkiss, "A networked/autonomous receiving array system," in *OCEANS 2008*, IEEE, 2008, pp. 1–6.

- [47] C. Leroy, S. Lani, K. G. Sabra, W. S. Hodgkiss, W. Kuperman, and P. Roux, “Enhancing the emergence rate of coherent wavefronts from ocean ambient noise correlations using spatio-temporal filters,” *The Journal of the Acoustical Society of America*, vol. 132, no. 2, pp. 883–893, 2012.
- [48] E. Vincent, R. Gribonval, and C. Févotte, “Performance measurement in blind audio source separation,” *IEEE transactions on audio, speech, and language processing*, vol. 14, no. 4, pp. 1462–1469, 2006.
- [49] A. D. Back and A. S. Weigend, “Discovering structure in finance using independent component analysis,” in *Decision Technologies for Computational Finance*, Springer, 1998, pp. 309–322.
- [50] L. C. Parra and C. V. Alvino, “Geometric source separation: Merging convolutive source separation with geometric beamforming,” *IEEE Transactions on Speech and Audio Processing*, vol. 10, no. 6, pp. 352–362, 2002.
- [51] A. J. Bell and T. J. Sejnowski, “An information-maximization approach to blind separation and blind deconvolution,” *Neural computation*, vol. 7, no. 6, pp. 1129–1159, 1995.
- [52] A. Hyvärinen and E. Oja, “Independent component analysis: Algorithms and applications,” *Neural networks*, vol. 13, no. 4, pp. 411–430, 2000.
- [53] M. B. McCoy, V. Cevher, Q. T. Dinh, A. Asaei, and L. Baldassarre, “Convexity in source separation: Models, geometry, and algorithms,” *IEEE Signal Processing Magazine*, vol. 31, no. 3, pp. 87–95, 2014.
- [54] M. S. Pedersen, J. Larsen, U. Kjems, and L. C. Parra, “A survey of convolutive blind source separation methods,” *Multichannel Speech Processing Handbook*, pp. 1065–1084, 2007.
- [55] S. Makino, H. Sawada, R. Mukai, and S. Araki, “Blind source separation of convolutive mixtures of speech in frequency domain,” *IEICE transactions on fundamentals of electronics, communications and computer sciences*, vol. 88, no. 7, pp. 1640–1655, 2005.
- [56] S. Araki, R. Mukai, S. Makino, T. Nishikawa, and H. Saruwatari, “The fundamental limitation of frequency domain blind source separation for convolutive mixtures of speech,” *IEEE Transactions on Speech and Audio Processing*, vol. 11, no. 2, pp. 109–116, 2003.
- [57] O. Yilmaz and S. Rickard, “Blind separation of speech mixtures via time-frequency masking,” *IEEE Transactions on signal processing*, vol. 52, no. 7, pp. 1830–1847, 2004.

- [58] K. Kokkinakis and A. K. Nandi, “Multichannel blind deconvolution for source separation in convolutive mixtures of speech,” *IEEE Transactions on Audio, Speech, and Language Processing*, vol. 14, no. 1, pp. 200–212, 2006.
- [59] H.-M. Park, C. S. Dhir, S.-H. Oh, and S.-Y. Lee, “A filter bank approach to independent component analysis for convolved mixtures,” *Neurocomputing*, vol. 69, no. 16, pp. 2065–2077, 2006.
- [60] N. Tian, S.-H. Byun, K. Sabra, and J. Romberg, “Multichannel myopic deconvolution in underwater acoustic channels via low-rank recovery,” *J. Acoust. Soc. Am.*, vol. 141, no. 5, pp. 3337–3348, 2017.
- [61] R. H. Keshavan, A. Montanari, and S. Oh, “Matrix completion from a few entries,” vol. 56, no. 6, pp. 2980–2998, 2010.
- [62] R. H. Keshavan, “Efficient algorithms for collaborative filtering,” PhD thesis, Stanford University, 2012.
- [63] P. Jain, P. Netrapalli, and S. Sanghavi, “Low-rank matrix completion using alternating minimization,” in *Proceedings of the forty-fifth annual ACM symposium on Theory of computing*, ACM, 2013, pp. 665–674.
- [64] M. Hardt, “Understanding alternating minimization for matrix completion,” in *Foundations of Computer Science (FOCS), 2014 IEEE 55th Annual Symposium on*, IEEE, 2014, pp. 651–660.
- [65] E. J. Candes, X. Li, and M. Soltanolkotabi, “Phase retrieval via Wirtinger flow: Theory and algorithms,” vol. 61, no. 4, pp. 1985–2007, 2015.
- [66] Y. Chen and E. Candes, “Solving random quadratic systems of equations is nearly as easy as solving linear systems,” in *Advances in Neural Information Processing Systems*, 2015, pp. 739–747.
- [67] G. Wang, G. B. Giannakis, and Y. C. Eldar, “Solving systems of random quadratic equations via truncated amplitude flow,” *arXiv preprint arXiv:1605.08285*, 2016.
- [68] T. T. Cai, X. Li, and Z. Ma, “Optimal rates of convergence for noisy sparse phase retrieval via thresholded Wirtinger flow,” *The Annals of Statistics*, vol. 44, no. 5, pp. 2221–2251, 2016.
- [69] P. Netrapalli, P. Jain, and S. Sanghavi, “Phase retrieval using alternating minimization,” in *Advances in Neural Information Processing Systems*, 2013, pp. 2796–2804.

- [70] I. Waldspurger, “Phase retrieval with random Gaussian sensing vectors by alternating projections,” *arXiv preprint arXiv:1609.03088*, 2016.
- [71] S. Choudhary and U. Mitra, “Sparse blind deconvolution: What cannot be done,” in *International Symposium on Information Theory*, IEEE, 2014, pp. 3002–3006.
- [72] Y. Li, K. Lee, and Y. Bresler, “Identifiability in blind deconvolution with subspace or sparsity constraints,” vol. 62, no. 7, pp. 4266–4275, 2016.
- [73] E. Riegler, D. Stotz, and H. Bölcskei, “Information-theoretic limits of matrix completion,” in *International Symposium on Information Theory*, IEEE, 2015, pp. 1836–1840.
- [74] Y. Li, K. Lee, and Y. Bresler, “Optimal sample complexity for blind gain and phase calibration,” vol. 64, no. 21, pp. 5549–5556, 2016.
- [75] M. Kech and F. Krahmer, “Optimal injectivity conditions for bilinear inverse problems with applications to identifiability of deconvolution problems,” *SIAM Journal on Applied Algebra and Geometry*, vol. 1, no. 1, pp. 20–37, 2017.
- [76] Y. Li, K. Lee, and Y. Bresler, “Identifiability in bilinear inverse problems with applications to subspace or sparsity-constrained blind gain and phase calibration,” vol. 63, no. 2, pp. 822–842, 2017.
- [77] —, “Identifiability and stability in blind deconvolution under minimal assumptions,” vol. 63, no. 7, pp. 4619–4633, 2017.
- [78] G. Tang and B. Recht, “Convex blind deconvolution with random masks,” in *Computational Optical Sensing and Imaging*, Optical Society of America, 2014, CW4C–1.
- [79] S. Bahmani and J. Romberg, “Lifting for blind deconvolution in random mask imaging: Identifiability and convex relaxation,” *SIAM Journal on Imaging Sciences*, vol. 8, no. 4, pp. 2203–2238, 2015.
- [80] K. Lee, Y. Li, M. Junge, and Y. Bresler, “Blind recovery of sparse signals from subsampled convolution,” vol. 63, no. 2, pp. 802–821, 2017.
- [81] X. Li, S. Ling, T. Strohmer, and K. Wei, “Rapid, robust, and reliable blind deconvolution via nonconvex optimization,” *arXiv preprint arXiv:1606.04933*, 2016.
- [82] W. Mantzel and J. Romberg, “Compressed subspace matching on the continuum,” *Information and Inference*, iav008, 2015.

- [83] K. Lee, F. Krahmer, and J. Romberg, “Spectral methods for passive imaging: Non-asymptotic performance and robustness,” *arXiv preprint arXiv:1708.04343*, 2017.
- [84] X.-T. Yuan and T. Zhang, “Truncated power method for sparse eigenvalue problems,” *Journal of Machine Learning Research*, vol. 14, no. Apr, pp. 899–925, 2013.
- [85] K. Lee and Y. Bresler, “ADMiRA: Atomic decomposition for minimum rank approximation,” vol. 56, no. 9, pp. 4402–4416, 2010.
- [86] P. Jain, R. Meka, and I. S. Dhillon, “Guaranteed rank minimization via singular value projection,” in *Advances in Neural Information Processing Systems*, 2010, pp. 937–945.
- [87] K. Lee, N. Tian, and J. Romberg, “Fast and guaranteed blind multichannel deconvolution under a bilinear system model,” *arXiv preprint arXiv:1610.06469v1*, 2016.
- [88] R. Adamczak and P. Wolff, “Concentration inequalities for non-Lipschitz functions with bounded derivatives of higher order,” *Probability Theory and Related Fields*, vol. 162, no. 3-4, pp. 531–586, 2015.
- [89] J. Ye, R. Janardan, and Q. Li, “Gpca: An efficient dimension reduction scheme for image compression and retrieval,” in *Proceedings of the tenth ACM SIGKDD international conference on Knowledge discovery and data mining*, ACM, 2004, pp. 354–363.
- [90] A. K. Jain and S. Z. Li, *Handbook of face recognition*. Springer, 2011.
- [91] J. Wright, Y. Ma, J. Mairal, G. Sapiro, T. S. Huang, and S. Yan, “Sparse representation for computer vision and pattern recognition,” *Proceedings of the IEEE*, vol. 98, no. 6, pp. 1031–1044, 2010.
- [92] P.-A. Absil, R. Mahony, and R. Sepulchre, *Optimization algorithms on matrix manifolds*. Princeton University Press, 2009.
- [93] M. L. Overton and R. S. Womersley, “Second derivatives for optimizing eigenvalues of symmetric matrices,” *SIAM Journal on Matrix Analysis and Applications*, vol. 16, no. 3, pp. 697–718, 1995.
- [94] N. Boumal, B. Mishra, P.-A. Absil, and R. Sepulchre, “Manopt, a Matlab toolbox for optimization on manifolds,” *Journal of Machine Learning Research*, vol. 15, pp. 1455–1459, 2014.

- [95] C. Davis and W. M. Kahan, “The rotation of eigenvectors by a perturbation. III,” *SIAM Journal on Numerical Analysis*, vol. 7, no. 1, pp. 1–46, 1970.
- [96] G. H. Golub and C. F. Van Loan, *Matrix computations*. JHU Press, 2012.
- [97] G. W. Stewart, *Matrix Algorithms: Volume II: Eigensystems*. Society for Industrial and Applied Mathematics, 2001.
- [98] P. Å. Wedin, “On angles between subspaces of a finite dimensional inner product space,” in *Matrix Pencils*, Springer, 1983, pp. 263–285.